THÈSE

En vue de l'obtention du

DOCTORAT DE L'UNIVERSITÉ DE TOULOUSE

Délivré par :

Institut National Polytechnique de Toulouse (INP Toulouse)

Discipline ou spécialité :

Energétique et Transferts

Présentée et soutenue par :

M. LUCAS ESCLAPEZ

le vendredi 22 mai 2015

Titre :

NUMERICAL STUDY OF IGNITION AND INTER-SECTOR FLAME PROPAGATION IN GAS TURBINE

Ecole doctorale :

Mécanique, Energétique, Génie civil, Procédés (MEGeP)

Unité de recherche :

CERFACS (CERFACS)

Directeur(s) de Thèse :

MME BENEDICTE CUENOT

MME ELEONORE RIBER

Rapporteurs :

M. BENOIT FIORINA, ECOLE CENTRALE DE PARIS

M. FABIEN HALTER, UNIVERSITE D'ORLEANS

Membre(s) du jury :

M. MARC BELLENOUE, UNIVERSITE D'ORLEANS, Président

M. BRUNO RENOU, INSA ROUEN, Membre

Mme BENEDICTE CUENOT, CERFACS, Membre

Mme ELEONORE RIBER, CERFACS, Membre

Contents

Acknowledgements

Je voudrais tout d'abord remercier les membres du Jury: B. Fiorina et F. Halter d'avoir relu et évalué le contenu de ce manuscrit, B. Renou, M. Bellenoue et S. Richard de les avoir rejoints au CERFACS pour assister à la soutenance et animer une séance de discussion intéressante et pleine de perspectives.

Je remercie ensuite mes encadrantes, Bénédicte Cuenot et Eleonore Riber, qui m'ont permis de mener à bien ces travaux dans un cadre de travail idéal, en y apportant leur expérience, leur enthousiasme et leur passion pour la recherche et la combustion. Je remercie aussi Thierry Poinsot de m'avoir en quelque sorte attiré au CERFACS à l'issue de mon cursus ingénieur, ainsi que de son accueil dans le groupe Combustion. Par ailleurs, cette thèse n'aurait pas existée sans le financement et le support de SNECMA, et en particulier de M. Cazalens, qui a suivi ces travaux tout au long de ces trois années.

Mes remerciements vont aussi à l'ensemble des séniors de l'équipe Combustion, qui ont toujours su m'apporter une oreille attentive ainsi que des conseils pertinents qui m'ont permis de résoudre les problèmes de thésard du quotidien: Laurent, Gabriel, Olivier, Antoine, Florent et dernièrement Jérôme. En parlant de problèmes de thésard du quotidien, il est difficile de ne pas remercier Marie et Nicole pour leur aide précieuse, l'ensemble de l'équipe CSG dont le travail nous facilite grandement la vie, ainsi que toute l'administration.

Je ne manquerai pas non plus de remercier l'ensemble des thésards CFD, et en particulier la bande qui a commencée fin 2011. L'équipe Coinche: Antho, Micka, Corentin, Raph pour l'ensemble de votre oeuvre dans les domaines du Panache, de la mauvaise foi et de la Chance Insolente qui sont venus agrémenter nos pauses du midi. A la mémoire de Dédé et Jojo, qui ont su remplir nos estomacs pendant les longues soirées d'hiver. A l'équipe Canyon: Raph, Corentin, Charlie pour ces weekends passé à faire de l'huile et des toboggans. A quand, le saut du Marc ? A Micka, Antho, Corentin, Raph, Dorian, Thomas, Charlie, Adrien également, pour les nombreuses boissons à base d'eau et de malt que nous avons partagées ainsi que les bons repas mijotés par Corentin. Et à tous les sportifs qui ont dû enchaîner les séances de grimpe et de Pelote pour compenser ! Un grand merci aussi à Greg, qui m'a guidé dans les méandres d'AVBP, de l'Euler-Euler et du CERFACS à mon arrivée; ainsi qu'à David avec qui j'ai travaillé sur KIAI et qui m'a lancé sur la bonne voie, dès mes débuts. A ceux qui viennent de finir ou qui finissent bientôt: Abdulla, Manqi, Dimitrios, Thomas J., Laure, Anne, ... A l'ensemble des plus jeunes, enfin, qui se préparent bientôt à finir et qui n'en voient pas (encore) le bout.

Cette thèse a aussi donné lieu à une merveilleuse rencontre. Anne avec qui je partage ma

vie depuis quelques mois maintenant, qui a su me faire sortir de mes soirée "monotâche" et qui a su m'accompagner pendant cette période pas toujours facile. J'espère que notre belle histoire se poursuivra pendant de longues années ponctuées de beaux moments et de ptits me voyages. Finalement, je tiens à remercier ma famille qui m'a soutenu dans ma démarche et qui a participé à la conclusion de ces trois années.

Ainsi la contemplation de la flamme pérennise une rêverie première. Elle nous détache du monde et elle agrandit le monde du rêveur. La flamme est à elle seule une grande présence, mais, près d'elle, on va rêver loin, trop loin: on se perd en rêveries. La flamme est là, menue et chétive, luttant pour maintenir son être, et le rêveur s'en va rêver ailleurs, perdant son propre être, en rêvant trop grand en rêvant au monde. La flamme est un monde pour l'homme seul.

La Flamme d'une Chandelle, Gaston Bachelard (1884-1962)

À mon père.

Nomenclature

Roman characters

Symbol	Definition
$\dot{\mathcal{Q}}_{sp}$	Spark energy source term
$\mathcal{A}$	Pre-exponential constant
$\mathcal{E}$	Efficiency function
$\mathcal{F}$	Thickening factor
$\mathcal{I}_{PFI}$	Flammability indicator
$\mathcal{K}$	Flame curvature
$\mathcal{Q}_j$	Progress rate of the reaction
$\mathcal{R}$	Perfect gases universal constant
c	Progress variable
C_p	Constant pressure heat capacity
C_v	Constant volume heat capacity
D_k	Molar diffusivity of the mixture
D_{th}	Thermal diffusivity
E	Total energy
E_a	Activation energy
F_f	Flammability factor
F'_f	Flammability dispersion
h_s	Sensible enthalpy
I_{tk}	Takeno index

J	Species diffusion flux
K_{eq}	Equilibrium constant
$K_{f,j}$	Forward reaction rate
$K_{r,j}$	Reverse reaction rate
L_{sp}	Inter-injector spacing (Chap. 10)
l_t	Integral length scale
P	Pressure
P_{ign}	Ignition probability
P_{ker}	Probability of kernel initiation
q	Heat flux
s	Stoichiomtrique mass ratio
S_c	Flame consumption speed
S_d	Flame displacement speed
S_T	Turbulent flamme speed
$S_{i,j}$	Velocity deformation tensor
S_L^0	Laminar flame speed
T	Temperature
u_i	Velocity component
V^c	Correction diffusion velocity
V^k	Diffusion velocity of species k
W	Molar mass
X	Molar fraction
Y	Mass fraction
z	Mixture fraction

Non-dimensional numbers

Symbol	**Definition**
Da	Damkhöler number

Ka	Karlovitz number
Le	Lewis number
Pr	Prandtl number
Pr^t	Turbulent Prandtl number
Re	Reynolds number
Re_t	Turbulent Reynolds number
S_w	Swirl number
Sc_k	Schmidt number of species k
Sc_k^t	Turbulent Schmidt number
St	Strouhal number

Superscript

Symbol	**Definition**
sgs	Subgrid-scale contribution
t	Turbulent contribution

Greek characters

Symbol	**Definition**
χ	Scalar dissipation rate
δ_r	Reactive layer thickness
Δ_s	Energy deposit diameter (ED model)
Δ_t	Energy deposit duration (ED model)
$\delta_{i,j}$	Kronecker symbol
δ_L^0	Flame thickness
$\dot{\omega}_k$	Reaction rate of species k
$\dot{\omega}_T$	Heat release rate
η_k	Kolmogorov length scale

γ_r	Flame kernel shape ratio
κ	Flame stretch
λ	Thermal conductivity
μ	Dynamic viscosity
ν	Kinematic viscosity
ν''_{kj}	Products stoichiometric coefficient
ν'_{kj}	Reactants stoichiometric coefficient
ν_{kj}	Global stoichiometric coefficient
ν_t	SGS viscosity
ϕ	Equivalence ratio
ρ	Density
Σ	Flame surface density
τ_c	Chemical time scale
τ_k	Turbulence Kolmogorov time scale
τ_t	Turbulence integral time scale
$\tau_{i,j}$	Viscous stress tensor
ε	Dissipation rate
ε_i	Energy deposit energy (ED model)

Subscripts

Symbol	**Definition**
0	Initial state
b	Burnt gas state
c	Critical
F	Fuel
f	Fresh gas state
fl	Flame
i	i-th component

j	j-th reaction
K	Kolmogorov
k	k-th species
ker	Kernel
O	Oxidizer
st	Stoichiometric
rms	*(root mean square)*

Acronyms

Symbol	**Definition**
AV	Artificial Viscosity
CFD	Computational Fluid Dynamics
CRZ	Corner Recirculation Zone
DNS	Direct Numerical Simulation
DTF	Dynamically Thickened Flame
ED	Energy Deposition model
FCG	Flame center of gravity
IRZ	Inner Recirculation Zone
LES	Large Eddy Simulation
LW	Lax-Wendroff
MIE	Minimum Ignition Energy
NGV	Nozzle Guide Vane
NSCBC	Navier-Stokes Characteristic Boundary Condition
OPR	Overall Pressure Ratio
PDF	Probability Density Function
PEA	Pre-exponential Adjustment
PLIF	Planar Laser-Induced Fluorescence
PVC	Precessing vortex core

RANS	Reynolds Averaged Navier-Stokes
RHS	Right Hand Side
SGS	Sub-Grid Scale
SPIV	Stereo Particle Image Velocimetry
SWJ	Swirled Jet
TFLES	TF model for LES
TTGC	Two-step Taylor-Galerkin version C

Chapter 1

Introduction

Contents

1.1 Motivations

Three major constraints drive the design of modern aeronautical engines: fuel consumption, noise and pollutant emissions. These constraints are driven by the growing market competition and increasing stringency of aeronautical pollution regulations. Fuel consumption and noise emissions are mostly controlled by overall design parameters such as overall pressure ratio (OPR) or bypass ratio, and details of turbine, compressor or exhaust design. Pollutant emissions, however, are largely governed by the combustor performances so that the combustion chamber design is directly affected by the regulatory constraints. Targeted pollutants are CO_2, NO_x, CO and unburned hydrocarbons, with particular attention to NO_x due to their higher health and environmental risks (Lee *et al.*, 2010). Indeed, a strong tightening of NO_x emissions regulation has been imposed over the last two decades. Figure 1.1 illustrates the evolution of NO_x emissions standards from CAEP2 (1991) to ACARE target (2020) (Advisory Council for Aeronautics Research in Europe, 2010) along with the emission levels of a large variety of current and future engines. The aim is to lower NO_x emissions by 80% by 2020.

Two main paths are currently investigated by engine manufacturers in order to reduce fuel consumption: increase of the propulsive efficiency with new technologies such as open-rotors (Hughes

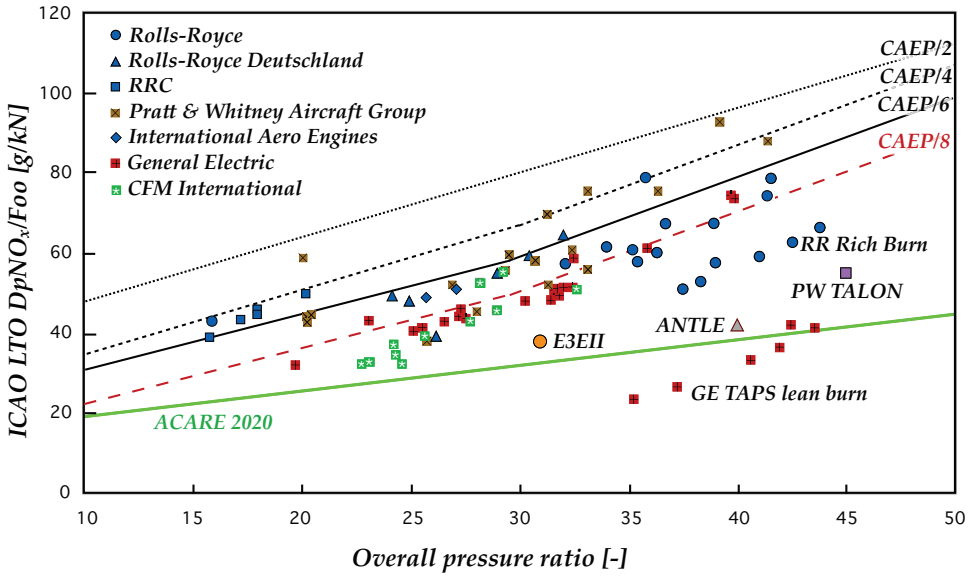

Figure 1.1: ICAO-CAEP NO_x stringency standards CAEP (2010)

& Gazzaniga, 1989) and increase of the core-engine cycle efficiency mainly through an increase of the OPR (up to 70 in the framework of the Low Emissions Core-Engine Technologies (LEMCOTEC) European project). One major drawback of increasing the OPR is the associated rise of combustor temperature, which in turns increases NO_x emissions (Lefebvre, 1998). To overcome this effect, engine manufacturers have developed several concepts: lean premixed prevaporised (LPP) (Allouis *et al.*, 2008), lean direct injection (LDI) (Read *et al.*, 2010) or multiple staged fuel injection (MSFI) (Barbosa *et al.*, 2009). As shown in Fig. 1.1, *low-NO_x* injection systems such as the GE TAPS can achieve the NO_x emissions targets set by the ACARE. *low-NO_x* designs rely on overall lean combustion to lower the maximum temperature in the combustor (Lefebvre, 1998). The design of *low-NO_x* combustors must also meet numerous constraints, the first being to guarantee a complete oxidation of fuel with a minimum pressure drop in order to maximize the overall efficiency. The design is further complicated by additional design elements required for the engine operability and maintenance: stable combustion regime without thermo-acoustic oscillation, efficient cooling of the structural elements or rapid and safe engine relight. All these requirements must be guaranteed over the wide range of operating conditions encountered in a flight envelope and often lead to contradicting technological solutions. One of the more stringent operability requirement is the relight capability: air safety regulations require engine in-flight relight capability at high altitude in the event of a flame-out. Similar constraints also drive the design of helicopter engines where the complex operational conditions require the engine to be back to full power in a handful of seconds. *low-NO_x* design increase the flow velocity in the combustor in order to reduce the equivalence ratio for a given amount of fuel. At the same time, engine designers tend to minimize the number of injection systems in order to cut down weight and maintenance costs. Both effects are detrimental to the relight capabilities and combined with the lack of feedback on these new designs, promote research for a better understanding of the ignition process in gas turbines.

1.2 Aeronautical combustion systems

1.2.1 Design of aeronautical combustors

When Frank Whittle in England and Hans Von Ohain in Germany invented the first jet engines in the 30ies, designing the combustion system appeared as an unsolvable issue. Indeed, the typical flow velocity at the compressor outlet of about 150 m/s, i.e. much higher than the turbulent flame velocity, was making the stabilization of the flame difficult. For the anecdote, H. Von Ohain, whose funding was about to be cut, tricked his sponsor using hydrogen during the demonstration of his first prototype since he could not manage to stabilize a kerosene/air flame.

Logically the first objective when designing a combustor was then to generate low velocity regions where the flame could survive. Early combustion chamber used obstacles called flame holders in the wake of which the flame was maintained. Nowadays, most combustors use swirled injection systems consisting of axial and/or radial swirlers which induce low velocity and/or backward velocity regions (Syred & Beér, 1974). Moreover, the additional rotation induces turbulence and increases mixing efficiency. Providing that the rotation is sufficiently strong, reverse flow regions are generated (Beer & Chigier, 1983) and act as a strong mechanism to stabilize the flame (Syred *et al.*, 1971). As shown in Fig. 1.2, the combustion system is generally preceded by a diffuser which smoothly reduces the incoming gas velocity with a limited pressure drop, and feeds a first cavity called the plenum which distributes the air between the injection system and the cooling of the structural parts of the combustion chamber.

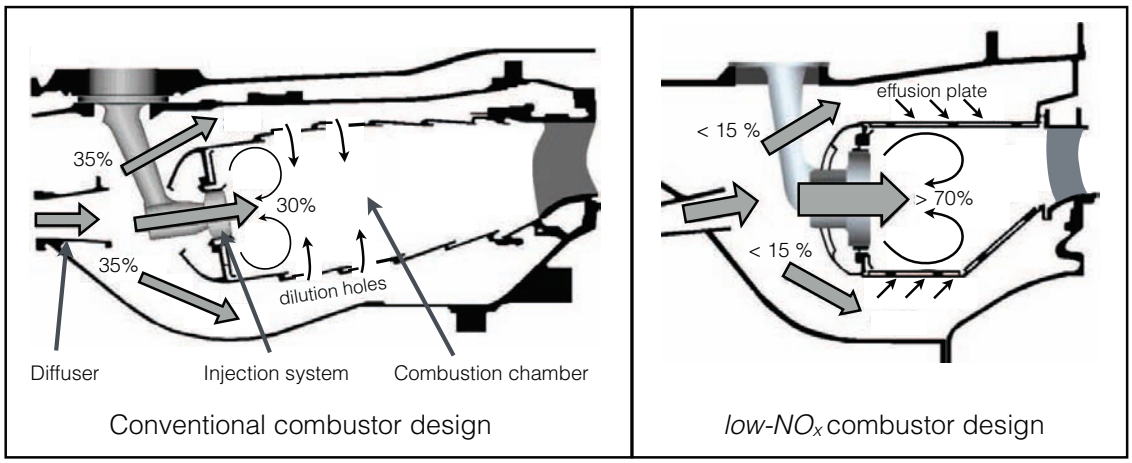

Figure 1.2: Typical design of conventional (left) versus low-NO_x (right) combustor (der Bank *et al.*, 2014).

Figure 1.2 shows both a conventional design and a *low-NO_x* concept to highlight the main differences. To achieve rapid mixing and reduction of the local equivalence ratio in the flame zone, a much larger portion of the flow goes through the injection system for *low-NO_x* design (70% vs. 30%). The combustor length is strongly reduced to minimize NO_x formation in the burnt gases since NO_x formation is directly linked to the residence time (Lefebvre, 1998). The primary zone of the conventional design located upstream of the dilution holes is suppressed. The

consequences of these technical changes are multiple:

- since most of the incoming air passes through the injection system the flame is leaner and more prone to thermo-acoustic instabilities in *low-NO_x* design.
- the reduced length of the combustor increases the temperature heterogeneities at the chamber exit, which can be destructive for the turbine.
- Since conventional design relies on low velocity and near stoichiometric conditions of the primary zone to achieve reliable ignition, *low-NO_x* design ignition capabilities are worse.

Ignition performance is usually expressed in terms of range of flight conditions over which combustion can be established. The size of the combustor is a critical design parameter that must be determined early in the design process and is generally dictated from the upper limit of the flight envelope where the relight constraint is critical (Nicholas, 2005). Indeed, the ignition capability is directly related to the residence time in the combustor, which must be higher than the ignition delay. In high altitude conditions, fuel evaporation, mixing and heat release processes are slowed down so that the ignition delays are maximum. Figure 1.3 shows the flight envelope in a Mach-altitude graph along with iso-levels of temperature. Dashed lines show how the changes of the combustor volume affects the ignition performance: from the baseline design (thick dashed line), a reduction of the combustor volume reduces the residence time and directly lowers the relight limit (Doerr, 2012). Finally, the combustor size is a trade-off between relight capability, weight and NO_x emissions.

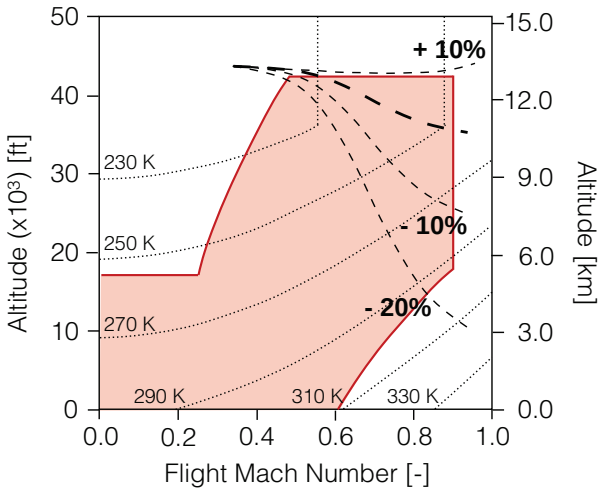

Figure 1.3: Effect of primary zone volume on the relight capability in an altitude-Mach number graph: thin dashed lines indicate ignition performances changing the combustor volume starting from an initial design (thick dashed line). Typical flight envelope (red) and isoline of temperature (dotted lines) are also reported. Adapted from (Doerr, 2012).

For conventional combustor design, engineers use a set of empirical correlations to scale the combustor dimensions adapted to new requirements, starting from an existing design (as shown is Fig. 1.3): dashed lines correspond to the empirical correlations, with the effect in a change in

the combustor volume (from -20% to +10%). These empirical design rules indicate the conditions that have been found to work in practice over a broad range of temperature, pressure and flow regime. But these rules do not rely on an appreciable understanding of the mechanisms involved nor indicate possible improvement paths. These design methods may be sufficient for conventional designs where the igniter is generally located in the primary zone of the combustor, in a region of relatively low fluid velocity and of mixture close to stoichiometry. However, *low-NO_x* designs drastically modify the flow, the spray and the spark igniter layout and these correlations do not hold anymore. The higher flow velocity at the spark position, the lower equivalence ratio, the shifted position of the spark igniter relative to the reverse flow regions have direct consequences on the flame kernel residence time at ignition, that are however not well understood. To address this issue, advanced experimental and numerical researches have been conducted over the last decade to support the design process with a sound understanding of the mechanisms in play. A specific issue of the relight constraint is that the volume of the combustion chamber must be decided early in the design process of the engine but it can only be validated late, when the combustor is installed in an experimental test bench reproducing sub-atmospheric conditions. Relight failure at this stage of the engine development would invalidate the whole design with huge financial consequences, since relight capabilities are mandatory for engine certification. The development of numerical tools able to validate the choice of the volume earlier in the design process would greatly be beneficial and help optimizing the igniter and combustor design.

1.2.2 Technologies of liquid injection systems

For their high energetic density and ease of handling, liquid fuels are employed in the vast majority of aeronautical gas turbines and must be vaporized prior to burn. In realistic high altitude conditions, the liquid phase can significantly affect the ignition performance because of the detrimental effect of the low temperature and low mass flow rate. The prime function of the injector is to increase the exchange surface between liquid and air by breaking up the liquid fuel in small droplets in order to enhance phase exchanges. Taking advantages of the strong air velocity generated by the injection system, liquid kerosene injection is generally intricately arranged with the injection system in order to efficiently atomize, disperse and evaporate the fuel. Several technologies have been developed and can be combined to ensure an efficient atomization of the liquid (Lefebvre, 1989):

- **Pressure atomizers**: the liquid fragmentation results from the pressure drop between the pressurized fuel lines and the combustion chamber pressure. The main advantage is that the droplet size is almost independent of the operating conditions but is rather controlled by the feeding line pressure and the injector nozzle design.
- **Vaporizer**: fuel is injected into a tube placed in the primary zone of the combustion chamber. The high temperature conditions around the tube allows a rapid vaporization of the fuel prior entering the combustion chamber but this can be highly detrimental to the tube lifetime due to high heat flux.
- **Air-blast atomizers**: rely on the air velocity to atomize the fuel. Fuel impacts the swirler passage walls and the resulting liquid film driven by the air flow towards an atomizing lip where the fuel is disintegrated into small droplets. This technology avoids using high

pressure supply lines, reducing the complexity and weight of the fuel system. However, at low power operation (as encountered during in-flight relight), the air velocity can be too low to ensure a sufficiently good atomization.

The fine droplets resulting from the primary and secondary atomization processes are then dispersed and mixed by the turbulent flow generated by the injection system, favoring premixed and pollutant free combustion. At in-flight relight conditions, the use of a pressure atomizer is favored since the air mass flow rate is too low to achieve fine droplets atomization with an air-blast atomizer.

1.2.3 Technologies of ignition systems

In aeronautical gas turbines, ignition is triggered by energy deposit since the conditions prior to ignition preclude the possibility of auto-ignition. Ignition systems are used to convert and transmit external energy (either electrical or chemical) to the gas and their design has a significant influence on the first phase of ignition. The igniter type, power and location are generally dictated by maintenance and accessibility constraints. For instance high power sparks may increase the ignition probability but lead to a faster erosion of the spark plug tip and more maintenance costs. Furthermore, due to the complexity of the engine auxiliary systems and the redundancy required in aviation, the space available for the igniter integration is generally very limited so that its size is an important parameter. Igniters are used in various applications with specific constraints which have led to the development of numerous researches. For instance, in spark ignited internal combustion engines, the number of ignition cycles is huge ($\simeq 10^7$) with a fairly high frequency (up to 40 Hz) and the spark must be reproducible with a high precision to avoid abnormal combustion. In gas turbines, the number of cycles and the frequency are lower but the flow conditions are less favorable for ignition success so that the power must be higher than for internal combustion engines. The major technical choices of igniter that have potential for gas turbines are a handful:

- **Spark plug** is the most commonly used igniter in gas turbines and ground transportation engines. Gas turbine sparks are usually constituted of a central electrode and a grounded outer electrode, the two being separated by a ceramic insulator. At the spark tip, the insulator terminates in a thin layer of semiconductor to ease ionization of the gap between electrodes (Lefebvre, 1998). An electrical circuit supplies a high voltage (greater than the breakdown voltage of the air gap between the electrodes) and enables to control the spark duration. Once the gas located within the gap is ionized, an intense electric arc is formed and only a small portion of its energy is transmitted to the surrounding gas (between 10% to 30% according to Teets & Sell (1988) and Maly & Vogel (1978)) due to losses in the electrical circuit, shock waves, radiation and conduction into the electrodes. Spark plugs suffer from one major drawback: their location is limited to the wall vicinity where significant heat losses to the cold wall can be encountered during the flame kernel growth.

- **Laser** is currently worked on by many research groups and is already used in lab-scale experiments (Bradley *et al.*, 2004). The purpose again in this case is to create a kernel

large and hot enough to generate a self-sustained flame. Here, the spark results from laser-induced breakdown where the photon radiation accelerates electrons at the focal point. High energy electrons are then able to ionize nearby molecules resulting in an increase of the medium opacity and the transmitted energy. Within 10 ns, a plasma approaching 100000 K and 1000 $atms$ is created in the ionized volume (Phuoc & White, 1999), which leads to the creation of a powerful shock wave (Phuoc & White, 2002). Contrary to spark plug, laser enables to control the deposit location. However, lasers are highly sensitive to high temperature so that the engine environment has prevented its use in realistic applications.

- **Torch igniter** is the combination of a spark plug and an auxiliary fuel jet (Lefebvre, 1998). It is generally employed in cryotechnic rocket engines but can also be found in gas turbines. The spark/fuel jet arrangement allows a safe ignition of the fuel jet and the hot gases produced ignite the neighbor burners. The main problem with torch igniter is its complexity and size that generally preclude its use in aeronautical gas turbines.

- **Plasma jet igniter** is close to the classical spark plug, but two successive sparks are used (Mittinti & Dabora, 1984). During the first spark, the gas contained in a small cavity at the igniter tip is ionized. The second spark induces a large overpressure in the small cavity, and a plasma jet issues from the igniter. The plasma is then located far from the combustor walls, which reduces heat losses to the walls. The main drawback of these igniters is the rapid erosion of the plasma cavity, preventing their use in spark ignition engines or gas turbines.

Current engines use classical spark plug igniters to initiate ignition sequences because of their relatively small size and ease of integration, reducing maintenance cost. However, the spark plug tip can suffer from excessive erosion due to wetting of its surface and a high energy deposit is required to overcome the effect of detrimental operating conditions and losses to the nearby walls. A better understanding of the ignition process could lead to significant improvement of the spark plug lifetime if the spark energy can be reduced and the spark position optimized.

1.3 Ignition in aeronautical gas turbines

Flame extinction inside a gas turbine can be caused by a quick modification of the air-flow through the engine during aircraft maneuvers or severe ingestion of ice or water. Even though such events are rare, the capability to perform an in-flight engine restart is mandatory and is the more stringent design criterion for the combustion chamber. The ignition of a gas turbine is a complex transient process, starting from the very small time and length scales at the spark deposit to the complete light-up of all injectors. To draw a clear picture of the numerous factors influencing the ignition process, it is generally decomposed in three successive phases identified by Lefebvre (1998) and sketched in Fig. 1.4:

- **Phase 1:** formation of flame kernel of sufficient size and temperature to be able to be propagated.

- **Phase 2:** propagation and first burner ignition to flame stabilization.

- **Phase 3:** spreading of the flame to all burners in the combustor, referred to as inter-sector flame propagation or light-round phase.

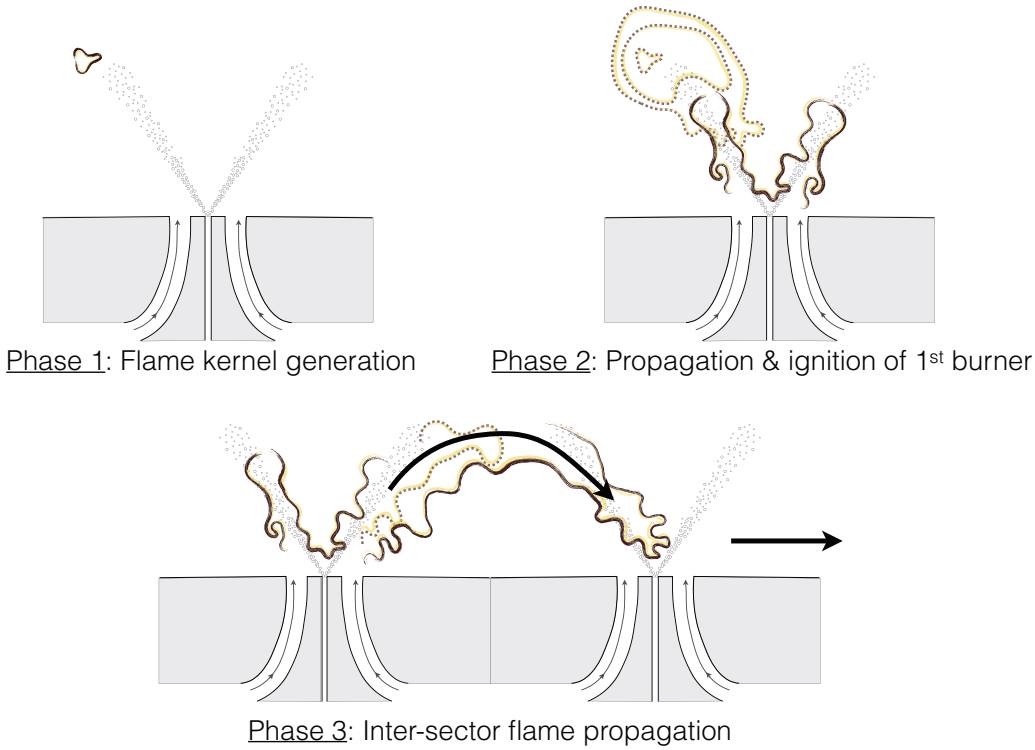

Figure 1.4: Schematic illustration of the ignition process. **Phase 1:** flame kernel creation, **Phase 2:** single burner ignition and **Phase 3:** light-around (Lefebvre, 1998).

A successful ignition is achieved if the combustor reaches a stable combustion state once the ignition system is turned off. For in-flight restart, a last phase might be added during which the progressive increase of heat release accelerates the gas turbine to its operational speed. This phase can be critical since an increase of the flow velocity could result in a blow-off if flames are not fully stabilized on the injectors. It is also interesting to note that Mastorakos (2009) split **Phase 2** into flame growth and burner ignition as distinct mechanisms. A failure of any of these steps will result in a failure of the engine ignition. This succession of phases helps to identify the critical parameters influencing each individual mechanism and point out which phase is the bottleneck to better performance.

1.3.1 Current research on ignition process

1.3.1.a Creation of a sustainable flame kernel

The igniter locally transfers energy from an auxiliary source to the flowing mixture. The ability of this energy source to initiate a sustainable flame kernel depends on multiple parameters and

it has been studied by numerous authors in the context of gas turbines (Ballal & Lefebvre, 1975; Rao & Lefebvre, 1976; Ballal & Lefebvre, 1977; Ouarti *et al.*, 2003), internal combustion engines (Pischinger & Heywood, 1990; Boudier *et al.*, 1992; Dale *et al.*, 1997; Dahms *et al.*, 2011) or fire safety (Lewis & von Elbe, 1987; Eckhoff *et al.*, 2010). The initiation of a flame kernel can be sufficiently simplified to perform theoretical studies (Zeldovich *et al.*, 1980; Deshaies & Joulin, 1984; Champion *et al.*, 1986; Vasquez-Espi & Linan, 2002): ignition can be triggered if the rate of heat released by the chemical reaction exceeds that of heat losses to the surrounding by molecular and turbulent transport. Theoretical and experimental researches introduce the concept of Minimum Ignition Energy (MIE) identified as the minimum energy required to initiate a flame kernel (Joulin, 1985; Lewis & von Elbe, 1987). The MIE is found to depend on the geometrical details of the igniter (Lewis & von Elbe, 1987; Kono *et al.*, 1984; Ko *et al.*, 1991), the mixture composition (Lewis & von Elbe, 1987; Ziegler *et al.*, 1985), the flow conditions and the turbulence level (Beduneau & Kim, 2003; Shy *et al.*, 2010; Cardin, 2013). Due to variability of both the deposited energy and initial flow field, **Phase 1** of ignition is a stochastic process. In turbulent flows, MIE is then defined statistically as the energy required to obtain typically 50% of ignition success (Kono *et al.*, 1984). The initiation of a sustainable flame kernel will be reviewed in further details in Chap. 5.

1.3.1.b Kernel growth and flame propagation

Once a flame kernel is created, it must expand and propagate to stabilize on the closest injector during **Phase 2**. Once again, the early flame growth and propagation are of interest for both gas turbines and internal combustion engines applications (Akindele *et al.*, 1982; Bradley *et al.*, 1996; Eichenberger & Roberts, 1999). As the kernel expands, it starts interacting with turbulence and transitions from a laminar to a turbulent propagating flame (Abdel-Gayed *et al.*, 1988; Bradley *et al.*, 2004). The kernel expansion has been studied in simple and well defined experimental configurations (Abdel-Gayed *et al.*, 1984; Renou, 2001; Mansour *et al.*, 2008; Galmiche *et al.*, 2012) where the effect of the turbulence on the kernel growth rate was highlighted: for low to mild turbulence, the kernel growth is enhanced by increasing turbulence intensity while for high turbulence the growth rate stabilizes then drops as velocity fluctuations are increased. These results are supported by numerous numerical studies, mainly using Direct Numerical Simulation (DNS) (Poinsot, 1991; Gashi *et al.*, 2005; Jenkins *et al.*, 2006; Fru *et al.*, 2011; Reddy & Abraham, 2013) where the turbulence is found to increase the flame surface due to wrinkling but to be also responsible for significant flame quenching. The effect on mixture composition is less studied experimentally since it requires complex experimental set-ups (Renou *et al.*, 2004; Ahmed *et al.*, 2007*b*). The shape and wrinkling of the kernel is found to be affected by the spatial distribution of fuel and in non-premixed conditions the propagation is found to be that of an edge flame. DNS allows to further investigate the effect of the mixture fraction and its gradient on the kernel growth (Chakraborty & Mastorakos, 2006; Neophytou *et al.*, 2010) and the combustion regime. The flame kernel development and subsequent flame propagation will be reviewed in further details in Chap. 5.

A detailed study of the flame propagation and subsequent stabilization on the injector nozzle necessitates the development of larger and more complex test rigs (Ahmed & Mastorakos, 2006; Ahmed *et al.*, 2007*a*; Read *et al.*, 2008; Marchione *et al.*, 2009; Garcia-Rosa *et al.*, 2011; Gebel

et al., 2012; Cordier, 2013) where sophisticated diagnostics are needed to investigate the flame front behavior. The dynamics of the flame front following the kernel phase is found to be driven by the underlying flow pattern and in non-premixed conditions the flame pathway follows the contours of stoichiometric mixture fraction and might adopt a tribranchial structure. To evaluate the ignition performance of these configurations, experimental ignition probability maps are constructed. These maps allows to distinguish favorable ignition locations with respect to the flow pattern for a given amount of energy. Ignition success is found to be correlated to the ability of the flame to reach the injector nozzle, i.e. to enter recirculation zones. These studies are supported by numerical simulations performed with Large Eddy Simulation (LES) due to the higher geometrical complexity and computational cost (Lacaze *et al.*, 2009*b*; Triantafyllidis *et al.*, 2009; Jones & Tyliszczack, 2010; Subramanian *et al.*, 2010; Jones *et al.*, 2011; Barré, 2014). As a first result, these studies prove that LES is well suited for the study of ignition sequences in single injector configuration where the non-reacting flow must be reproduced accurately to capture the subsequent flame dynamic. The detailed study of the flame structure and dynamics during the ignition transient process shows that the ability of the flame to stabilize on the injector nozzle is related to low/backward velocity regions. The direct evaluation of the ignition performance (probability maps) using brute force LES is limited by the current computational resources which do not allow to compute numerous realizations. Several methodologies have been therefore developed to estimate the ignition probability only from one non-reacting computation (Wilson *et al.*, 1999; Richardson, 2007; Neophytou *et al.*, 2012; Eyssartier *et al.*, 2013). Such methodologies allow to rapidly evaluate the ignition performance of **Phase 1** and possibly of **Phase 2** in realistic combustors at a limited computational cost. A more detailed review on the ignition probability models is proposed in Chap. 8.

1.3.1.c Light-around

In the last phase, the flame must propagate from one burner to its neighbor in order to finally light the full burner. This question is very little addressed in the open literature. The pioneering work of Boileau *et al.* (2008) focused on the ignition dynamics of a simplified annular helicopter combustor and demonstrated the capability of LES to tackle such complex flows. The authors also highlighted the effect of the burnt gases expansion on the flame propagation and the overall ignition delay but no experiments were available to validate the results. This topic has undergone recent progress with the development of in-line (Cordier, 2013) or annular (Bach *et al.*, 2013; Bourgouin *et al.*, 2013) multi-injector test rigs. Although limited to gaseous flows, these studies investigate the effect of the inter-injector spacing and the inlet mass flow rate on the light-around dynamics and shed some light on the mechanisms driving propagation and flame stabilization. Two of these test rigs are studied numerically in this thesis and will be described in Chaps. 10 & 11.

1.3.2 Application to aeronautical gas turbines

In gas turbines, the question regarding the igniter location is often raised as it directly affects the ignition performance and is strongly constrained by integration and maintenance issues. In a combustor, the local mixture and turbulence conditions can preclude ignition success regard-

less the amount of energy deposited and even if the spark is adequately located with respect to flammable mixture, the capability of the igniter to transfer energy to the gas can be strongly reduced by adverse conditions (such as wet surface of the igniter). In gas turbine, the igniter energy is then generally much higher than the MIE and the success of **Phase 1** mainly depends on the mixture flammability near the spark location (Lefebvre, 1998). The experimental and numerical studies in academic configurations clearly show that the flame kernel must be captured by the recirculation zone created by the injection system in order to increase the residence time. The increase of the flow in the combustor in *low-NO_x* design can be detrimental to the success of **Phase 2** because the increased turbulence level can quench the growing flame kernel and the higher mean flow velocity can blow the kernel out of the combustion chamber before it enters a recirculation zone. The ignition dynamics of flow at high turbulent conditions, closer to realistic conditions, is then required to investigate the full range of mechanisms controlling the ignition probability. From a design perspective, the number of injection systems sets both the distance between two consecutive injectors and the mass flow rate therethrough. These two parameters thus directly affect the light-around dynamics. In the context of cost and weight savings, the number of injection systems could be reduced, but this has a detrimental effect on the flame propagation. Due to the complexity of direct experimental investigation of the light-around mechanism in fully integrated core-engine, the development of numerical tools is a promising path to improve our understanding of the governing mechanisms. Several other phenomena not targeted in the experimental rigs listed above can affect the light-around: 1) the pressure rise during the light-around phase can induce sonic conditions at the combustor outlet which act as a bottleneck: the volume of the combustor and the design of the interface between the combustion chamber and the nozzle guide vane (NGV) can modify the hot gases expansion through the chamber; 2) the liquid fuel distribution in the combustion chamber is a crucial factor since it controls the ability of inter-sector regions to burn.

1.4 Objectives and outline

Over the last 20 years, CERFACS has developed an expertise in Computational Fluid Dynamics (CFD) and more specifically in LES with the solver AVBP co-developed by CERFACS and IFPEN. Started in the early nineties by Schönfeld & Rudgyard (1999), AVBP has been developed by numerous Ph.D. students and researchers and has been applied to study turbulent combustion in complex configurations (Selle *et al.*, 2004; Giauque *et al.*, 2005; Boileau *et al.*, 2008; Wolf *et al.*, 2012). Started with the work of Pascaud (2006) and Boileau (2007), numerical studies of ignition with AVBP have been continued by Lacaze (2009), Eyssartier (2012) and Barré (2014). The work of Boileau (2007) focused on two-phase flow ignition in both single sector and full annular simplified configurations. In the Ph.D. of Lacaze (2009), a model to mimic the spark deposit was developed and validated, and the first qualitative comparison of LES with experiments for a turbulent free methane jet showed promising results. Eyssartier (2012) built a methodology to predict ignition probability from non-reacting flow simulations. This methodology includes the local effect of the flow on the ignition success but is found to be inadequate if transport effects are dominant. Finally, Barré (2014) performed ignition sequences of the swirled burner studied in Chapter 7 but in premixed conditions. Both the early instants of ignition and overall ignition of the burner were investigated and the effect of the LES modeling parameters on the ignition

was evidenced by comparison with experiments.

The present work is sponsored by Snecma in the framework of the LEMCOTEC FP7 European project. The first objectives is to confirm the capacity of the AVBP code to predict ignition sequence and ignition statistics. Several configurations of increasing complexity are then investigated with LES, with the objective of increasing the understanding of the ignition process from the kernel phase at the early instants after energy deposit to the inter-sector flame propagation. A first part is devoted to a general description of the problem. Then, following the decomposition of the ignition sequence introduced by Lefebvre (1998), the next two parts are divided following to the successive phases of ignition:

- **Part 1** provides the baseline of combustion and computational fluid mechanics required to tackle the issue of ignition in gas turbines.

- **Part 2** focuses on the second phase of ignition. State of the art regarding **Phase 1** & **2** is first presented to underline recent advances of the scientific community and the potential for research. The LES of the partially premixed configuration of Cordier (2013) is presented and analyzed. The objectives of this LES study are two-fold: 1) confirm the capability of LES to reproduce the ignition scenarios observed in experiments as well as the ignition probability in flow conditions representative of gas turbines; 2) build an extensive LES database to identify the mechanisms leading to ignition success or failure in complex flow configurations. Finally, the LES database is used to construct and validate a new model for the prediction of ignition probability map based on non-reacting flow solutions. The model is built to encompass non-local flow effects that have been observed in both LES and experiments.

- **Part 3** is dedicated to the light-around phase. The study is built around two experimental setups: 1) the configuration of Cordier (2013) featuring a variable spacing capability is first studied and highlights some of the mechanisms responsible for flame propagation; 2) the azimuthal configuration of Bourgouin *et al.* (2013) is then computed to analyze the complete light-around and evidence the effect of the burnt gases expansion on the propagation.

Part I

Turbulent reactive flows

Chapter 2

Conservation equations for turbulent reactive flows

Contents

Fluid mechanics is the study of motion of liquid and/or gases. The mathematical description of fluid motion started in 1757 with the set of governing equations describing inviscid flows reported by Leonhard Euler (and called after him Euler equations). Then Claude-Louis Navier introduced the notion of viscosity in 1822 and George Stokes wrote the final set of equations describing the motion of viscous fluids in 1845. These equations are known as the 'Navier-Stokes equations' of fluid motion. From a mathematical point of view, these equations are nonlinear partial differential equations and, except in simple canonical cases, cannot be solved analytically. The equations for turbulent reactive flows include chemical source terms, and additional transport equations for species mass fractions involved in the chemical reactions are solved.

The aim here is to introduce the main variables describing reactive flows as well as the physical models used in the multispecies Navier-Stokes equations solved in AVBP. The derivation can be found in fluid mechanics textbooks such the one of Kuo (2005).

2.1 Multispecies thermodynamics

Dealing with combustion requires to describe multispecies mixtures, where each species k is characterized by its:

- mass fraction: $Y_k = m_k/m$, the ratio of the mass of species k, m_k over the total mixture mass m.

- density: $\rho_k = \rho Y_k$, where ρ is the density of the mixture
- molar mass of species k: W_k
- molar fraction of species k: $X_k = \frac{W}{W_k} Y_k$, where W is the molar mass of the mixture
- molar concentration of species k: $[X_k] = \rho \frac{X_k}{W}$
- constant pressure mass heat capacity: $C_{p,k}$
- mass enthalpy: $h_k = h_{s,k} + \Delta h^0_{f,k}$, where $h_{s,k} = \int_{T_0}^{T} C_{p,k} dT$ is the sensible enthalpy and $\Delta h^0_{f,k}$ is the formation enthalpy at reference temperature T_0

By construction, for a mixture composed of N species, $\sum_{k=1}^{N} Y_k = 1$, the mixture molar mass is given by:

$$\frac{1}{W} = \sum_{k=1}^{N} \frac{Y_k}{W_k} \tag{2.1}$$

Under the hypothesis of perfect gases, the mixture total pressure P is the sum of partial pressures p_k of each species:

$$P = \sum_{k=1}^{N} p_k \quad \text{where} \quad p_k = \rho_k \frac{\mathcal{R}}{W_k} T \tag{2.2}$$

where T is the mixture temperature and $\mathcal{R} = 8.314\ J.mol^{-1}.K^{-1}$ is the perfect gas universal constant. The equation of state yields:

$$p = \sum_{k=1}^{N} p_k = \sum_{k=1}^{N} \rho_k \frac{\mathcal{R}}{W_k} T = \rho \frac{\mathcal{R}}{W_k} T \tag{2.3}$$

The constant pressure mass heat capacity of the mixture C_p is given by:

$$C_p = \sum_{k=1}^{N} Y_k C_{p,k} \tag{2.4}$$

2.2 Navier-Stokes equations

The Navier-Stokes equations for multispecies mixtures using Einstein index notation write:

$$\frac{\partial \rho u_j}{\partial t} + \frac{\partial \rho u_i u_j}{\partial x_i} + \frac{\partial P \delta_{ij}}{\partial x_i} = -\frac{\partial \tau_{ij}}{\partial x_i} \quad \text{for} \quad j = 1, 3 \tag{2.5}$$

$$\frac{\partial \rho Y_k}{\partial t} + \frac{\partial \rho u_i Y_k}{\partial x_i} = -\frac{\partial J_{i,k}}{\partial x_i} + \dot{\omega}_k \quad \text{for} \quad k = 1, N \tag{2.6}$$

$$\frac{\partial \rho E}{\partial t} + \frac{\partial \rho u_i E}{\partial x_i} + \frac{\partial u_j P \delta_{ij}}{\partial x_i} = -\frac{\partial q_i}{\partial x_i} + \frac{\partial u_j \tau_{ij}}{\partial x_i} + \dot{\omega}_T + \dot{\mathcal{Q}}_{sp} \tag{2.7}$$

with u_j is the j^{th}-component of the velocity, P is the static pressure, τ_{ij} is the viscous tensor, $J_{i,k}$ is the i^{th}-component of the diffusive flux of species k, $\dot{\omega}_k$ and $\dot{\omega}_T$ are the species k and energy chemical source term, E is the total energy, q_i is the i^{th}-component of the energy flux and $\mathcal{Q}_{sp}$ is the external energy source term, limited in this study to the spark. δ_{ij} is the Kronecker symbol equal to 1 if $i = j$ and 0 otherwise. Eqs. (2.5)-(2.7) are referred to as the momentum, k^{th}-species and energy conservation equations respectively.

The viscous tensor is proportional to the symmetric part of the deformation tensor (Newtonian fluid), and equality between mechanical and thermodynamic pressure (zero coefficient of bulk viscosity null, Stokes assumption) is assumed:

$$\tau_{ij} = 2\mu \left(S_{ij} - \frac{1}{3}\delta_{ij} S_{kk} \right) \tag{2.8}$$

with μ the dynamic viscosity and S_{ij} the deformation tensor:

$$S_{ij} = \frac{1}{2}\left(\frac{\partial u_j}{\partial x_i} + \frac{\partial u_i}{\partial x_j} \right) \tag{2.9}$$

The computation of the exact formulation of the diffusive flux of species k in the mixture is a very complex task. The Hirschfelder and Curtiss approximation (Hirschfelder *et al.*, 1969) is employed, yielding:

$$J_{i,k} = \rho Y_k V_{k,i} = -\rho \left(D_k \frac{W_k}{W} \frac{\partial X_k}{\partial x_i} - Y_k V_i^c \right) \tag{2.10}$$

with D_k the equivalent diffusion coefficient of species k in the rest of the mixture:

$$D_k = \frac{1 - Y_k}{\sum_{j \neq k} X_j / D_{jk}} \tag{2.11}$$

where D_{jk} is the binary diffusion coefficient of species j in species k. V_i^c in Eq. (2.10) is the correction velocity ensuring global mass conservation:

$$V_i^c = \sum_{k=1}^{N} D_k \frac{W_k}{W} \frac{\partial X_k}{\partial x_i} \tag{2.12}$$

The chemical source term $\dot{\omega}_k$ in the species conservation equation is described in Sec. 2.4. The energy flux is the combination of the Fourier flux and the enthalpy flux induced by species diffusion:

$$q_i = -\lambda \frac{\partial T}{\partial x_i} + \sum_{k=1}^{N} J_{i,k} h_{s,k} \tag{2.13}$$

where λ is the heat conduction coefficient of the mixture. Finally the reaction energy source term is linked to the species source terms by:

$$\dot{\omega}_T = -\sum_{k=1}^{N} \Delta h_{f,k}^0 \dot{\omega}_k \tag{2.14}$$

2.3 Transport properties

Simple transport models are used. The dynamic viscosity μ of the mixture is supposed independent of the species composition and only depends on the temperature through a standard power law:

$$\mu = \mu_0 \left(\frac{T}{T_0} \right)^b \tag{2.15}$$

where the exponent b depends on the mixture and typically lies between 0.6 and 1.0. The species diffusion coefficient is evaluated assuming a constant Schmidt number Sc_k for each species k that yields:

$$D_k = \frac{\mu}{\rho Sc_k} \tag{2.16}$$

The Schmidt number is a dimensionless number that compares the viscous and species diffusion rates. Similarly, the thermal conductivity λ is computed assuming constant a Prandtl number Pr of the mixture:

$$\lambda = \frac{\mu C_p}{Pr} = \rho C_p D_{th} \quad \text{with} \quad D_{th} = \frac{\nu}{Pr} \tag{2.17}$$

where the Prandtl number compares the viscous and thermal diffusion rates. Finally, the Lewis number Le_k that compares the thermal and species diffusion rates is introduced as:

$$Le_k = \frac{D_{th}}{D_k} = \frac{Sc_k}{Pr} \tag{2.18}$$

2.4 Chemical kinetics

N species reacting through M reactions are considered:

$$\sum_{k=1}^{N} \nu'_{kj} \mathcal{M}_k \Longleftrightarrow \sum_{k=1}^{N} \nu''_{kj} \mathcal{M}_k \quad \text{for } \; j = 1, M \tag{2.19}$$

where $\mathcal{M}_k$ is the symbol for species k, ν'_{kj} and ν''_{kj} are the molar stoichiometric coefficients of species k in reaction j. The reaction rate $\dot{\omega}_k$ of species k is the sum of all reaction rates $\dot{\omega}_{k,j}$ in reaction j:

$$\dot{\omega}_k = \sum_{j=1}^{M} \dot{\omega}_{k,j} = W_k \sum_{j=1}^{M} \nu_{kj} \mathcal{Q}_j \tag{2.20}$$

where $\nu_{kj} = \nu''_{kj} - \nu'_{kj}$ and $\mathcal{Q}_j$ is the progress rate of reaction j. Total mass conservation yields:

$$\sum_{k=1}^{N} \dot{\omega}_k = 0 \tag{2.21}$$

The progress rate of reaction j is given by:

$$\mathcal{Q}_j = K_{fj} \prod_{k=1}^{N} \left(\frac{\rho Y_k}{W_k} \right)^{\nu'_{kj}} - K_{rj} \prod_{k=1}^{N} \left(\frac{\rho Y_k}{W_k} \right)^{\nu''_{kj}} \tag{2.22}$$

K_{fj} and K_{rj} are the forward and reverse reaction rates of reaction j respectively. The forward reaction rate is described with an Arrhenius law:

$$K_{fj} = \mathcal{A}_j \exp\left(-\frac{E_{aj}}{\mathcal{R}T} \right) \tag{2.23}$$

where $\mathcal{A}_j$ and E_{aj} are the pre-exponential factor and the activation energy of reaction j respectively. At a molecular level, the Arrhenius law describes the probability that an atom exchange occurs due molecular collisions. The reverse reaction rate is given by:

$$K_{rj} = \frac{K_{fj}}{K_{eq,j}} \tag{2.24}$$

with $K_{eq,j}$ the equilibrium constant, defined following Kuo (2005):

$$K_{eq,j} = \left(\frac{P_0}{\mathcal{R}T} \right)^{\sum_{k=1}^{N} \nu_{kj}} \exp\left(\frac{\Delta S_j^0}{\mathcal{R}} - \frac{\Delta H_j^0}{\mathcal{R}T} \right) \tag{2.25}$$

where $P_0 = 1\ bar$, ΔH_j^0 and ΔS_j^0 are the enthalpy and entropy changes for reaction j respectively:

$$\Delta H_j^0 = h(T) - h(0) = \sum_{k=1}^{N} \nu_{kj} W_k (h_{s,k} + \Delta h_{f,k}^0) \tag{2.26}$$

$$\Delta S_j^0 = \sum_{k=1}^{N} \nu_{kj} W_k s_k(T) \tag{2.27}$$

where s_k is the entropy of species k.

Chapter 3

Fundamentals of turbulent combustion

Contents

3.1 Introduction

The power required by aeronautic gas turbines implies to burn a large amount of fuel in a fairly small part of the engine. The high velocity flow coming from the compressor generates highly turbulent conditions that favor high heat release density and generate a partial premixing of the fuel with incoming air. As a consequence, a gas turbine is a turbulent partially premixed application. However, ignition is a transient process during which a wide variety of combustion regimes can be encountered. These regimes have been identified by the combustion community and are classically classified depending on the quality of the mixing between fuel and oxidizer prior to combustion (premixed or non-premixed) and the flow flow regime (laminar or turbulent).

The objective here is not to give an exhaustive description of all the combustion regimes, but to provide an overview of the mechanisms controlling the flame propagation, relevant for ignition problems. A complete description can be found in classical textbooks of Poinsot & Veynante (2011), Kuo (2005) or Peters (2000). The structure and propagation mechanism of laminar flames

is described in Sec. 3.2 while Sec. 3.3 focuses on turbulent flames with a brief reminder of some elements of turbulence.

3.2 Laminar flames

Focusing first on laminar flames is relevant for ignition applications since flame propagation may be initiated in this regime. The description of laminar flames is also a prerequisite to study turbulent combustion and many turbulent flame theories are derived from laminar flames.

3.2.1 Laminar premixed flame

3.2.1.a Laminar premixed flame characteristics

Mixture composition

Combustion generally involves numerous intermediate species and reactions to convert the reactant and oxidizer into combustion products. From a macroscopic point of view, combustion reduces to a redox reaction. The equivalence ratio ϕ is, together with the temperature and the pressure, characteristic of the fresh gas mixtures. Considering ν'_F and ν'_O, the stoichiometric coefficients of fuel and oxidizer respectively, the redox reaction writes:

$$\nu'_F F + \nu'_O O \rightarrow Products \tag{3.1}$$

The mixture is said stoichiometric when the fuel and oxidizer mass fractions of the fresh gases Y_F and Y_O follow:

$$\left(\frac{Y_O}{Y_F}\right)_{st} = \frac{\nu'_O W_O}{\nu'_F W_F} = s \tag{3.2}$$

where W_F and W_O are the molar mass of fuel and oxidizer respectively, s is the mass stoichiometric ratio and the subscript st denotes stoichiometric conditions. The equivalence ratio ϕ is given by:

$$\phi = s\frac{Y_F}{Y_O} = \left(\frac{Y_F}{Y_O}\right) \Big/ \left(\frac{Y_F}{Y_O}\right)_{st} \tag{3.3}$$

A mixture having $\phi > 1$ is called rich (excess of fuel) while lean mixture corresponds to $\phi < 1$ (excess of oxidizer).

Flame structure

In a one-dimensional stationary case, the reactive Navier-Stokes equations (2.5-2.7) can be simplified. The thermal theory proposed by Zeldovich, Frank-Kamenetski and Von Karman (ZFK) (Zeldovitch & Frank-Kamenetskii, 1938) is the first theoretical treatment of stationary one-dimensional flames. The ZFK analysis assumes a single-step global reaction with an Arrhenius type reaction rate and a high activation energy, unity Lewis number for all species and first

order dependance of the reaction rate to fuel and oxidizer. The flame front is then described by a single differential equation and can be viewed as a wave propagating from the burnt gases toward the fresh gases at a constant velocity S_L^0 (Zeldovitch & Frank-Kamenetskii, 1938):

$$\rho_u S_L^0 \frac{dT}{dx} = \frac{d}{dx}\left(\frac{\lambda}{C_p}\frac{dT}{dx}\right) - \frac{Q}{C_p}\omega \tag{3.4}$$

The authors also introduced the thermal structure of the laminar flame, as sketched in Fig. 3.1.

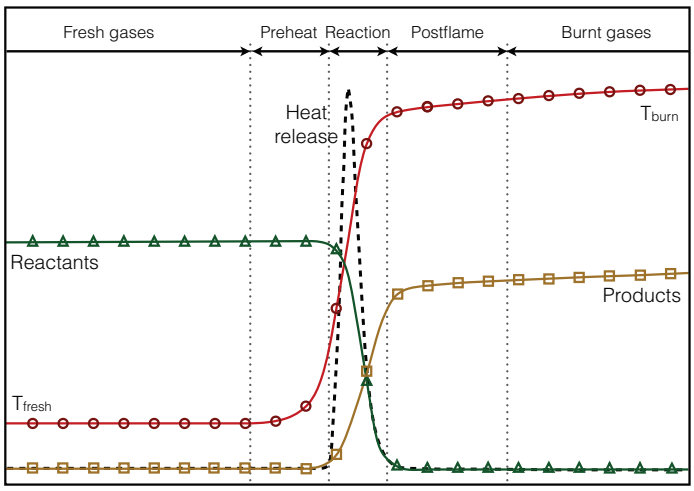

Figure 3.1: Schematic description of the laminar premixed flame structure.

Several characteristic zones can be identified from left (fresh gases) to right (burnt gases):

- the **preheat zone**, chemically inert, where heat diffuses progressively from the reaction zone and increases the gas temperature.
- the **reaction layer** where the fuel is decomposed in smaller hydrocarbons which react with radicals (O or H) to create secondary species such as CO, C_2 or H_2. The reaction layer has a thickness δ_r.
- the **post-flame region** where secondary species are transformed in final products of the reaction such as CO_2 or H_2O.

Most of the heat is released in the reaction layer, characterized by a strong temperature gradient. The chain branching reactions occurring in the reaction layer involve small hydrocarbons and free radicals at high reactions rates. On the contrary, the recombination reactions occurring in the post-flame region are much slower, and this region is much thicker than the reaction region.

Laminar flame speed

The ZFK thermal theory also derives an explicit expression of the laminar flame speed as a function of the thermal diffusivity D_{th} and the Arrhenius pre-exponential factor $\mathcal{A}$. The derivation assumes a null reaction rate in the preheat zone and a negligible convection term in the

reaction layer: from Eq. (3.4) the temperature balance can be written in both regions and an expression for S_L^0 is obtained by equating the temperature gradient at the frontier between these two regions:

$$S_L^0 \propto \sqrt{D_{th}\mathcal{A}} \tag{3.5}$$

Laminar flame thickness

The laminar flame thickness is a crucial flame characteristic, often required in combustion models for RANS or LES. Indeed, the size of the flame front is a critical parameter that controls the resolution required in numerical simulation. Several definitions of the laminar flame thickness are reported in the literature, among which:

- The diffusion thickness δ is based on the thermal diffusion of fresh gases (Poinsot & Veynante, 2011):

$$\delta = \frac{\lambda(T_f)}{\rho(T_f)C_p(T_f)S_L^0} = \frac{D_{th}}{S_L^0} \propto \sqrt{\frac{D_{th}}{\mathcal{A}}} \tag{3.6}$$

  where the subscript f denotes the fresh gases. This definition, which directly derives from the ZFK asymptotic theory, provides an estimation of the flame thickness. In practice the result is too approximate to determine the required mesh resolution.

- The thermal thickness δ_L^0 is based on the temperature gradient and is generally used to estimate the grid resolution required in LES or DNS computations:

$$\delta_L^0 = \frac{T_b - T_f}{max(|\nabla T|)} \tag{3.7}$$

  where the subscript b denotes the burnt gases. The computation of a 1D laminar flame allows to estimate the flame thermal thickness.

- The reaction layer thickness δ_r can also be used to estimate the flame thickness with $\delta_r = \delta_L^0/\beta$, where β is given by:

$$\beta = \alpha\frac{E_a}{\mathcal{R}T_b} \quad \text{and} \quad \alpha = \frac{T_b - T_f}{T_b} \tag{3.8}$$

  The parameters α and β measure the heat release by the flame and the activation energy respectively. Since typical values of β range between 10 and 20, $\delta_r < \delta_L^0$ and using this definition leads to stronger mesh resolution constraint.

3.2.1.b Laminar premixed flame propagation

Considering multi-dimensional laminar premixed flames in non-uniform flow, additional notions are required to investigate the flame propagation.

Definitions of flame speed

The front propagation speed is an intrinsic characteristic of laminar premixed flames. Theoretical descriptions of premixed flame propagation reduce the front to an interface between fresh and burnt gases. A progress variable c is therefore introduced. It could be any variable that ensures a monotonical behavior from 0 in the fresh gases to 1 in the burnt gases. Under the assumption of unity Lewis number, the definition of c can be based on the fuel mass fraction or on the mixture temperature such as:

$$c = \frac{Y_F - Y_{F,f}}{Y_{F,b} - Y_{F,f}} = \frac{T - T_f}{T_b - T_f} \tag{3.9}$$

leading to $c = 0$ in the fresh gases and $c = 1$ in the burnt gases. The flame front may be represented by an iso-surface of progress variable:

$$c(\boldsymbol{x}, t) = c^* \tag{3.10}$$

On this surface, the normalized local gradient of c defines the flame front normal direction:

$$\boldsymbol{n} = -\frac{\boldsymbol{\nabla} \boldsymbol{c}}{|\boldsymbol{\nabla} \boldsymbol{c}|}\bigg|_{c=c^*} \tag{3.11}$$

Using this convention, the normal is pointing towards the fresh gases. Several definitions of the flame speed based on the kinematic or chemical properties of the flame can be defined as illustrated in Fig. 3.2:

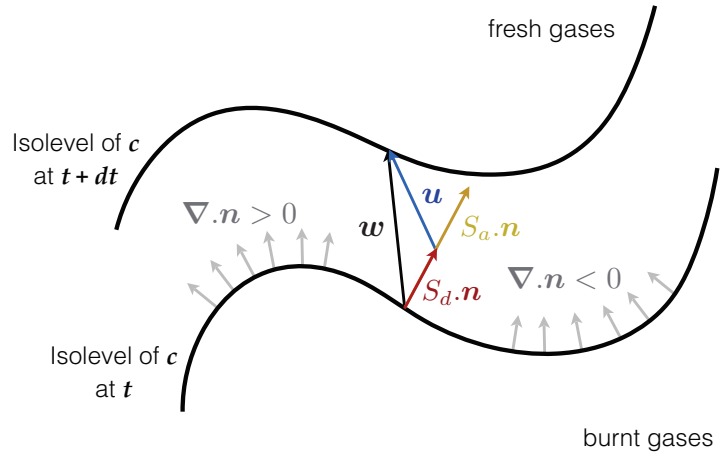

Figure 3.2: Notations for flame speed definitions following Poinsot & Veynante (2011).

- $\boldsymbol{w}$ is the local **flame front velocity** in a fixed reference frame and its definition derives from the differentiation of Eq. (3.10) with respect to time t (Peters, 2000)):

$$\frac{\partial c}{\partial t} + \boldsymbol{\nabla} \boldsymbol{c} \cdot \frac{\partial x}{\partial t}\bigg|_{c=c^*} = \frac{\partial c}{\partial t} + \boldsymbol{\nabla} \boldsymbol{c} \cdot \boldsymbol{w} = 0 \tag{3.12}$$

- S_a is the **absolute speed**, projection of $\boldsymbol{w}$ on the flame front normal $\boldsymbol{n}$. Using Eqs. 3.12 and 3.11, S_a is expressed as a function of c:

$$S_a = \boldsymbol{w} \cdot \boldsymbol{n} = \frac{1}{|\boldsymbol{\nabla} \boldsymbol{c}|} \frac{\partial c}{\partial t} \tag{3.13}$$

- S_d is the **displacement speed** of the flame relative to the underlying gaseous velocity $\boldsymbol{u}$, i.e. the difference between the absolute front flame velocity S_a and the flow velocity $\boldsymbol{u}$ projected on the flame normal. S_d is also expressed as a function of c:

$$S_d = S_a - \boldsymbol{u} \cdot \boldsymbol{n} = \frac{1}{|\boldsymbol{\nabla} \boldsymbol{c}|} \frac{\partial c}{\partial t} + \boldsymbol{u} \cdot \frac{\boldsymbol{\nabla} \boldsymbol{c}}{|\boldsymbol{\nabla} \boldsymbol{c}|} = \frac{1}{|\boldsymbol{\nabla} \boldsymbol{c}|} \frac{Dc}{Dt} \tag{3.14}$$

where D/Dt is the total derivative. Note that S_a and S_d are defined only on the flame front and derived only from the geometrical properties of the front. Gibson (1968) derived an expression for the displacement speed for non-reacting scalar, extended by Peters (2000) to take into account the chemical source term:

$$S_d = \left[\frac{\boldsymbol{\nabla} \cdot (\rho D_c \boldsymbol{\nabla} \boldsymbol{c}) + \dot{\omega}_c}{\rho |\boldsymbol{\nabla} \boldsymbol{c}|} \right]_{c=c^*} \tag{3.15}$$

where $\dot{\omega}_c$ is the chemical energy or species source term depending on the definition of c and D_c is the thermal or species diffusivity depending on the definition of c. Gran *et al.* (1996), Echekki & Chen (1999) and Peters *et al.* (1998) showed that the diffusive term appearing in Eq. (3.15) may be split into two contributions, one accounting for tangential diffusion and another one for diffusion normal to the iso-surface $c = c^*$:

$$\boldsymbol{\nabla} \cdot (\rho D_c \boldsymbol{\nabla} \boldsymbol{c}) = \underbrace{\boldsymbol{n} \cdot \boldsymbol{\nabla} (\rho D_c \boldsymbol{n} \cdot \boldsymbol{\nabla} \boldsymbol{c})}_{normal\ diffusion} \underbrace{-\rho D_c |\boldsymbol{\nabla} \boldsymbol{c}| \boldsymbol{\nabla} \cdot \boldsymbol{n}}_{tangential\ diffusion} \tag{3.16}$$

Finally, the displacement speed (on the iso-surface $c = c^*$) can be rewritten such as:

$$S_d = \underbrace{\frac{\boldsymbol{n} \cdot \boldsymbol{\nabla} (\rho D_c \boldsymbol{n} \cdot \boldsymbol{\nabla} \boldsymbol{c})}{\rho |\boldsymbol{\nabla} \boldsymbol{c}|}}_{normal\ diffusion} - \underbrace{D_c \boldsymbol{\nabla} \cdot \boldsymbol{n}}_{tangential\ diffusion} + \underbrace{\frac{\dot{\omega}_c}{\rho |\boldsymbol{\nabla} \boldsymbol{c}|}}_{reaction} \tag{3.17}$$

It is important to note that S_d is governed by the local balance between diffusion and reaction. The flame structure sketched in Fig. 3.1 is such that the diffusion/convection process dominates in the preheat zone while the reaction/diffusion process is important in the reaction layer. As a consequence, the magnitude of S_d components are changing through the flame front. To account for the gas expansion through the flame front, the density-weighted flame displacement speed noted S_d^* is generally preferred:

$$S_d^* = \frac{\rho}{\rho_f} S_d \tag{3.18}$$

- S_c is the **consumption speed** defined by the mass conservation across the flame front:

$$S_c = -\frac{1}{\rho(T_f) Y_{F,f}} \int_{-\infty}^{\infty} \dot{\omega}_F \, d\boldsymbol{n} \tag{3.19}$$

The consumption speed is the only global quantity. For this reason, the consumption speed is usually preferred when analyzing reactive flows, but its computation in complex tridimensional turbulent flames is not an easy task. Note that for an unstretched laminar premixed flame, the different flame speeds are related by:

$$S_L^0 = S_c = \frac{\rho}{\rho_f} S_d \tag{3.20}$$

Definition of stretch and effect on the flame front

The total flame stretch κ is defined as the time derivative of the fractional rate of a flame surface element A (Williams, 1985):

$$\kappa = \frac{1}{A}\frac{dA}{dt} \tag{3.21}$$

κ can be decomposed into a tangential strain rate contribution and a term accounting for the effect of flame front curvature (Candel & Poinsot, 1990):

$$\kappa = \underbrace{-\boldsymbol{nn} : \boldsymbol{\nabla u} + \boldsymbol{\nabla} \cdot \boldsymbol{u}}_{Tangential\ strain\ rate} + \underbrace{S_d \boldsymbol{\nabla} \cdot \boldsymbol{n}}_{Curvature} \tag{3.22}$$

where $\boldsymbol{nn} : \boldsymbol{\nabla}$ is the gradient operator normal to the flame surface. From Eq. (3.22), the rate of change of the flame surface area is obviously related to both the flow aerodynamics and the shape of the flame surface.

For stretched flames, it is not straightforward neither experimentally nor numerically to evaluate accurately the flame speed. Under the assumption of small strain rate and curvature contributions, using an asymptotic theory is the only way to obtain the flame response to stretch (Bush & Fendell, 1970; Clavin, 1985; Williams, 1985). The displacement and the consumption speeds are found to have a linear but different response to stretching:

$$\frac{S_d}{S_L^0} = 1 - M_a^d \frac{\kappa \delta_{th}}{S_L^0} \quad \text{and} \quad \frac{S_c}{S_L^0} = 1 - M_a^c \frac{\kappa \delta_{th}}{S_L^0} \tag{3.23}$$

where $\kappa\delta_{th}/S_L^0$ is a reduced Karlovitz number based on the diffusive thickness (Peters, 1986), that compares the chemical and small turbulence time scales. M_a^d and M_a^c are the Markstein numbers for the displacement and the consumption speeds respectively, proportional to the fuel Lewis number $(Le_F - 1)$. The Markstein numbers compare the stability wavelength of a curved flame (called Markstein length) to the thermal thickness of the flame front δ_L^0. The stability of the flame front depends on the sign of the Markstein number: for the displacement speed natural intrinsic thermo-diffusive instabilities of the flame front arise for negative Markstein numbers (Clavin, 1985). The typical asymptotic behavior of the consumption speed for stagnation flames is illustrated in Fig. 3.3 as a function of stretch for different values of the fuel Lewis number:

- For $Le_F = 1$, species and temperature gradients increase in the same proportions when increasing stretch. As a consequence, the flame is thinner but the consumption speed is not affected, at least for small stretch values.

- For $Le_F < 1$, the consumption Markstein number is negative and the consumption speed linearly increases with stretch, in the limit of small stretch values.
- For $Le_F > 1$, the consumption speed decreases with stretch.

In general for an adiabatic flame, quenching can be observed only for very large values of stretch but when heat losses are taken into account, extinction could occur for lower stretch values. For large values of stretch, the asymptotic theory is no longer valid, but numerical simulations showed that the linear response could still be applicable beyond the assumption of small stretch values with reasonable accuracy (Meneveau & Poinsot, 1991).

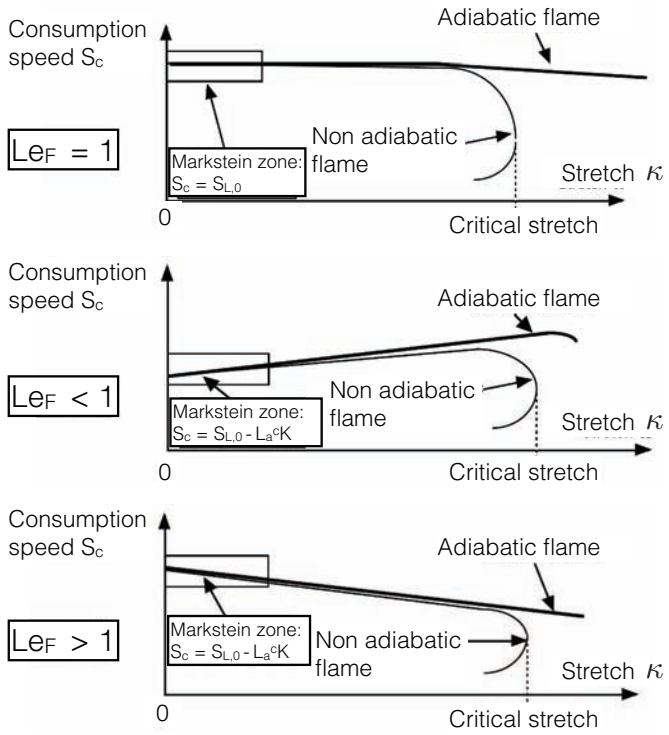

Figure 3.3: Asymptotic response of consumption speed to strain rate for different Lewis numbers (Poinsot & Veynante, 2011).

3.2.2 Laminar diffusion flame

In many applications, fuel and oxidizer are introduced separately in the combustion chamber, mainly to ensure a safe fuel storage. Depending on the design and the operating conditions, a partial premixing of fuel and oxidizer is achieved before burning and/or a reactive layer is found at the interface between fuel and oxidizer. In that sense, diffusion flames differ from premixed flames since they do not propagate and cannot be viewed as waves of finite speed and thickness.

Flame structure

The diffusion flame is sustained by diffusion of fuel and oxidizer towards the reaction zone, located around the stoichiometric mixture region. A schematic illustration of a diffusion flame structure is shown in Fig. 3.4.

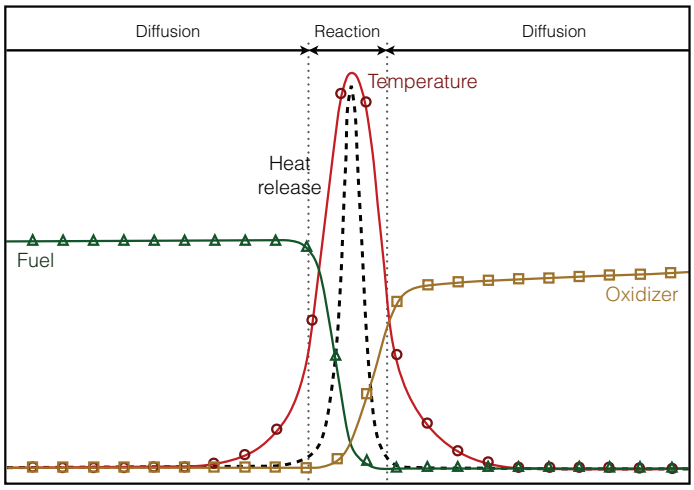

Figure 3.4: Schematic description of the laminar diffusion flame structure.

Flame characteristics

Two main length scales are related to diffusion flames (Bilger, 1989):

- **the diffusion layer thickness** l_d corresponds to the layer of the zone where the mixture fraction z goes from 0 to 1 and where fuel and oxidizer may coexist and diluted by combustion products.
- **the reaction zone thickness** l_r corresponds to the zone where reaction occurs and typically lies around the stoichiometric mixture fraction z_{st}.

These scales are not equivalent to the premixed flame thermal and reactive thicknesses defined in Sec. 3.2.1.a since they can evolve separately and depend on the flow conditions. A laminar diffusion flame can be characterized by the Damköhler number:

$$Da^{fl} = \frac{\tau_f}{\tau_c} \tag{3.24}$$

where the flow time scale can be estimated from the scalar dissipation rate at the stoichiometric point $\tau_f = \chi_{st}^{-1}$ (Libby & Williams, 1994) where $\chi = 2D(\boldsymbol{\nabla} \boldsymbol{z})^2$ and z is the mixture fraction. Since χ_{st} measures the mixture fraction gradient, it can also be used to estimate the diffusion layer thickness $l_d \simeq \sqrt{D/\chi_{st}}$. Asymptotic theories (Linan, 1974) prove that the reaction and diffusion layer thicknesses can be related through the flame Damköhler number Da^{fl}:

$$\frac{l_r}{l_d} \simeq (Da^{fl})^{-1/a} \tag{3.25}$$

where $a = \nu'_F + \nu'_O + 1$ is obtained from the stoichiometric coefficients of the global fuel redox reaction.

To describe non-premixed combustion, the mixture fraction z which is a chemistry-independent "conserved scalar" variable is essential. The conserved scalar satisfies the non-reactive transport equation:

$$\rho\frac{\partial z}{\partial t} + \rho\boldsymbol{u}\cdot\boldsymbol{\nabla z} = \boldsymbol{\nabla}\cdot(\rho D\boldsymbol{\nabla z}) \tag{3.26}$$

where D is the diffusivity (either thermal or species depending on the definition of z). All scalar quantities of the flow (temperature, concentration or density) are then uniquely related to the mixture fraction, which in turns decouple mixing from combustion. In this work, the mixture fraction is defined following Bilger (1989) and based on the coupling function β (Williams, 1985):

$$z = \frac{\beta - \beta_0}{\beta_1 - \beta_0} \tag{3.27}$$

with

$$\beta = \sum_{l=1}^{N_e}\gamma_l\sum_{k=1}^{N_s}\frac{a_{l,k}W_lY_k}{W_k} \tag{3.28}$$

where β_0 and β_1 are the of β evaluated in the fuel and oxidizer streams respectively, γ_l and W_l are the weighting factor and the atomic weight of the element l respectively, and $a_{l,k}$ is the number of atoms of element l in one molecule of species k. The choice of Bilger for γ_l is used in this work with $\gamma_C = 2/W_C$, $\gamma_H = 1/(2W_H)$, $\gamma_O = -1/W_O$ and $\gamma_N = 0$. Note that the definition of the mixture fraction is restricted to cases where the Schmidt numbers of all species are equal since preferential diffusion effects arising from non-equal Schmidt numbers do not lead to a passive scalar. z is linked to the equivalence ratio by:

$$\phi = \frac{z}{1-z}\frac{1-z_{st}}{z_{st}} \tag{3.29}$$

Assuming infinitely fast one step irreversible chemistry, Burke-Schumann proposed a solution to Eq. (3.27) in the mixture fraction space. There exists an infinitely thin non-equilibrium layer at $z = z_{st}$ and outside this layer, the mass fractions of fuel and oxidizer are either zero or piecewise linear function of z. Taking into account finite rate reversible chemistry, the Burke-Schumann structure is altered and fuel and oxidizer can coexist in the reaction zone, which thickness depends on the scalar dissipation rate χ. Once the solution of the mixing problem is known (Eq. (3.27)), χ can be evaluated and the flame structure can be determined in the mixture fraction space.

3.2.3 Triple flame propagation

After ignition in a partially premixed environment, the flame structure is that of a triple flame (Dold, 1989; Kioni *et al.*, 1993; Chakraborty & Mastorakos, 2008; Neophytou *et al.*, 2010). Triple flames are crucial for partially premixed configurations since they play a role in the flame stabilization mechanisms (Veynante *et al.*, 1994) or auto-ignition processes (Domingo & Vervisch,

1996). As sketched in Fig. 3.5, triple flames feature both premixed and non-premixed flame fronts: the premixed flame front spans from fuel-rich to fuel-lean mixtures. This premixed flame front has a leading edge (called triple point) in the stoichiometric mixture region that exhibits a maximum burning velocity. Downstream this triple point, a diffusion flame is stabilized and fed by the excess of fuel and oxidizer from the rich and lean premixed flames respectively.

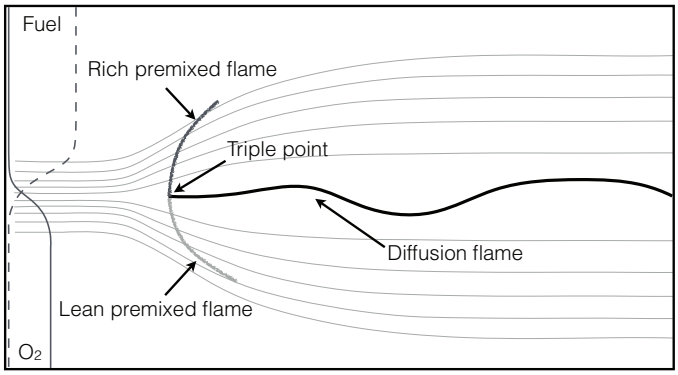

Figure 3.5: Schematic description of the triple flame structure

The propagation speed of a triple flame was found to be larger than a premixed laminar flame speed due to hydrodynamic effects associated with heat release in the premixed flame (Ruetsch *et al.*, 1995; Echekki & Chen, 1998) which redirects the flow in front of the flame (illustrated in Fig. 3.5). The propagation speed then depends on the gradient of mixture fraction: for small gradients, premixed flames are longer and the flow deflection in front of the triple point is larger than for strong gradients where the premixed flames are shorter.

3.3 Turbulent flames

3.3.1 Basics of turbulence

The transition from a laminar flow to a turbulent flow in our target application is characterized by the Reynolds number comparing inertia to viscous forces:

$$Re = \frac{|\boldsymbol{u}|l}{\nu} \tag{3.30}$$

where $\boldsymbol{u}$ and l are characteristic velocity and dimension of the flow respectively and ν is the kinematic viscosity. When inertia forces dominate (i.e. large Reynolds number), the flow is characterized by significant variations of the velocity field in space and time which presents a multitude of vortices of varying sizes, called eddies, convected by the mean flow. These eddies strongly interact with each other through a cascade process where large eddies split into smaller ones, transmitting energy from the large to the small scales. As compared to laminar flow, turbulence greatly enhances transfers of mass, momentum and heat. In a homogeneous isotropic turbulence, the spectral distribution of energy follows the typical sketch presented in Fig. 3.6

where the energy density $E(k)$ is plotted versus the eddy wave number k (inverse of the eddy length scale).

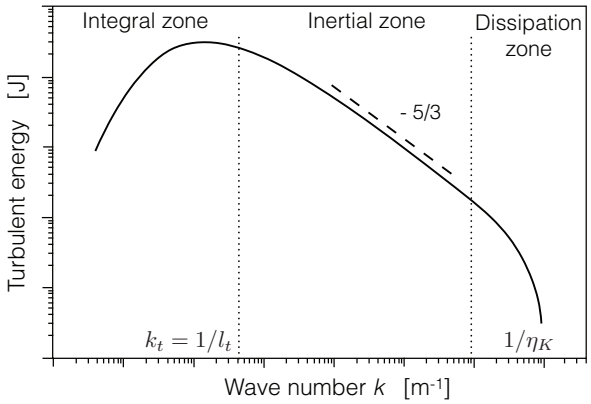

Figure 3.6: Sketch of energy density spectrum $E(k)$ in an homogeneous isotropic turbulence along with the distinction of the integral, inertial and dissipation zones (Richardson, 1922).

Following Pope (2000), three zones can be identified from the biggest to the lowest length scales:

- The **integral zone** is characterized by the lowest frequencies and is centered on the wave number k_t corresponding to the integral length scale l_t. It contains the biggest and most energetic eddies where the turbulent energy is produced and their size is of the order of the characteristic length of the geometry. The largest scales in a turbulent flow are mainly controlled by inertia and are not affected by viscous effects.

- In the **inertial zone** the large eddies become unstable and break down into smaller eddies via the 'cascade' process. No eddy dissipation is detected and the rate of energy transfer from the biggest to the smallest structures is constant following a $k^{-5/3}$ law for isotropic statistically steady turbulence (Kolmogorov, 1941).

- The **dissipation zone** is characterized by the highest wave numbers and is centered on the Kolmogorov wave number k_{η_K} corresponding to the Kolmogorov length scale η_K. At these scales, viscous forces dominate and the turbulent energy is dissipated into heat due to the kinematic viscosity ν. Kolmogorov length scale and speed can be estimated (in isotropic homogeneous turbulence) by:

$$\eta_K = \left(\frac{\nu^3}{\varepsilon}\right)^{1/4} \text{ and } u'_K = (\nu\varepsilon)^{1/4} \tag{3.31}$$

where the subscript K denotes the Kolmogorov scale and ε is the dissipation rate given by:

$$\varepsilon = 2\nu S_{ij} S_{ij} \tag{3.32}$$

3.3.2 Turbulent premixed combustion

3.3.2.a Turbulent premixed combustion regimes

In a first approach, turbulent premixed combustion is described as the result of interactions between the flame front and the flow eddies whose sizes range from the Kolmogorov to the integral scales and with characteristic speeds ranging from the Kolmogorov velocity u'_K to the integral Root Mean Square (RMS) velocity u'. Chemistry can be characterized by a chemical time scale:

$$\tau_c = \frac{\delta_L^0}{S_L^0} \tag{3.33}$$

where δ_L^0 and S_L^0 are respectively the thermal thickness and flame speed of an unstrained laminar premixed flame. This chemical time τ_c corresponds to the time required for the flame to propagate over a distance equal to its own thickness. This flame then interacts at the same time with the most energetic turbulent structures characterized by the turbulence time scale $\tau_t = l_t/u'_t$, and with the smallest turbulent scales characterized by the Kolmogorov time scale $\tau_K = \eta_K/u'_K$. Classical approaches therefore introduce two reduced numbers corresponding to the limiting values of the flow motion and sizes to describe the turbulence/flame interactions:

- The **Damköhler number** Da is defined as the ratio of the integral time scale τ_t to the chemical time scale τ_c:

$$Da = \frac{\tau_t}{\tau_c} = \frac{l_t}{\delta_L^0}\frac{S_L^0}{u'_t} \tag{3.34}$$

  Two cases must be distinguished:

  - for high Da number ($Da >> 1$), the turbulent time scale is much larger than the chemical time scale and the structure of the flame front is not modified by the turbulence. In this **flamelet regime** or **thin wrinkled flame regime**, the turbulent flame front can be assimilated to a collection of laminar flame elements called "flamelets".
  - for small Da number ($Da << 1$), the turbulent time scale is much smaller than chemistry and the reactants and products are mixed by turbulent motion before reacting via a slow chemical process. This corresponds to the **well stirred reactor** limit.

- The **Karlovitz number** Ka identifies the interactions between the turbulent small scales and the flame:

$$Ka = \frac{\tau_c}{\tau_K} = \frac{\delta_L^0}{\eta_K}\frac{u'_K}{S_L^0} \tag{3.35}$$

  Various expressions of the Karlovitz number can be found in the literature. Using the relation $S_L^0 \sim \nu/\delta_L^0$, a unity flame Reynolds number is obtained:

$$Re_{fl} = \frac{\delta_L^0 S_L^0}{\nu} = 1 \tag{3.36}$$

yielding:

$$Ka = \left(\frac{u'}{S_L^0}\right)^{3/2} \left(\frac{l_t}{\delta_L^0}\right)^{-1/2} = \left(\frac{\delta_L^0}{\eta_K}\right)^2 \tag{3.37}$$

using Eq. (3.31), showing that the Karlovitz number compares the laminar flame length scale to the smallest turbulent scale.

Since the Reynolds, Damköhler and Karlovitz numbers are related through $Re = Da^2 Ka^2$, the transition between the different combustion regimes can be completely defined using only two non-dimensional numbers. Following Peters (2000), a diagram of the various combustion regimes is presented in Fig. 3.7 as a function of length l_t/δ_L^0 and velocity u'/S_L^0 ratios, giving a qualitative distinction between the combustion regimes based on the Karlovitz, Damköhler and the flame Reynold numbers.

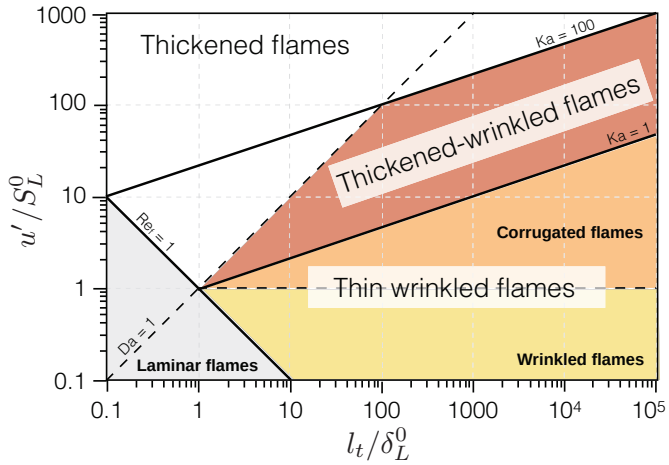

Figure 3.7: Combustion regime diagram for premixed turbulent combustion from Peters (2000).

3.3.2.b Turbulent flame propagation and quenching

In the flamelet regime, the turbulent flame can be viewed as a collection of laminar premixed flame elements distributed along a stretched and wrinkled front (see Fig. 3.8). As a consequence of the wrinkling, the turbulent flame area A_T is increased enhancing diffusion and reaction, hence increasing the propagation speed. The turbulent flame brush is propagating at a turbulent velocity S_T equal to the laminar flame speed weighted by the ratio of the wrinkled instantaneous flame front area A_T to the unwrinkled area A_L (Driscoll, 2008):

$$\frac{S_T}{S_L^0} = \frac{A_T}{A_L}\frac{\overline{S}_c}{S_L^0} \tag{3.38}$$

where the term $\overline{S}_c/S_L^0$ is the stretch factor that accounts for the effect of stretch on the flamelet velocity (Bray & Cant, 1991) using the turbulent flame brush mean consumption velocity $\overline{S}_c$.

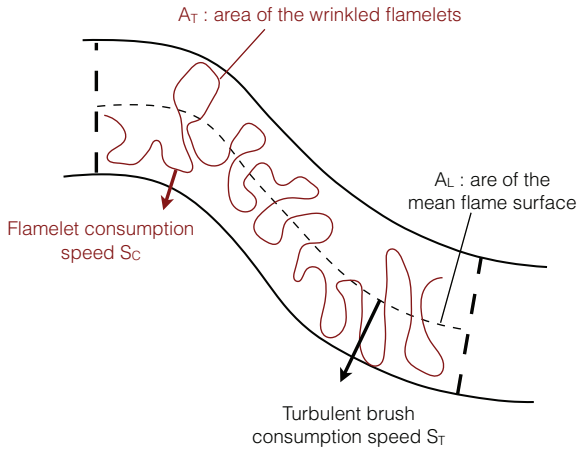

Figure 3.8: Sketch of the wrinkled area A_T and the mean flame surface A_L. Extracted from Driscoll (2008).

The turbulent velocity S_T increases with increasing turbulent intensity. Several relations linking the turbulent velocity fluctuations u' to the turbulent flame speed have been established, such as the simplest one proposed by Abdel-Gayed *et al.* (1984):

$$\frac{S_T}{S_L^0} \simeq 1 + \frac{u'}{S_L^0} \tag{3.39}$$

Relations such as Eq. (3.39) have been built from both experimental and theoretical studies, but with large disparities proving the difficulty of deriving a universal expression. Nonetheless, it is generally agreed that for high level of turbulence, S_T reaches a plateau followed by flame quenching if the turbulence intensity is further increased. Quenching in a turbulent flame front is the consequence of sufficiently strong aerodynamic stretch that can locally reduce or even completely suppress the combustion process. This point has been discussed in Sec. 3.2.1.b for laminar flame submitted to steady stretch. In turbulent flames, stretch is intrinsically time-dependent and results from the interaction with the full range of vortices. In the flamelet regime, the results of laminar studies using DNS (Poinsot *et al.*, 1991) and experiments (Roberts *et al.*, 1993) should be valid in turbulent flames. These studies investigate the canonical case of laminar flame/vortex interactions varying the vortex size and strength. The interaction is found to mainly depend on three parameters (Poinsot & Veynante, 2011): the vortex velocity to flame speed ratio, the Karlovitz number evaluated at the vortex size and the vortex power. The interaction of individual vortices with the flame can then be classified in a spectral diagram as reported in Fig. 3.9 following Poinsot *et al.* (1991).

Vortices in the "no effect zone" are either too slow to counteract the flame speed ($u'(r)/S_L^0 < 1$) or too weak ($(r/\delta_L^0)^2 < 1$) to penetrate the flame front and have no significant effect on the flame front. As the vortex size and strength increases, the flame is first wrinkled, then pockets of fresh gases are created and finally quenching of the flame front is observed past the quench limit. In Fig. 3.9, a Homogeneous Isotropic Turbulence (HIT) spectrum can be represented by a line following $u'(r)^3/r = \varepsilon$. Depending on whether this line crosses the quenching region or not,

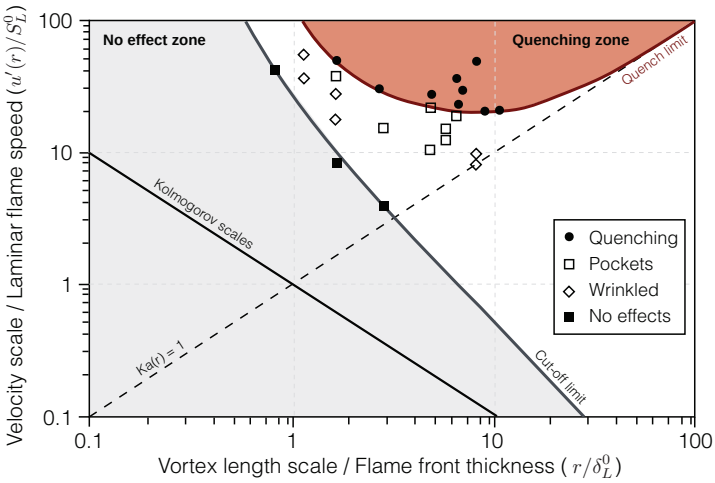

Figure 3.9: Spectral diagram obtained from DNS of laminar flame/vortex interaction. Extracted from Poinsot *et al.* (1991).

the flamelet regime or the thickened-wrinkled flame regime better characterize the combustion regime encountered in this flow (see Fig. 3.7).

3.3.3 Non-premixed combustion regimes

Similarly to the premixed combustion, non-premixed combustion regimes have to be identified in order to study the interaction of diffusion flames with turbulence and support the development of models. However, since diffusion flames do not exhibit well-defined characteristic scales this task is more difficult. Figure 3.10(left) illustrates a comparison between the laminar flame length scale introduced in Sec. 3.2.2 and the turbulence length scales.

As a first step towards the construction of a non-premixed turbulent combustion diagram, Cuenot & Poinsot (1994) investigated the ability of turbulent vortices to modify the laminar diffusion flame in a flame/vortex case where the flame characteristic scales can be defined unambiguously. Even though a combustion diagram cannot directly be derived from this study, it shows that the diffusion flame structure is controlled by Da^{fl} and that a simple classification can be proposed based on the transition flame Damköhler numbers Da^{LFA} and Da^{ext} where LFA stands for Laminar Flamelet Assumption and the superscript ext denote an extinction zone:

- For $Da^{fl} > Da^{LFA}$, the diffusion flame keeps its laminar flame structure.
- For $Da^{LFA} > Da^{fl} > Da^{ext}$, the flame structure is modified but the diffusion flame is not quenched because of unsteady effects: indeed the flame undergoes strain rates higher than predicted by asymptotic theories but is not quenched because of the short duration of the flame/vortex interaction.
- For $Da^{ext} > Da^{fl}$, the laminar diffusion flame is quenched because the strain rate is too strong.

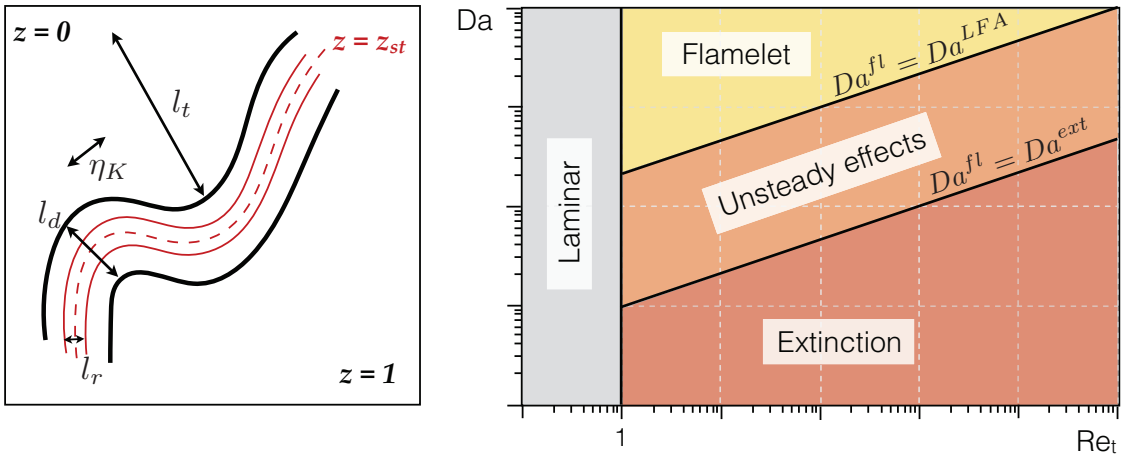

Figure 3.10: Definition of diffusion flame thickness and turbulence length scale (left). Non-premixed combustion diagram as function of the turbulent Reynolds number Re_t and Damköhler number Da (Cuenot & Poinsot, 1994) (right).

The non-premixed diagram derived from the identification of these transitions is presented in Fig. 3.10(right) as function of the turbulent Reynolds number Re_t and the Damköhler number $Da \simeq 2\sqrt{Re_t} Da^{fl}$ (Cuenot & Poinsot, 1994).

Chapter 4

Modeling of turbulent reactive flows

Contents

The numerical resolution of Eqs. 2.5-2.7 for turbulent flows in complex geometries is today still a challenge. Turbulent flows are characterized by a wide range of length scales. Indeed between the most energetic integral length scale l_t and the dissipative Kolmogorov length scale η_K, several orders of magnitude can be found, depending on the flow Reynolds number as (Kolmogorov, 1941):

$$\frac{l_t}{\eta_K} = Re^{3/4} \tag{4.1}$$

This ratio gives the discretization required in each direction to explicitly compute all the scales of the flow. Considering a three dimensional computation, the number of grid points N_{pt} scales as:

$$N_{pt} = \left(Re^{3/4}\right)^3 = Re^{9/4} \tag{4.2}$$

The Reynolds number in aeronautical combustor can go up to $Re = 1.10^6$, leading to numerical grid containing $N_{pt} = 3.10^{13}$, which is still out of reach with current computational ressources. Taking into account the chemical reactions further stiffen the problem since realistic combustion chemistry involves hundreds of species through thousands of reactions, and the characteristic chemical time scales spread over a very wide range.

4.1 Computationnal approaches

Three CFD methodologies have emerged to solve the compressible reactive Navier-Stokes set of equations and can be sorted based on the modeling effort required:

- Reynolds Averaged Navier-Stokes (RANS) computations do not solve for the instantaneous flow field but only the time-averaged values of all NS quantities. The governing RANS equations are obtained by (Reynolds or Favre) averaging the instantaneous equations (Eqs. 2.5-2.7), exhibiting unclosed terms for which models have been developed. These models represent the effect of the entire turbulence spectrum on the mean flow field. However, the largest scales of the turbulent motion strongly depending on the simulated configuration, the RANS closure models often lack universality. RANS computations have historically been the first possible approach thanks to their affordable computational cost.

- LES introduces a scale separation between the turbulent large scales and the smaller ones. The former are supposed to greatly depend on the geometry and are explicitly calculated while the latter are modeled. Modeling of the small scale is expected to be easier than RANS closure models since the small scale turbulence have a self-similar universal nature (at least far from boundary layers). The balance equations for LES are obtained by filtering the instantaneous balance equations as summarized in Sec. 4.2. Compared to RANS, LES main advantage is its intrinsic capability to capture unsteady features. LES has experienced a fast development over the last 20 years and appears to be an excellent candidate to investigate unsteady phenomena in complex configurations, in particular the ignition process studied in this work.

- DNS consists in explicitly resolving the full instantaneous Navier-Stokes equations from the largest to the smallest turbulent scales. In that sense, DNS is the opposite approach to RANS and is associated with very high computational costs. For a long time, DNS of realistic configurations has been prevented by the high numerical cost of the simulation. If DNS of full realistic configurations are not yet affordable, academic configurations (moderate Reynolds number) are now investigated by using High Performance Computing (HPC) (Chen *et al.*, 2009; Moureau *et al.*, 2011*b*). Nonetheless, DNS has changed the analysis of turbulent combustion and has been used to bring some fundamental understanding of the physical phenomena and build models for LES and RANS.

These three approaches are illustrated in Fig. 4.1 in the turbulent energy spectrum where the wave numbers of both the integral length scale l_t and the Kolmogorov length scale η_K are mentioned. By construction, LES tend towards DNS when the cut-off length scale goes to η_K.

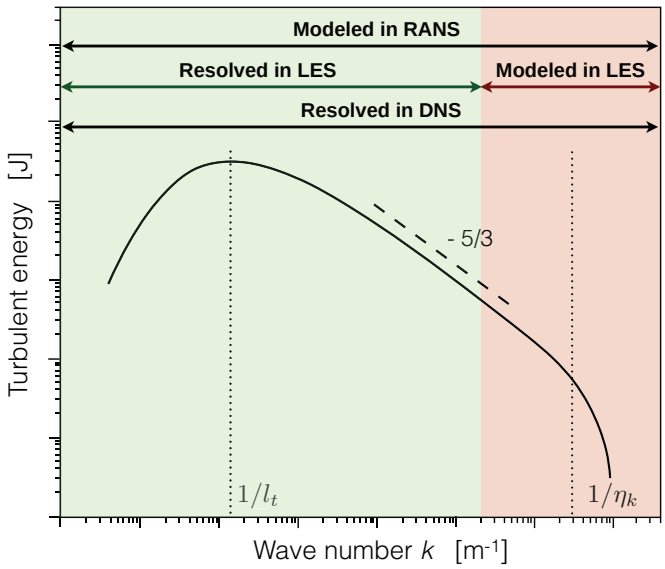

Figure 4.1: Turbulence energy spectrum plotted as function of the wave number k. RANS, LES and DNS are depicted in terms of spatial ranges explicitly resolved and modeled for each computational approach.

4.2 LES modeling

LES filtered quantities are obtained by the convolution product of any scalar quantity with a filter $\mathcal{G}_\Delta$:

$$\overline{f}(\mathbf{x},t) = \int f(\mathbf{x},t)\mathcal{G}_\Delta(\mathbf{x}-\mathbf{x}')\,dx \tag{4.3}$$

Two classes of LES can be distinguished depending on whether the filtering operation is applied explicitly to the conservation equations, which are subsequently resolved numerically (referred as "explicit LES") or results from the discretization on an under-resolved grid size (referred as "implicit LES"). In this work, only implicit LES will be used.

The unresolved or subgrid scale (SGS) contribution is defined by:

$$f'(\mathbf{x},t) = f(\mathbf{x},t) - \overline{f}(\mathbf{x},t) \tag{4.4}$$

Using the above definition, a source term appears in the filtered mass conservation equation corresponding to the correlation between density and velocity fluctuations (Poinsot & Veynante, 2011) and is uneasy to handle in CFD codes. Generally, a Favre averaged definition is preferred to avoid this issue:

$$\widetilde{f} = \frac{\overline{\rho f}}{\overline{\rho}} \tag{4.5}$$

4.2.1 Filtered governing equations

Applying the filtering operation to Eqs. 2.5-2.7 yields:

$$\frac{\partial \overline{\rho}}{\partial t} + \frac{\partial \overline{\rho}\widetilde{u}_i}{\partial x_i} = 0 \tag{4.6}$$

$$\frac{\partial \overline{\rho}\widetilde{u}_j}{\partial t} + \frac{\partial \overline{\rho}\widetilde{u}_i\widetilde{u}_j}{\partial x_i} + \frac{\partial \overline{P\delta_{ij}}}{\partial x_i} = \frac{\partial}{\partial x_i}\left[\overline{\tau}_{ij} - \overline{\rho}(\widetilde{u_i u_j} - \widetilde{u}_i\widetilde{u}_j)\right] \quad \text{for} \quad j = 1,3 \tag{4.7}$$

$$\frac{\partial \overline{\rho}\widetilde{Y}_k}{\partial t} + \frac{\partial \overline{\rho}\widetilde{u}_i\widetilde{Y}_k}{\partial x_i} = \frac{\partial}{\partial x_i}\left[\overline{J}_{i,k} - \overline{\rho}(\widetilde{u_i Y_k} - \widetilde{u}_i\widetilde{Y}_k)\right] + \overline{\dot{\omega}}_k \quad \text{for} \quad k = 1,N \tag{4.8}$$

$$\frac{\partial \overline{\rho}\widetilde{E}}{\partial t} + \frac{\partial \overline{\rho}\widetilde{u}_i\widetilde{E}}{\partial x_i} + \frac{\overline{\partial u_i P\delta_{ij}}}{\partial x_i} = \frac{\partial}{\partial x_i}\left[\overline{q_i} - \overline{\rho}(\widetilde{u_i E} - \widetilde{u}_i\widetilde{E})\right] + \overline{\tau_{ij}\frac{\partial u_i}{\partial x_j}} + \overline{\dot{\omega}}_T + \dot{\mathcal{Q}}_{sp} \tag{4.9}$$

In Eqs. 4.6-4.9, the Left Hand Side (LHS) contains the filtered inviscid fluxes while viscous and turbulent (or SGS) fluxes as well as source terms are in the RHS.

4.2.2 Filtered viscous fluxes

The filtered viscous fluxes appearing in the LES governing equations are given by:

- **Laminar filtered stress tensor** $\overline{\tau_{ij}}$:

$$\overline{\tau_{ij}} = \overline{2\mu\left(S_{ij} - \frac{1}{3}\delta_{ij}S_{kk}\right)} \tag{4.10}$$

$$\text{approximation: } \overline{\tau_{ij}} \simeq 2\overline{\mu}\left(\widetilde{S}_{ij} - \frac{1}{3}\delta_{ij}\widetilde{S}_{kk}\right) \tag{4.11}$$

$$\text{with: } \widetilde{S}_{ij} = \frac{1}{2}\left(\frac{\partial \widetilde{u}_j}{\partial x_i} + \frac{\partial \widetilde{u}_i}{\partial x_j}\right) \tag{4.12}$$

$$\text{and: } \overline{\mu} \simeq \mu(\widetilde{T}) \tag{4.13}$$

- **Diffusive species flux vector** $\overline{J}_{i,k}$:

$$\overline{J}_{i,k} = \overline{-\rho\left(D_k\frac{W_k}{\overline{W}}\frac{\partial X_k}{\partial x_i} - Y_k V_i^c\right)} \tag{4.14}$$

$$\text{approximation: } \overline{J}_{i,k} \simeq -\overline{\rho}\left(\overline{D}_k\frac{W_k}{\overline{W}}\frac{\partial \widetilde{X}_k}{\partial x_i} - \widetilde{Y}_k\widetilde{V}_i^c\right) \tag{4.15}$$

$$\text{with: } \widetilde{V}_i^c = \sum_{k=1}^{N}\overline{D}_k\frac{\partial \widetilde{X}_k}{\partial x_i} \tag{4.16}$$

$$\text{and: } \overline{D}_k \simeq \frac{\overline{\mu}}{\overline{\rho}Sc_k} \tag{4.17}$$

- **Filtered heat flux** $\overline{q}_i$:

$$\overline{q_i} = \overline{\lambda \frac{\partial T}{\partial x_i}} - \overline{\rho \sum_{k=1}^{N} V_{k,i} Y_k h_{s,k}} \tag{4.18}$$

$$\text{approximation: } \overline{q_i} \simeq \overline{\lambda} \frac{\partial \widetilde{T}}{\partial x_i} - \sum_{k=1}^{N} \overline{J}_{i,k} \widetilde{h}_{s,k} \tag{4.19}$$

$$\text{with: } \overline{\lambda} \simeq \frac{\overline{\mu}\,\overline{C_p}(\widetilde{T})}{Pr} \tag{4.20}$$

The species and thermal diffusion fluxes have been approximated using a simple gradient assumption.

4.2.3 Subgrid fluxes closure

The unresolved scales effect on the filtered quantities appearing in Eqs. 4.6-4.9 must be modeled. SGS closures are given by:

- **Unresolved Reynolds tensor** $\overline{\tau}_{ij}^{sgs} = -\overline{\rho}(\widetilde{u_i u_j} - \widetilde{u}_i \widetilde{u}_j)$:

$$\overline{\tau}_{ij}^{sgs} = 2\overline{\rho}\nu_t \left(\widetilde{S}_{ij} - \frac{1}{3}\delta_{ij} \widetilde{S}_{kk} \right) \tag{4.21}$$

  where ν_t is the SGS kinematic viscosity for which various expressions have been established (detailed in Sec. 4.2.4).

- **Unresolved species fluxes** $\overline{J}_{i,k}^{sgs} = -\overline{\rho}(\widetilde{u_i Y_k} - \widetilde{u}_i \widetilde{Y}_k)$:

$$\overline{J}_{i,k}^{sgs} = -\overline{\rho} \left(D_k^t \frac{W_k}{\overline{W}} \frac{\partial \widetilde{X}_k}{\partial x_i} - \widetilde{Y}_k \widetilde{V}_i^{c,t} \right) \tag{4.22}$$

$$\text{with: } \widetilde{V}_i^{c,t} = \sum_{k=1}^{N} \overline{D}_k^t \frac{\partial \widetilde{X}_k}{\partial x_i} \tag{4.23}$$

$$\text{and: } D_k^t = \frac{\mu_t}{\rho S c_k^t} \tag{4.24}$$

  where Sc_k^t is the turbulent Schmidt number of species k, equal for all species $Sc_k^t = Sc^t = 0.6$. Note that having one turbulent Schmidt number for all the species does not imply $\widetilde{V}_i^{c,t} = 0$ because of the ratio $W_k/\overline{W}$ in Eq. (4.22).

- **Unresolved energy flux** $\overline{q}_i^{sgs} = -\overline{\rho}(\widetilde{u_i E} - \widetilde{u}_i \widetilde{E})$:

$$\overline{q}_i^{sgs} = -\lambda_t \frac{\partial \widetilde{T}}{\partial x_i} + \sum_{k=1}^{N} \overline{J}_{i,k} \widetilde{h}_{s,k} \tag{4.25}$$

$$\text{with: } \lambda_t = \frac{\mu_t \overline{C}_p}{Pr^t} \tag{4.26}$$

4.2.4 Modeling of the subgrid stress tensor

LES models for the subgrid stress tensor (see Eq. (4.21)) are derived on the theoretical ground that the LES filter is spatially and temporally invariant. Generally, the influence of the SGS on the resolved motion is taken into account by a SGS model based on the introduction of a turbulent kinematic viscosity, ν_t (Boussinesq (1877) hypothesis). Such an approach assumes that the effect of the SGS field on the resolved field is purely dissipative. This assumption is essentially valid within the cascade theory introduced by Kolmogorov (1941). LES models for the subgrid stress tensor only differ through the estimation of ν_t. In this document, only the three models used during the thesis are presented: the Smagorinsky, the WALE (Wall Adapting Local Eddy-viscosity) and the SIGMA model. More information on the other models implemented in AVBP can be found for example in (AVBP, 2011).

- **The Smagorinsky model**

$$\nu_t = (C_s \Delta_x)^2 \sqrt{2 \widetilde{S}_{ij} \widetilde{S}_{ij}} \tag{4.27}$$

  where Δ_x is the filter characteristic length (cube-root of the cell volume), C_s is the model constant equal to 0.18 but can vary between 0.1 and 0.8 depending on the flow configuration. The Smagorinsky model (Smagorinsky, 1963) was developed in the sixties and heavily tested for multiple flow configurations. This closure has the particularity of supplying the right amount of dissipation of kinetic energy in homogeneous isotropic turbulent flows. Locality is however lost and only global quantities are maintained. It is known to be too dissipative and transitioning flows are not suited for its use (Sagaut, 2002). Moreover, this formulation is known for not vanishing in near-wall regions and therefore cannot be used when walls are treated as no-slip walls.

- **The WALE model**

$$\nu_t = (C_w \Delta_x)^2 \frac{(s^d_{ij} s^d_{ij})^{3/2}}{(\widetilde{S}_{ij} \widetilde{S}_{ij})^{5/2} + (s^d_{ij} s^d_{ij})^{5/4}} \tag{4.28}$$

  with

$$s^d_{ij} = \frac{1}{2}(\widetilde{g}^2_{ij} + \widetilde{g}^2_{ij}) - \frac{1}{3}\widetilde{g}^2_{kk}\delta_{ij} \tag{4.29}$$

  where $C_w = 0.4929$ is the model constant and $\widetilde{g}_{ij}$ is the resolved velocity gradient. The WALE mode was developed by Nicoud & Ducros (1999) for wall bounded flow in an attempt to recover the scaling of the laws-of-the-wall. Similarly to the Smagorinsky model locality is lost and only global quantities are to be trusted.

- **The SIGMA model**

$$\nu_t = (C_\sigma \Delta_x)^2 \frac{\sigma_3(\sigma_1 - \sigma_2)(\sigma_2 - \sigma_3)}{\sigma_1^2} \tag{4.30}$$

  where $C_\sigma = 1.35$ is the model constant. The SIGMA operator was proposed by Nicoud *et al.* (2011) based on singular values (σ_1, σ_2 and σ_3) of a tensor built using resolved velocity

gradients. Note that the singular values σ_i have the following near-wall behaviors:

$$\begin{cases} \sigma_1 = O(1) \\ \sigma_2 = O(y) \\ \sigma_3 = O(y^2) \end{cases} \tag{4.31}$$

where y is the normal coordinate to the wall surface and $O(y^p)$ denotes a term of the order of p, i.e. behaving like y^p when the distance to the solid boundary decreases: $y \mapsto 0$. Thus, the SIGMA model behaves correctly in the near-walls region: $\nu_t = O(y^3)$.

4.3 Combustion modeling

4.3.1 Overview

The region where chemical reactions take place, referred to as the flame front, is generally very small. Typical flame thickness at atmospheric pressure for kerosene/air flames is about 0.1 to 0.5 mm raising a problem for LES of reactive flows: the flame thickness δ_L^0 is generally smaller than the standard LES grid size Δ_x. Depending on the complexity of the chemical description and the operating conditions, 5 to 50 points are needed to correctly resolve the flame front. The resulting mesh size is out of reach with current computational resources considering the complexity of industrial configurations. In LES, combustion models have been developed to approximate the filtered species reaction rates $\overline{\dot{\omega}}_k$ (see Eq. (4.8)) from the resolved quantities. Reviews proposed by Veynante & Vervisch (2002), Pitsch (2006) or the textbook of Poinsot & Veynante (2011) give an overview of the combustion models. Combustion modeling is generally split between models for premixed and non-premixed regimes.

For turbulent premixed combustion, two main categories are distinguished:

- **Models assuming an infinitely thin reaction zone:** the turbulent premixed flame is modeled by fresh reactants and burnt products separated by an infinitely thin reaction zone. The local structure of the flame is assumed equal to a laminar flame for which the inner structure is not affected by turbulence (flamelet assumption). The Bray-Moss-Libby (BML) models (Bray & Moss, 1977), the flame surface density models (Hawkes & Cant, 2000), and the G-equation model (Moureau *et al.*, 2009) are some of the most popular models in this category.
- **Models describing the structure of the reaction zone thickness:** the turbulent premixed flame is characterized by a finite thin reaction zone that can interact with the turbulent flow and often behaves as a stretched laminar flame. Some examples are the Probability Density Function (PDF) models (Dopazo, 1994), the F-TACLES approach (Fiorina *et al.*, 2010) and the artificially Thickened Flame (TF) models (Colin *et al.*, 2000; Légier *et al.*, 2000).

In non-premixed systems, combustion is generally controlled by the rate of molecular mixing because chemistry is faster than turbulent motion. The mixing is then evaluated with a conserved

scalar, typically the mixture fraction z which is essentially a measure of the local equivalence ratio. Several methods have been proposed to measure the mixing rate in turbulent flows:

- **Probability Density Function (PDF) methods:** the Reynolds averaged values are obtained from the PDF of mixture fraction. Under the assumption of an infinitely fast chemistry, the local filtered reaction rate may be expressed as:

$$\overline{\dot{\omega}}_k(x,t) = \int_0^1 \dot{\omega}_k(z) P(z,x,t) dz \tag{4.32}$$

  where $P(z,x,t)$ is the subgrid scale mixture fraction PDF and $\dot{\omega}_k(z)$ is the non-filtered reaction rate obtained from a flamelet library. A popular method is to presume the shape of the PDF: Cook & Riley (1994) proposed to use β-function using the mean mixture fraction $\widetilde{z}$ and its variance $\widetilde{z''^2}$. A conservation equation for $\widetilde{z}$ is typically added to the NS set of equations while $\widetilde{z''^2}$ is obtained either from an algebraic closure or a balance equation. The PDF can also be explicitly computed from a balance equation (Pope, 1985). Similar approaches have been derived to encompass finite rate chemistry through the scalar dissipation rate χ (Cook & Riley, 1998), for which the PDF must be evaluated and the flamelet library extended to $\dot{\omega}_k(z,\chi)$.

- **Linear Eddy Model (LEM) methods:** they were proposed by Kerstein (1988) for which a turbulent stirring at the subgrid scale level is applied on a 1D scalar field and a 1D reaction-diffusion equation is integrated in each LES cell to represent unresolved mixing and chemical reactions.

Regardless of the combustion regimes, the artificially thickened flame model is considered in this work. Poinsot & Veynante (2011) recalled that the use of TFLES for non-premixed flame is not correct from a theoretical point of view, but the model has shown reasonably good results in several non-premixed configurations, mainly because the combustion regime in realistic gas turbine is generally partially premixed rather than purely non-premixed. Section 4.3.2 details the TFLES model.

4.3.2 Thickened Flame LES (TFLES) model

An attractive solution to explicitly resolve the flame front on the LES grid consists in artificially thickening the flame. This idea was first proposed by Butler & O'Rourke (1977). Since the reaction rate is still expressed using Arrhenius law, various phenomena can be accounted for without requiring ad-hoc sub models (ignition, flame/wall interactions, heat losess, ...). The whole TFLES method is based on a simple change of the spatial and temporal variables:

$$x \mapsto \mathcal{F}x \quad \text{and} \quad t \mapsto \mathcal{F}t \tag{4.33}$$

which corresponds to a thickening of the flame thickness by a factor $\mathcal{F}$. The thickened species reaction rates are then:

$$\overline{\dot{\omega}}_k^* = \frac{\dot{\omega}_k}{\mathcal{F}} \tag{4.34}$$

Following the theories of laminar premixed flame (Williams, 1985), the laminar flame speed S_L^0 then writes:

$$S_L^0 \propto \frac{D_{th}}{\delta_L^0} \mapsto \frac{D_{th}}{\mathcal{F}\delta_L^0} \tag{4.35}$$

In order to conserve the flame speed through the change of variables, the thermal and species diffusivities need to be multiplied by the same thickening factor $\mathcal{F}$ so that:

$$S_L^0 \propto \frac{\mathcal{F}D_{th}}{\mathcal{F}\delta_L^0} = \frac{D_{th}}{\delta_L^0} \tag{4.36}$$

When the flame is thickened by a factor $\mathcal{F}$, the interaction between the flame and the turbulence is modified: the flame becomes less sensitive to turbulent motions and vortices may affect the reaction zone. This interaction is characterized by the Damköhler number Da (see Eq. (3.34)):

$$Da = \frac{\tau_t}{\tau_c} = \frac{l_t}{u'}\frac{S_L^0}{\delta_L^0} \mapsto \frac{l_t}{u'}\frac{S_L^0}{\mathcal{F}\delta_L^0} = \frac{\tau_t}{\mathcal{F}\tau_c} \tag{4.37}$$

This point has been investigated using DNS by Angelberger *et al.* (1998) and Colin *et al.* (2000). The so-called efficiency function $\mathcal{E}$ has been proposed to properly account for the unresolved wrinkling effect (filtered at the thickened flame size $\Delta_e \sim \mathcal{F}\Delta_x$ where the subscript e stands for effective) on the filtered reaction rate:

$$D_{th} \mapsto \mathcal{E}\mathcal{F}D_{th} \quad \text{and} \quad D_k \mapsto \mathcal{E}\mathcal{F}D_k \tag{4.38}$$

$$\overline{\dot{\omega}}_k = \frac{\mathcal{E}\dot{\omega}_k}{\mathcal{F}} \tag{4.39}$$

so that:

$$S_L^0 \mapsto \frac{\mathcal{E}\mathcal{F}D_{th}}{\mathcal{F}\delta_L^0} = S_T \tag{4.40}$$

where S_T is the resolved turbulent flame speed.

In this work, two different efficiency functions $\mathcal{E}$ are employed. Both are based on the hypothesis that an equilibrium is reached between the turbulent motion and the flame surface at the subgrid scale level (i.e. the aerodynamic stretch and the stretch induced by the curvature of the flame front compensate each other so that there is no creation or destruction of flame surface at the subgrid scale level).

- In the **Colin model**, Colin *et al.* (2000) proposed an efficiency function $\mathcal{E}_{Colin}$ which compares the flame wrinkling with and without thickening, using the wrinkling factor Ξ:

$$\Xi(\delta_L^0) = 1 + \alpha\Gamma_{Co}\left(\frac{\Delta_e}{\delta_L^0}, \frac{u'_{\Delta_e}}{S_L^0}\right)\frac{u'_{\Delta_e}}{S_L^0} \tag{4.41}$$

  where α is a constant and Γ_{Co} is a function taking into account the subgrid strain rate depending on the effective filter size Δ_e and the fluctuating subgrid velocity u'_{Δ_e}. Note that

α requires an estimation of the integral length scale l_t, which is often unknown and varies in space and time. The efficiency function is then given by:

$$\mathcal{E}_{Colin} = \frac{\Xi(\delta_L^0)}{\Xi(\mathcal{F}\delta_L^0)} \tag{4.42}$$

Finally, this combustion model is closed by approximating the subgrid scale turbulent velocity u'_{Δ_e} with an operator based on the rotational of the velocity field to remove the dilatation part of the velocity and by estimating the constant α using HIT simulations (Angelberger *et al.*, 1998).

- In the **Charlette model**, Charlette *et al.* (2002) proposed a power-law model for the wrinkling factor which extends the Colin model:

$$\Xi(\delta_L^0) = \left(1 + \min\left[\frac{\delta_{\Delta_e}}{\delta_L^0}, \Gamma_{Ch}\left(\frac{\delta_{\Delta_e}}{\delta_L^0}, \frac{u'_{\Delta_e}}{S_L^0}, Re_{\Delta_e}\right)\frac{\delta_{\Delta_e}}{\delta_L^0}\right]\right)^{\beta} \tag{4.43}$$

where β is the model parameter to be specified and Re_{Δ_e} is the turbulent Reynolds at the effective filter size: $Re_{\Delta_e} = S_L^0\delta_L^0/\nu$.

In order to tackle non-premixed configuration where fuel and oxidizer can partially mix before burning, the TFLES model has been modified to avoid acceleration of the mixing process in the non-reacting zones. A dynamic thickening method (called DTFLES) depending on the flame position and the local resolution has been developed by Légier *et al.* (2000) and is therefore preferred. This method is called DTFLES, where the word dynamic refers to local application of the TFLES model and not a dynamic procedure to evaluate the model constant as recently done in Wang *et al.* (2011). The thickening factor $\mathcal{F}$ is not constant anymore but goes from unity in non-reacting zones to $\mathcal{F}_{max}$ in the flame. This is obtained by writing:

$$\mathcal{F} = 1 + (\mathcal{F}_{max} - 1)\mathcal{S} \tag{4.44}$$

where $\mathcal{S}$ is a sensor depending on the local reaction rate and $\mathcal{F}_{max}$ is given by:

$$\mathcal{F}_{max} = \frac{N_e}{\Delta_x}\delta_L^0 \tag{4.45}$$

with N_e the number of elements used to resolve the flame front. N_e depends on the chemical scheme used, but a typical value of 5 points guarantees to recover the correct flame speed of a 1D flame for global one step or two steps schemes. The sensor $\mathcal{S}$ is computed as:

$$\mathcal{S} = \tanh\left(\beta'\frac{\Omega}{\Omega_0}\right) \tag{4.46}$$

where β' is a constant equal to 50, Ω is a sensor function detecting the presence of a reaction front and Ω_0 corresponds to its maximum value and is extracted from a laminar 1D flame computation.

4.4 Chemical scheme for LES

Directly including detailed chemical mechanisms in LES is not a viable option because of the associated high computational cost. Indeed, each species requires an additional transport equation and the stiffness of the source term of some of them requires to reduce the time step. Two approaches have been developed to overcome this problem in LES:

- Reduced schemes result in a simplification of detailed mechanisms where the chemical behavior is correctly reproduced using as few species as possible. This approach is used in this work and will be detailed below.

- Tabulated chemistry rely on the fact that the kinetic scheme variables are linked: the flame structure is studied as function of a limited number of variables (temperature, mixture fraction, ...) (Maas & Pope, 1992; Gicquel *et al.*, 2000) and all the species of the detailed kinetics are available in the LES computation through a look-up table. Two problem arise using tabulated chemistry: 1) the size of the table can rapidly increase when the number of parameters increase and several methods have been proposed to ease its use (Veynante *et al.*, 2008; Fiorina *et al.*, 2009), 2) the choice of the prototype flame used to create the table is not obvious in complex configurations where the combustion regime is unknown.

Reduced schemes can be classified in two classes:

- Global schemes are built to reproduce macroscopic quantities such as the premixed flame speed or burnt gas state. These mechanisms are easy to build for a wide range of operating conditions and since the number of reaction is low (<= 4), their implementation in LES codes is easy. All information about intermediate species and the intricate flame structure disappears.

- Analytical mechanisms have been proposed to include more physical insight in the chemical description. The reduction of a detailed mechanism can be achieved through a two-step procedure, performing first a skeletal reduction to obtain a skeletal mechanism and then a second reduction to reduce the stiffness of the obtained mechanism. The construction of a skeletal mechanism aims at removing redundant species/reactions from the detailed mechanism using for instance Sensitivity Analysis (Tomlin *et al.*, 1992) or Directed Relation Graph Analysis (Lu & Law, 2006). The resulting skeletal scheme is generally still too large and too stiff for LES in complex geometries so that techniques such as the Computational Singular Perturbation (CSP) (Lam & Goussis, 1994) or Intrinsic Low-dimensional Manifold (ILDM) (Maas & Pope, 1992) are used to further reduce the number of species based on their lifetime.

In this work, the combustion of two hydrocarbons is studied: 1) the KIAI experimental benches studied in Chaps. 6-8 & 10 use methane, 2) the annular flame propagation in the MICCA burner studied in Chap. 11 uses propane. The chemistry description employed for both hydrocarbon is presented below.

4.4.1 Methane chemistry

Two methane mechanisms are used in this work to investigate the KIAI configurations: a global two-steps chemistry and an analytically 13 species reduced scheme. Unless specified otherwise, the simulations are performed with the global two-step mechanism due to its low computational cost but the effect of the chemical description is evaluated by comparison with the analytically reduced scheme. The performances of both schemes are compared to the GRI 3.0 detailed mechanisms.

4.4.1.a Global scheme: 2S_CH4_BFER

Most of the LES performed in this study use the 2S_CH4_BFER two-step mechanism of Franzelli *et al.* (2012) where the Pre-Exponential Adjustment (PEA) (Légier, 2001) method allows to reproduce the laminar flame speed over a wide range of equivalence ratio. This global scheme involves six species through two reactions given by:

$$CH_4 + 1.5\ O_2 \Longrightarrow CO + 2\ H_2O \tag{4.47}$$

$$CO + 0.5\ O_2 \Longleftrightarrow CO_2 \tag{4.48}$$

where the oxidation reaction (Eq. (4.47)) is irreversible and the recombination of CO into CO_2 is reversible (Eq. (4.48)). The Prandtl number is evaluated from the burnt gases transport properties $Pr = 0.7$ and the Schmidt numbers result from a constant unity Lewis number approximation for all species. The effect of this approximation is found to be low in Franzelli (2011) since the global scheme is fitted to reproduce the laminar flame speed. The mixture viscosity μ follows a power law (see Sec. 2.3) of parameter $\mu_0 = 1.84e^{-5}$ kg/m/s and $b = 0.6759$. When using a global scheme, the structure of the flame front is completely lost and only the global thermal balance between reaction and diffusion processes is reproduced to recover the flame speed.

4.4.1.b Analytical scheme: LU_13

The LU_13 mechanism (Sankaran *et al.*, 2007) is used to evaluate the effect of the chemistry description on the ignition kernel phase. It has been implemented in AVBP by Franzelli (2011), where several methane mechanisms were benchmarked in a partially premixed turbulent swirled flame and the LU was found to perform well compare to the GRI detailed mechanism. It takes into account 13 resolved species (CH_4, O_2, CO_2, CO, H_20, N_2, H_2, H, OH, O, HO_2, CH_3 and CH_2O) and 4 Quasi-Steady State (QSS) species (CH_2, CH_2S, HCO and CH_2OH) through 73 elementary reactions. The LU_13 mechanism does not use unity Lewis assumption and the species Lewis number are listed in Tab. 4.1 and the Prandtl number is equal to 0.7 (burnt gases state). The mixture viscosity μ follows a power law with the same parameter as the 2S_CH4_BFER scheme. The computational cost of LU_13 is about 1.68 times that of the 2S_CH4_BFER ones and it requires 63% more memory to store LES data.

CH_4	O_2	CO_2	CO	H_20	N_2	H_2	H	OH	O	HO_2	CH_3	CH_2O
0.967	1.0557	1.35	1.07	0.777	0.29	1.036	0.17	0.69	0.7	1.07	0.97	1.25

Table 4.1: Species Lewis numbers for the LU analytical mechanism

4.4.1.c Comparison of the two reduced schemes

Both the global and the analytically reduced schemes are able to reproduce the laminar flame speed over the whole range of flammable mixture with a fairly good agreement with experimental data (Franzelli, 2011) as shown in Fig. 4.2 where the adiabatic flame temperature and the laminar flame speed of both reduced schemes are plotted as functions of the equivalence ratio.

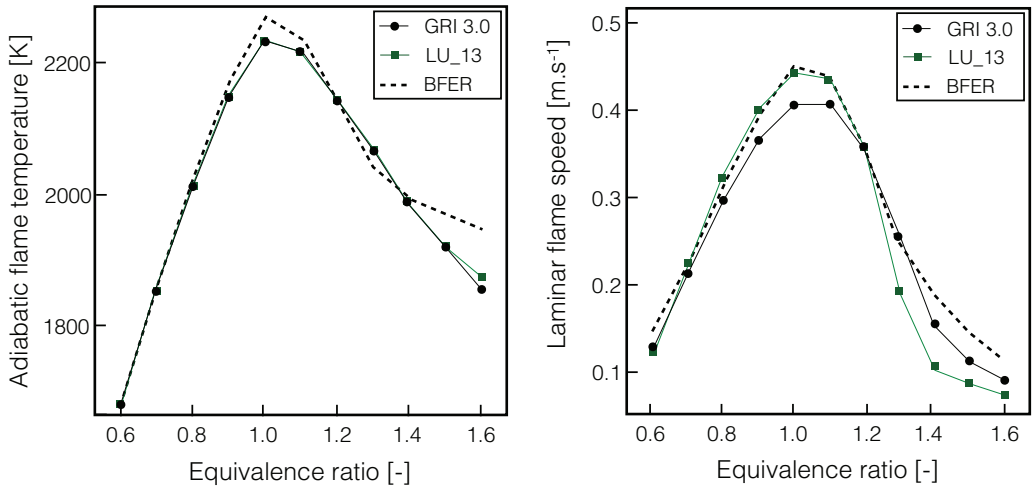

Figure 4.2: Comparison of the 2S_CH4_BFER and LU_13 schemes with GRI 3.0: adiabatic flame temperature (left) and laminar flame speed (right) (extracted from Franzelli (2011)).

When dealing with ignition, more complex flames properties should be evaluated, such as the flame response to strain and the ignition delay. To evaluate the performances of both mechanisms, the flame consumption speed is plotted against strain rate at ambient conditions in Fig. 4.3(left) and the ignition delay versus the fresh gas temperature reciprocal in Fig. 4.3(right). The results obtained with the GRI 3.0 detailed mechanism are also reported as a reference.

The LU_13 mechanism is found to recover quite well the flame response to strain for a wide range of strain rates compared to the GRI 3.0 while the 2S_CH4_BFER is less satisfactory but is able to reproduce the correct trend. Similarly, ignition delay predicted by LU_13 remains close to the GRI 3.0 mechanism (even though it can be one order of magnitude slower for low temperature) but the 2S_CH4_BFER scheme is about 100 times faster than the detailed mechanism. The effect of these differences will be evaluated in further analysis.

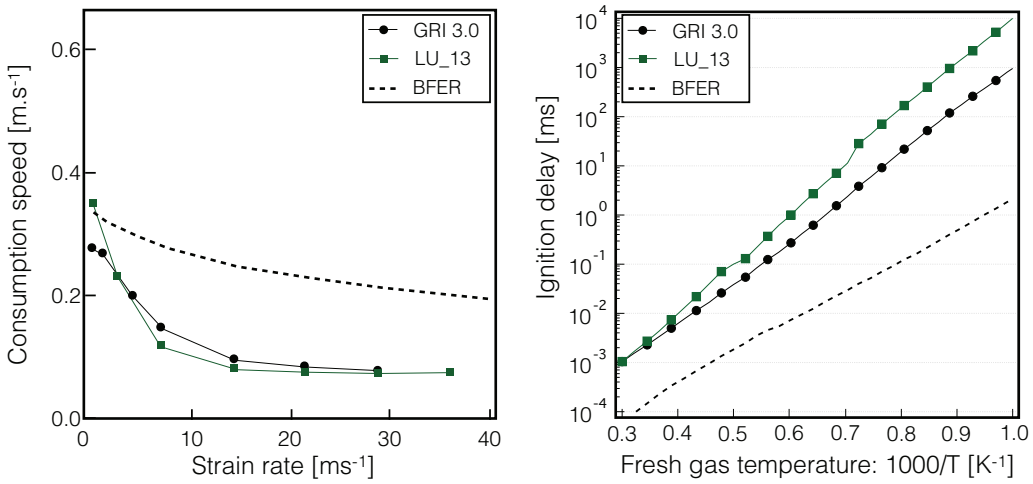

Figure 4.3: Comparison between the 2S_CH4_BFER and LU_13 schemes: consumption speed as function of strain (extracted from Franzelli (2011)) (left) and ignition delay as function of temperature reciprocal (computed with CANTERA) (right).

4.4.2 Propane chemistry

A two-step global mechanism is used to study the SIMAC configuration (Chap. 11). Since the experiment is perfectly premixed, the scheme is fitted to match the laminar flame speed at a single equivalence ratio $\phi = 0.76$. The laminar flame speed is $S_{L,0} = 0.239\ m.s^{-1}$ at this operating point. As the 2S_CH4_BFER scheme, this global scheme involves six species through two reactions given by:

$$C_3H_8 + 3.5\ O_2 \Longrightarrow 3CO + 4\ H_2O \tag{4.49}$$

$$CO + 0.5\ O_2 \Longleftrightarrow CO_2 \tag{4.50}$$

The rate of the oxidation reaction q_1 and the CO_2 recombination reaction q_2 are given by:

$$q_1 = \mathcal{A}_{f,1} \left(\frac{\rho Y_F}{W_F}\right)^{n_1^F} \left(\frac{\rho Y_{O_2}}{W_{O_2}}\right)^{n_1^{O_2}} \exp\left(\frac{E_{a,1}}{\mathcal{R}T}\right) \tag{4.51}$$

$$q_2 = \mathcal{A}_{f,2} \left[\left(\frac{\rho Y_{CO}}{W_{CO}}\right)^{n_2^{CO}} \left(\frac{\rho Y_{O_2}}{W_{O_2}}\right)^{n_2^{O_2}} - \frac{1}{K_e}\left(\frac{\rho Y_{CO_2}}{W_{CO_2}}\right)^{n_2^{CO_2}}\right] \exp\left(\frac{E_{a,2}}{\mathcal{R}T}\right) \tag{4.52}$$

where the constants are summarized in Tab. 4.2.

Once again, a constant and equal Lewis number assumption is used for all species with $Pr = 0.739$ and $Sc_k = Sc = 0.739$. The dynamic viscosity follows a power law with $\mu_0 = 2.5034e^{-5}$ kg/m/s and $b = 0.6695$.

	C_3H_8 oxidation	CO-CO_2 equilibrium
Acitivation energy	$4.15\ .10^4$	$2.0\ .10^4$
Pre-exponential factor	$2.2\ .10^{12}$	$2.5\ .10^{10}$
C_3H_8 exponent n_1^F	0.55	
O_2 exponent $n_1^{O_2}$ ($n_2^{O_2}$)	0.90	0.5
CO exponent n_2^{CO}		1.0
CO_2 exponent $n_2^{CO_2}$		1.0

Table 4.2: Activation energy $E_{a,i}$, pre-exponential factor $\mathcal{A}_{f,i}$, and reaction exponents for the C_3H_8 two-step global scheme. Units are: cal.mol^{-1} and csg.

4.5 Numerical methods in AVBP

The development of the AVBP solver started in the mid-nineties on the initiative of Schönfeld & Rudgyard (1999). The goal was to develop an efficient code handling unstructured grids of any element type in order to study complex geometries. AVBP is based on a *Cell-Vertex* finite volume formulation (Rudgyard, 1993) where the solution variables are stored at the nodes but the flux integration is computed on the cells. The cell residuals (or variations) are then distributed to the nodes in order to obtain the updated solution. From this perspective, *Cell-Vertex* schemes have a close affinity with weighted residual finite element methods (Morton & Paisley, 1989) and Colin & Rudgyard (2000) took advantage of this to implement finite element schemes in AVBP. Over the last decade, AVBP has been optimized to have a good scalability on thousands of processors on various machine architectures, allowing to have a reasonable return time even with large grid size ($\mathcal{O}^7$).

4.5.1 Numerical schemes

A complete review of the numerical schemes implemented in AVBP is presented in the Ph.D. of Lamarque (2007). The two numerical schemes used in this work are:

- The **Lax-Wendroff (LW) scheme** developed by Lax & Wendroff (1960) is a finite volume centered scheme using an explicit time integration with a single Runge-Kutta step. Its accuracy is of second order in both space and time. Its main advantage stems from the fact that its formulation includes a streamwise stabilization term making it quite robust and a mass lumping operation resulting in a low computational cost. Its use in this Ph.D. is limited to the initialization of non-reacting flows and the carburation of the combustion chambers.
- The **Two step Taylor-Galerkin 'C' (TTGC) scheme** developed by Colin & Rudgyard (2000) is a finite element scheme of the continuous Taylor-Galerkin family (Donea & Huerta, 2003). Its accuracy is of third order in both space and time (4^{th} order on regular grid (Moureau *et al.*, 2005)). Specifically built for LES, TTGC has good properties regarding dissipation and dispersion. However, these advantages make it less robust than LW and the explicit mass matrix inversion increases the computational cost (about 2.5 time

more expensive than LW). TTGC is used in this work for both non-reacting flow preceding energy deposit and complete ignition sequences.

The numerical discretization methods in AVBP are spatially centered and prone to small-scale oscillations in the vicinity of steep solution variations. This is why it is common practice to add a so-called artificial viscosity (AV) term to the discrete equations, to control these spurious modes (also known as "wiggles"). These AV models are characterized by the "linear preserving" property which leaves unmodified a linear solution on any type of element. The models are based on a combination of a "shock capturing" term (called 2^{nd} order AV) and a "background dissipation term" (called 4^{th} order AV or hyper-viscosity). In AVBP, adding AV is done in two steps:

- first a sensor detects if AV is necessary, as a function of the flow characteristics,
- then a certain amount of 2^{nd} and 4^{th} AV is applied, depending on the sensor value and on user-defined parameters.

The 2^{nd} order AV acts just like a "classical" viscosity activated only in certain regions of the flow. It smoothes local gradients, and introduces artificial dissipation. The 4^{th} order AV is mainly used to control spurious high-frequency wiggles.

4.5.2 Boundary conditions

Boundary conditions are a crucial point of CFD codes, especially for compressible flows. In the case of AVBP, it is of particular importance since the goal is to study reactive flows in combustion chambers where the geometry has a direct effect on the flow and where the acoustic behavior is controlled by inlet and outlet impedances. For nodes at the boundary of the computational domain, it is necessary to correct the residual obtained from the convective and diffusive fluxes. To take into account acoustic at inlet and outlet boundary conditions, the residual is modified by translating the boundary condition in a problem of characteristic waves propagation (Struijs, 1994). This method called Navier-Stokes Characteristic Boundary Condition (NSCBC) developed by Poinsot *et al.* (1991) and extended to multi-species flows by Moureau *et al.* (2005) is implemented in AVBP and is used in all simulations presented in this work.

Part II

Single burner ignition

Chapter 5

Literature review on kernel initiation and expansion

Contents

5.1 Phase 1: Initiation of a self-sustained expanding flame kernel

Literally, ignition derives from the Latin *ignire* "set on fire" and designates the initiation of chemical reactions. It is also used in the literature in a broad sense to encompass the subsequent flame propagation and eventually the flame stabilization. In this section, the review is limited to its literal definition and emphasis is given to forced ignition, i.e. using an external source term, in contrast with autoignition. The main insights from the literature in both laminar and turbulent as well as premixed and non-premixed systems are first reported. Then the studies dedicated to the detailed transition from high temperature plasma to flame kernel are briefly reviewed and the models developed to mimic the igniter are listed.

5.1.1 Quiescent/laminar flows

The understanding of forced ignition in quiescent or laminar flow is not of practical importance for gas turbines or ground transportation engines, but it is crucial for fire and explosion safety issues in fuel transport or petrochemical activities. In any case, the case is sufficiently simplified to allow theoretical study that can shed some light on the fundamentals of the ignition process. Theoretical developments that have lead to the concept of Minimum Ignition Energy (MIE) in premixed flows are first reviewed and the effect of the operating conditions or fuel composition highlighted. Then, the effect of partial premixing and two-phase flow is presented.

Early theoretical work on ignition in quiescent mixture uses the fact that for a vast majority of fuel kinetics, heat release is strongly dependent on temperature and comparatively less sensitive to reactant concentrations (Gorbachev, 1981). Thus, during the first instants of ignition, variation of the reactant mass fractions are considered negligible whereas the variations of temperature are taken into account. Then, studying ignition reduces to a thermal balance: the chemical runaway can occur if the rate of chemical heat release in the system exceeds the rate of heat losses to the surroundings. This balance has been first formulated by Semenov (1928) and improved then by Frank-Kamenetskii (1942) in the study of thermal explosion in solids. Deshaies & Joulin (1984) briefly sumarize the results in terms of characteristic times for gaseous mixtures: the time t_{cond} for the initial temperature profile to relax to the surrounding temperature by conduction is estimated by $t_{cond} \propto r_i^2/D_{th}$, where r_i is the initial hot spot size. As for the chemical time t_{chem}, it is derived from a single step irreversible Arrhenius law:

$$t_{chem}(T_i) \propto \frac{1}{\rho \mathcal{A} e^{-E/\mathcal{R}T_i}} \tag{5.1}$$

where T_i is the initial temperature in the hot spot (after energy deposit) and $\mathcal{A}$ and E are the pre-exponential constant and the activation energy of the single step reaction respectively. A critical radius $r_{th,c}$ is obtained for $t_{cond} \simeq t_{chem}(T_i)$:

$$r_{th,c} \simeq \sqrt{\frac{D_T}{\rho \mathcal{A} e^{-E/\mathcal{R}T_i}}} \tag{5.2}$$

More recently Vasquez-Espi & Linan (2002) use the asymptotic analysis first introduced by Berman *et al.* (1981) to study the chemical initiation phase and a model is proposed in terms of Damkhöler number $Da_{ign} = t_{cond}/t_{chem}(T_i)$: ignition occurs for values of Da_{ign} higher than a critical value computed for planar, cylindrical and spherical cases as shown in Fig. 5.1. The study indicates that the critical diameter increases with the number of spatial dimensions considered since the rate of dissipation increases. This study gives one criterion for the size (or energy) of the initial deposit that must be fulfilled for the thermal runaway to occur but is not sufficient to ensure its subsequent propagation.

After the thermal runaway, the reaction starts consuming reactants and their depletion can no longer be neglected (Merzhanov & Averson, 1971). The rate of chemical heat release then depends on the diffusion rate of the limiting reactant towards the reaction zone to overcome the rate of losses to the surroundings. Taking into account the consumption and diffusion of the

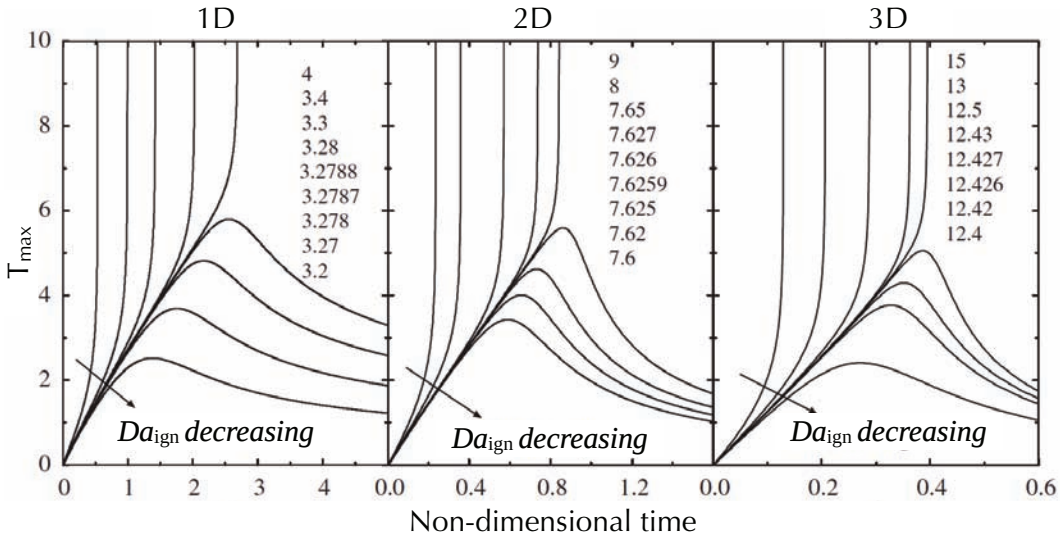

Figure 5.1: Temporal evolution of the temperature at the center of the energy deposit for various Damkhöler numbers Da_{ign}. Extracted from Vasquez-Espi & Linan (2002).

limiting reactant, Zeldovich *et al.* (1980) show the existence of a stationary unstable solution to the conservation equations. This solution consist in a spherical flame of radius r_c for which the reactant diffusion rate towards the flame is such that the chemical heat release balances the outward thermal conduction. This solution is unstable and a stability analysis (Zeldovich *et al.*, 1980) demonstrates that a negative radius perturbation results in a flame collapse while a positive perturbation initiates an outwardly propagating spherical flame. Thus, to generate a self-sustained flame, the energy deposit must drive the flame kernel beyond that critical radius r_c before the kernel temperature drops below the adiabatic temperature T_{ad}. As noted by Joulin (1985), in the case of high temperature hot spot such as encountered with spark deposit ($T_i >> T_{ad}$ (Maly & Vogel, 1978)), $r_{th,c} < r_c$ since $r_{th,c}$ strongly decreases with T_i: energy deposit can be sufficient to initiate the thermal runaway but too weak to drive the kernel beyond the critical size. Experiments show this behavior for propane-air mixture in Olsen *et al.* (1953).

The critical flame radius r_c is strongly dependent on the limiting reactant Lewis number of the limiting reactant (Deshaies & Joulin, 1984; He, 2000): r_c decreases with decreasing Lewis number. Flame initiation is then expected to be more difficult if the limiting reactant is heavier, which is in agreement with experimental observation of Lewis & von Elbe (1987). Starting from the unstable solution of the conservation equation and using high activation energy asymptotic development, Champion *et al.* (1986) explicitly derive a formula for the critical radius r_c:

$$r_c = \frac{\lambda(T_{ad})}{C_p(T_{ad})\rho(T_f)S_L^0}\frac{T_{ad}}{T_b Le_A}e^{\frac{E}{2\mathcal{R}T_{ad}}\frac{T_{ad}-T_b}{T_b}} \tag{5.3}$$

Note that for non-unity Lewis number, the adiabatic flame temperature and the burnt gas

temperature differ. For unity Lewis number mixture, the critical radius reduces to:

$$r_c = \frac{\lambda(T_{ad})}{C_p(T_{ad})\rho(T_f)S_L^0} \tag{5.4}$$

This definition is similar to the definition of the laminar flame thickness (Williams, 1985), but in this case λ and C_p are evaluated at the adiabatic temperature and not at the fresh gas temperature. Other studies report that the critical radius is of the order of the laminar flame thickness (Glassman & Yetter, 2008; Akindele *et al.*, 1982).

The critical energy is then theoretically defined as the energy required to increase to the adiabatic flame temperature of a sphere of radius r_c:

$$E_c = \frac{4}{3}\pi r_c^3 \rho(T_0) C_p(T_0)(T_{ad} - T_0) \tag{5.5}$$

This critical energy often referred as Minimum Ignition Energy (MIE) has been evaluated experimentally in a wide range of conditions representative of internal combustion engines. The extensive experimental study using reported in Lewis & von Elbe (1987) investigates the MIE of numerous hydrocarbons (methane, propane, heptane, ...) over a wide range of equivalence ratio using a spark plug igniter. Experiments shows fairly good agreement with theoretical values: the critical energy is found to be strongly dependent to the equivalence ratio (Lewis & von Elbe, 1987; Ballal & Lefebvre, 1977; Ziegler *et al.*, 1985; Beduneau & Kim, 2003) with a ϕ_{MIE} minimizing MIE in rich mixture. ϕ_{MIE} increases with the number of carbon atoms in the hydrocarbon. These results agree with the theory: MIE is controlled by the diffusion of the heavy hydrocarbon towards the flame front. In accordance with Eq. (5.4), MIE increases when pressure decrease. Ballal & Lefebvre (1975) and Kono *et al.* (1984) experimentally investigate ignition in laminar flow: MIE increases with the bulk flow velocity. DNS of spark ignition in flowing mixture performed by Baum & Poinsot (1995) demonstrates the same trends: the MIE increase is the consequence of convective heat losses and the fact that the energy in deposited on a larger volume.

The main findings from gaseous perfectly premixed flow are still valid for gaseous non-premixed flow, but the location of the spark compared to the stoichiometric mixture fraction iso-line and the lean and rich flammability limits z_{lean} and z_{rich} comes into play. If the ignition location is far from the flammable region, the temperature in the hot spot may decrease below the critical temperature before being able to reach a flammable mixture. The laminar counterflow configuration is often used in the literature to study ignition in non-premixed flames and the effect of strain. The first study of ignition in a laminar counterflow configuration is performed by Rashkovsky (1999), using a point source energy deposit and a one-step chemistry description. This configuration is also used by Richardson *et al.* (2007) using a complex chemistry. The study shows that there is a critical strain rate above which ignition is not possible regardless of the spark position relative to the stoichiometric mixture iso-line. The ignitability limits are found to differ from the mixture flammability limits due to the rapid transport of heat from inflammable regions towards more favorable mixtures.

Finally, ignition in non-premixed two-phase flow reviewed in Aggarwal (1998), is first studied in quiescent fuel mist by Ballal & Lefebvre (1978) by combining experiments with a phenomenological model. Experiments show that the MIE monotonically increases when the fuel droplet

Sauter Mean Diameter (SMD) increases and when the fuel volatility decreases. The MIE is also found to decrease with increasing prevaporized fuel mass fraction at a constant overall equivalence ratio. From these observations, the authors conclude that the ignition process is controlled by the evaporation rate rather than the chemical rate. Ballal & Lefebvre (1978) propose a phenomenaological model which is obtained by comparing t_{cond} with both the evaporation and the burning times of the droplets. Those are experimentally estimated using d^2-law (Sirignano, 1999) and an infinitely fast chemistry approximation. The model is further improved by Ballal & Lefebvre (1979) including convection effects and finite rate chemistry. The first numerical study performed by Aggarwal & Sirignano (1984) brings some new insights on the ignition process in two-phase flow that neither the limited range of equivalence ratios nor the polydispersion of the experiments of Ballal & Lefebvre are able to show. The study indicates the existence of an optimum equivalence ratio for a given droplet diameter and an optimum droplet diameter d_{opt} for a given overall equivalence ratio which minimizes MIE. This behavior is explained by the difference between the gaseous equivalence ratio ϕ_g and the total equivalence ratio ϕ_{tot} (sum of the liquid and gas equivalence ratios) and the dependence of MIE to the gaseous equivalence ratio shown for gaseous premixed flow. Considering a given ϕ_{tot}, droplets with a diameter $d_l > d_{opt}$ are less prompt to evaporate, leading to $\phi_g < \phi_{MIE}$. On the contrary, for $d_l < d_{opt}$ evaporation is faster resulting in $\phi_g > \phi_{MIE}$. d_{opt} is expected to change with fuel volatility or droplet temperature.

Even though quiescent or laminar flows exhibits very little variability, the initiation of the flame kernel is probabilistic due to the variability of the ignition system deposit size and strength (Kono *et al.*, 1984). In case of laminar two-phase flows, the randomness of droplets distribution also introduce stochasticity in the ignition process (Aggarwal & Sirignano, 1984).

5.1.2 Effect of turbulence

When sparking in a turbulent environment, it is difficult to distinguish between failures associated with the generation of a sustainable flame kernel or with the subsequent flame/turbulence interactions. Thus, experiments do not always explain the origin of the ignition failure observed.

A convenient and easy way to investigate the effect of turbulence is to introduce the concept of turbulent diffusivity. Akindele *et al.* (1982) perform a 1D numerical study of an expanding kernel in a turbulent environment. The effect of turbulence is encompassed in the thermal diffusivity $D_{th} = \lambda/(\rho C_p) + D_{turb}$ where D_{turb} is the turbulent eddy diffusivity given by (under the hypothesis of HIT):

$$D_{turb} = 0.44\, u' l_t \left(1 - \exp\left(-\frac{u' t}{0.44 l_t}\right)\right) \tag{5.6}$$

where u' and l_t are the turbulent intensity and turbulent integral length scale respectively. Note that D_{turb} is time dependent, and initially zero. Therefore, diffusion is controlled by the molecular transport at first and turbulent transport takes over later. Using Eq. (5.6) in Eq. (5.2) and Eq. (5.4), one can observe that turbulence increases both the thermal critical radius $r_{th,c}$ and the critical radius r_c. The critical radius is then defined as the radius of the laminar flame kernel when the turbulent transport becomes dominant. Similar approaches are developed in Ballal & Lefebvre (1977) and more recently by Klein *et al.* (2008) to estimate the critical radius. These simplified approaches allow to understand the effect of turbulence in a deterministic sense.

Considering the stochastic nature of turbulence, the MIE must be statistically defined. It is generally accepted to define the MIE as the energy required to obtain a 50% probability of success (Kono *et al.*, 1984; Ziegler *et al.*, 1985). Figure 5.2 displays the MIE experimentally measured in a methane-air mixture for varying equivalence ratio and increasing turbulence intensity (Huang *et al.*, 2007; Shy *et al.*, 2010). For low turbulence intensity, the MIE slowly increases when u'/S_l increases. There is critical turbulence intensity where the slope changes, the MIE increasing then quickly for increasing turbulence intensity. This transition in the ignition process is explained by the change of turbulent combustion regime: the flame switches from a wrinkled flamelet regime to a thin-reaction regime: vortices of significant energy are smaller than the thermal thickness of the flame and modifies the structure of the flame modifying the thermal balance and favoring the diffusion process which results in a rapid increase of the MIE with turbulent intensity. This transition is also observed by Cardin *et al.* (2013) for another experimental set-up and a wider range of equivalence ratios. The study shows that for very lean mixture, the delay for the chain branching reactions to start is increased, increasing the heat losses prior to chemical runaway.

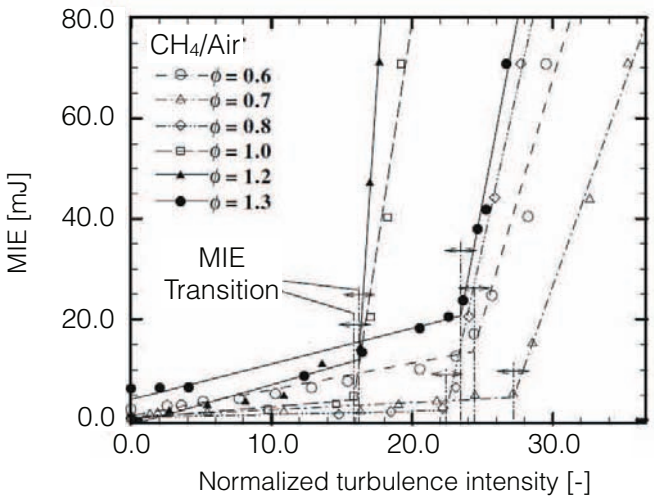

Figure 5.2: Evolution of the MIE in methane-air mixture as function of u'/S_l for various equivalence ratios from Shy *et al.* (2010).

The situation is more complex in non-premixed flows since both velocity and mixture variations control the generation of the flame kernel. As for laminar non-premixed flows, the location of the energy deposit compared to the flammable limits of the mixture determines the initiation of the combustion reactions. For turbulent non-premixed flows, the flammability factor F_f introduced by Birch *et al.* (1981) and Smith *et al.* (1986) enables to evaluate the probability of finding a flammable mixture at a given location by:

$$F_f = \int_{z_{lean}}^{z_{rich}} P(z)\, dz \tag{5.7}$$

where $P(z)$ is the PDF of mixture fraction.The probability of creating a flame kernel P_{ker} is defined as the number of ignition events that successfully initiate a flame kernel over the total number of ignition events. These studies show the strong correlation between F_f and P_{ker}. Cardin (2013) studies ignition in non-premixed homogeneous turbulent flow behind a grid, focusing on

the initiation of the flame kernel ($t < 1\ ms$). In an attempt to discriminate the effects of mixture fraction and the turbulence, the strength of the energy deposit is chosen so that ignition is alway successful when sparking in a premixed case in similar turbulence condition. The authors not only show that the ignition probability is strongly correlated with the mean mixture fraction in the energy deposit region at ignition time (Fig. 5.3 (left)), but also that the amount of fuel in the spark region is also crucial (Fig. 5.3 (right)). The amount of fuel is estimated with F_f where the PDF is constructed from the spatial distribution rather than the temporal distribution as in Birch *et al.* (1981). The study also demonstrates that even though F_f based on the initial field distribution is close to one, the kernel might be quenched due to detrimental conditions encountered later.

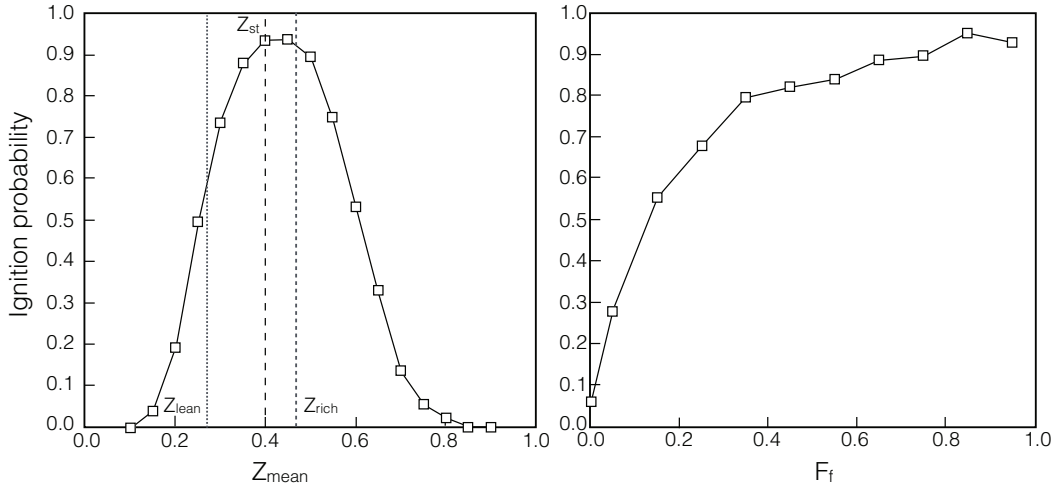

Figure 5.3: Evaluation of the ignition probability as function of the mean mixture fraction in the deposit region (left) or the amount of fuel in the same region (right). Extracted from Cardin (2013).

Ahmed & Mastorakos (2006) study the ignition probability in a turbulent methane jet where transport comes into play. The study demonstrates that $P_{ker} < F_f$ in region of high aerodynamic strain and demonstrates the joint effect of mixture and turbulence on the ignition probability. Results also reveals that P_{ker} can be non zero in regions where $F_f = 0$ which confirms the possibility to ignite by transport of heat from non flammable mixture zones as indicated in the laminar set-up of Richardson *et al.* (2007). The same distinction between F_f and P_{ker} is also observed by Ahmed *et al.* (2007*a*) in a bluff-body recirculating flow configuration: regions with F_f close to unity are showed to have P_{ker} of about 20% due to the high diffusion induced by turbulence. The maps of P_{ker} and F_f extracted from Ahmed *et al.* (2007*a*) are reported in Fig. 5.4: the results depict a large central region where $F_f \simeq 1$ but P_{ker} is low: this region corresponds to the recirculation bubble in the wake of the bluff body where turbulence is intense.

5.1.3 Models to mimic energy deposit

So far, the question of the igniter model has not been addressed. The fairly good agreement with the experiments of theoretical developments considering the igniter as an idealized energy source

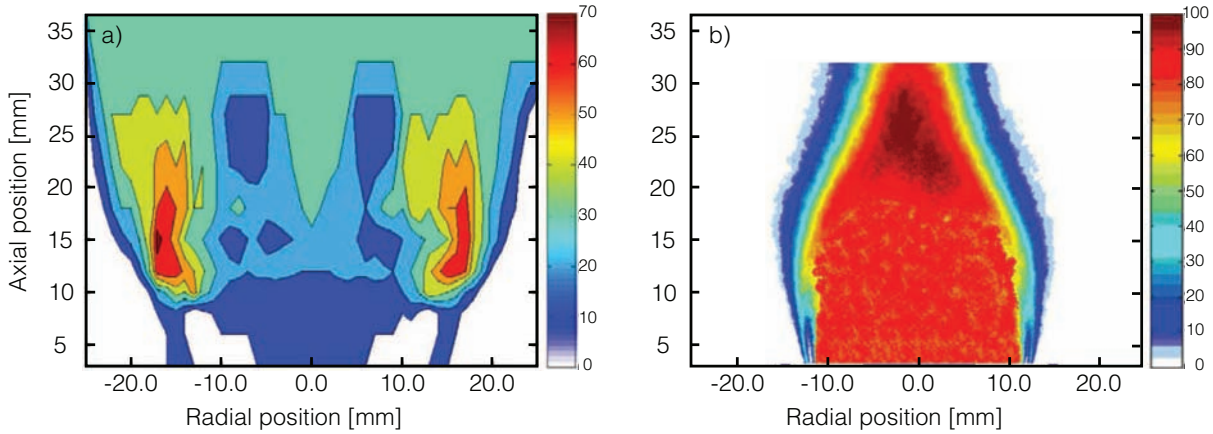

Figure 5.4: Spatial distribution of P_{ker} (a) and F_f (b) in a bluff-body methane/air burner. Extracted from Ahmed *et al.* (2007*a*).

term indicates that this strong approximation might be sufficient to study ignition. Nonetheless, questions remain open regarding the effect of the arc shape and deformation on the subsequent kernel formation, especially in turbulent flows. The exact composition of the gaseous mixture following the plasma phase is also unknown and could significantly affect the initiation of the chemical reactions.

As described by Maly & Vogel (1978), the generation of a flame kernel by a spark plug is subsequent to the creation of a plasma in the spark channels. But the complete simulation from the spark discharge to the creation of a flame front is not an easy task since the physics of plasma is not fully understood. Several attempts are conducted by Sher *et al.* (1992) or Kravchik *et al.* (1995) to couple the Navier-Stokes equations with a statistical thermodynamic model in order to capture the physics of the plasma phase. These studies show that the transition from the spark to the flame kernel could be split in two steps:

- during less than 5 μs, the pressure wave controls the plasma kernel expansion. The velocity is high compared to the flame speed and the chemical heat release is negligible
- a diffusive period follows, during which energy and mass are transferred from the plasma towards the unburnt mixture and a chemically active zone is created at the spark kernel surface.

More recent studies by Thiele *et al.* (2000) and Thiele *et al.* (2002) focus on the coupled resolution of the gaseous flow with the Navier-Stokes equations and complex transport, and the electric field using the Maxwell equations in order to model the spark. An experimental study is performed in parallel to validate the numerical results. The influence of the spark arc phase duration and electrode shape on the kernel expansion was found to be negligible in the studied temperature and pressure ranges.

Considering the grid resolution for LES, the creation of the plasma, the transition to a chem-

ically sustained kernel and its early expansion cannot today be explicitly included in LES simulations. Several models have been therefore proposed to externally solve the small-scale physics in 0D or 1D, mainly in the context of internal combustion engines, and then use the results as an input in LES or RANS:

- Boudier *et al.* (1992) solve for the first laminar expansion phase of the kernel in 0D and project the kernel on the LES grid once the turbulent stretch dominates the laminar one.
- The ATKIM model developed by Duclos & Colin (2001) for RANS simulations at IFPEN is composed of several elements: 1) a model for electrical circuit, 2) a description of the electrical arc using lagrangian particles, 3) tracking of multiple spark kernels that could result in a burnt gas kernel, and 4) fixed lagrangian particles to emulate the presence of the electrodes and estimate the heat losses. The model has been extended to LES in Richard *et al.* (2007), and the tracking of the spark kernel is replaced by a progress variable coupled to the flame surface density equation of the CFM-LES model.
- In the context of RANS simulations of two-phase flow gas turbines Ouarti *et al.* (2003), Garcia-Rosa *et al.* (2009) and Linassier *et al.* (2013) at ONERA developed a model to compute the early kernel laminar growth in a two-phase flow in a 1D configuration based on the flow properties at the spark deposit location.

A simpler model to mimic energy deposit is used in many DNS (Poinsot *et al.*, 1991; Baum & Poinsot, 1995; Chakraborty *et al.*, 2007) and LES (Lacaze *et al.*, 2009*a*; Jones & Prasad, 2011) studies where the spark is reduced to a source term in the transport equation for gaseous energy. The spatial and temporal distribution of the source term is found to vary between these studies (Gaussian distribution, hyperbolic tangent or Heaviside functions in both space and time). Finally, Sloane (1985) investigates ignition in quiescent methane-air mixture by addition either of a thermal energy source term or of both thermal and free radicals (H and O) source terms. The results indicate that, for the chemical scheme considered, the effect of free radicals addition is negligible, supporting the assumption that ignition is mainly driven by the thermal balance.

5.2 Phase 2: kernel expansion and transient flame propagation

If the energy deposit is sufficient to initiate chemical reactions and generates a sustainable flame kernel, the kernel must then be able to grow and the flame front must propagate to eventually stabilize on the injector nozzle (Lefebvre, 1998). Following Mastorakos (2009), the literature review proposed here for **Phase 2** of ignition is further split in two: first, the development of an isolated flame kernel interacting with turbulence (Sec. 5.2.1) and second, the ignition sequence in a complex turbulent flow where the convection of the flame front comes into play (Sec. 5.2.2).

5.2.1 Development of isolated flame kernel

Once a flame kernel is established, its survival depends on the turbulence level and the interactions between the turbulent flow and the flame front. Indeed, turbulence can induce deformation

and fragmentation of the kernel, wrinkling and stretching of the flame front as well as enhancement of the diffusion process. If it is well known that turbulence can have a beneficial effect on the burning rate of the flame, it can also induce local or global extinction of the flame kernel during the first few milliseconds after energy deposit. The study of a spherical flame kernel expansion without or with turbulence has been widely studied experimentally since it constitutes a canonical case to investigate laminar and turbulent burning velocity (Karpov *et al.*, 1959; Abdel-Gayed *et al.*, 1984; Weiss *et al.*, 2008; Galmiche *et al.*, 2012). However, only recent progress both in optical diagnostics and numerical simulations have allowed detailed investigation of the local flame front properties during the kernel development. Except for very intense turbulence, the early instants of kernel expansion are laminar due to the increase of viscosity with temperature, the small size of the kernel and the very short deposit duration. As time proceeds, the kernel transitiones to a turbulent expanding flame when vortices of increasing size start interacting with the flame.

5.2.1.a Transition from laminar to turbulent flame propagation

Initially, the burning velocity is controlled by the laminar stretch associated with the kernel expansion (Poinsot *et al.*, 1991). The stretch of a freely, outwardly propagating flame is expressed in terms of surface variation by (Poinsot & Veynante, 2011):

$$\kappa = \frac{2}{r_k}\frac{dr_k}{dt} \tag{5.8}$$

where r_k is the kernel radius. The laminar stretch is maximal for small radius and decreases as $1/r_k$ as the kernel expands (Renou, 2001). The overall growth rate of the kernel during the laminar phase strongly depends on the Lewis number of the fuel: for $Le_F < 1$, the stretch increases the flame consumption rate. It is the opposite for $Le_F > 1$ (Poinsot & Veynante, 2011). Since $Le_F < 1$ combustion flames are prone to thermo-diffusive instabilities, the Lewis number can also induce an increase of the flame surface enhancing the overall consumption rate (Poinsot *et al.*, 1991; Renou *et al.*, 2000) and trigger a faster transition to turbulent flame propagation. During this early phase, the flame kernel is only sensitive to turbulent scale having a turnaround time of the order of the time elapsed since the energy deposit (noted $t_{elapsed}$) (Abdel-Gayed *et al.*, 1988). Turbulent scales larger than the kernel size cause a bulk motion of the flame kernel with limited effect on its growth rate (at least in premixed flows). As time proceeds, the kernel grows and starts interacting with larger and more energetic turbulent scales, and the turbulent stretch becomes dominant. To represent this effect, Abdel-Gayed *et al.* (1988) introduce the concept of effective turbulent velocity u'_{eff}: it can be evaluated by the area under the curve of power spectral density versus frequency between the cut off frequency of the kernel given by $f_{ker} = 1/t_{elapsed}$ and the Kolmogorov frequency as illustrated in Fig. 5.5. At first u'_{eff} is zero and it progressively increases toward the overall turbulent velocity u'. u'_{eff} When $t_{elapsed}$ becomes larger than the turnaround time, $u'_{eff} \sim u'$. This concept is supported by both spark and laser ignited experiments (Abdel-Gayed *et al.*, 1987; Bradley *et al.*, 2011).

Bradley *et al.* (2004) Laser Induced Breakdown (LIS) experiments reported in Fig. 5.6 illustrate the effect of the effective turbulent velocity on the kernel growth rate: the kernel radius temporal evolution is similar in both laminar and turbulent environments during the early instants and diverge later. The time at which the temporal evolutions diverge is found to decrease

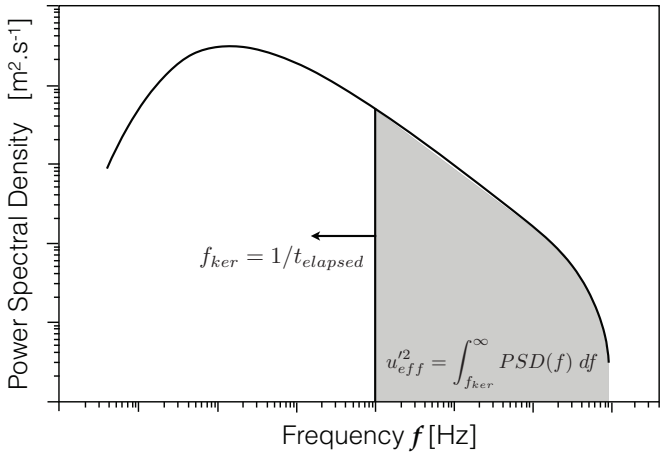

Figure 5.5: Frequency band of PSD used to evaluate the effective turbulent velocity u'_{eff}. Adapted from Abdel-Gayed *et al.* (1988)

with increasing turbulent intensity since the Kolmogorov length scale decreases. This trend is in accordance with the numerical results reported in Akindele *et al.* (1982).

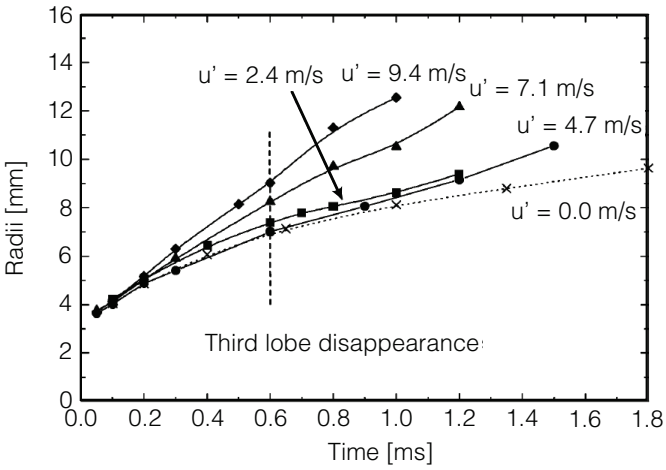

Figure 5.6: Temporal evolution of kernel equivalent radius for LIS ignition at various turbulence intensity levels. Extracted from Bradley *et al.* (2004)

In partially premixed or non-premixed flows, the early kernel growth rate is found to be well correlated with the amount of flammable mixture at the deposit location as shown by Cardin (2013). Two cases have to be considered separately depending on whether the distribution of mixture fraction stays on one side of the stoichiometric mixture fraction line (whether rich or lean) or spreads across z_{st} (Peters, 2000; Mastorakos, 2009). The former corresponds to stratified mixture ignition whereas the latter is referred to as non-premixed ignition. In the case of stratified mixture ignition, the kernel growth is quite similar to a premixed kernel expansion with spatial heat release variation due to inhomogeneity (Renou *et al.*, 2004). The local burning

rate variations induce wrinkling of the flame front which is found important for weakly turbulent cases but negligible for strongly turbulent flows as compared to aerodynamic wrinkling (Poinsot *et al.*, 1996). For non-premixed ignition, the flame front rapidly turns into a triple flame propagating along the stoichiometric iso-contours (Hartley & Dold, 1991; Chakraborty *et al.*, 2007). The growth rate of the flame kernel then depends on the ability of the triple flame to propagate: because the rich premixed branch of the triple flame exhibits higher reaction rates than its lean counterpart, the initial kernel growth is enhanced for overall richer mixture (Chakraborty & Mastorakos, 2008).

5.2.1.b Effect of turbulence on the flame kernel

As larger and more energetic scales start interacting with the kernel, wrinkling of the flame front is observed (Poinsot *et al.*, 1991; Kaminski *et al.*, 2000). As compared to a laminar case, the increase of flame surface associated with wrinkling enhances the kernel growth. The effect of u' on the flame surface is found to increase with increasing turbulent intensity, up to the point where local quenching of the flame front overcomes the beneficial effect of the higher flame surface. Indeed, development of the flame kernel after the transition is fairly similar to a turbulent flame propagation, so that the influence of turbulence on the kernel growth can be analyzed in a classical combustion diagram (Borghi, 1985; Peters, 1986). As the turbulent intensity increases, the flame/turbulence interaction regime goes from the wrinkled flamelet regime where the flame structure is that of an unstretched laminar flame, to the thin reaction zone regime where the vortices penetrate in the preheat zone, and eventually to the distributed reaction zone regime if the turbulence intensity further increases. The last two regimes are characterized by a modification of the flame structure and possible quenching by turbulence since the turbulent time scales are of the order (or smaller) of the chemical time scale.

To clarify the effect of the turbulence on the flame kernel, it is interesting to analyze the interaction of a flame kernel with a single vortex of varying size and strength. Initial experiments conducted by Eichenberger & Roberts (1999) and followed by Xiong *et al.* (2001) and Xiong & Roberts (2002) show enhancement of the overall burning rate for small vortex size but also local or overall flame quenching for vortex of size similar to the kernel. The DNS study of Kolera-Gokula & Echekki (2006) for premixed hydrogen-air mixture similarly reveals an increase of the overall growth rate due to distortion of the flame kernel and distinguishes two interaction regimes: the breakthrough regime where the vortex is strong enough to go through the kernel without global extinction, and the global extinction regime where larger vortices inducing global quenching of the kernel. Both regimes are characterized by a strong wrinkling of the kernel, flame-flame interaction and annihilation and strong effect of strain and curvature. This work is followed by the parametric study of Echekki & Kolera-Gokula (2007) in an attempt to build a kernel-vortex spectral diagram similar to classical spectral vortex/flame diagrams (Poinsot *et al.*, 1991). The diagram of Vasudeo *et al.* (2010) is reported in Fig. 5.7(a).

- In the **laminar regime**, characterized by small and/or weak vortex, the kernel is merely distorted and the vortex quickly dissipated by the increase of temperature through the flame front.
- As the size and strength of the vortex increase, the interaction enters the **wrinkled regime**

where large deformations of the kernel are observed and the vortex is able to penetrate in the kernel. However, the vortex is dissipated and does not break the leading edge of the kernel.

- If the size and/or strength further increases, the **breakthrough regime** is observed.
- Finally the **global extinction regime** is encountered for large and/or strong vortices.

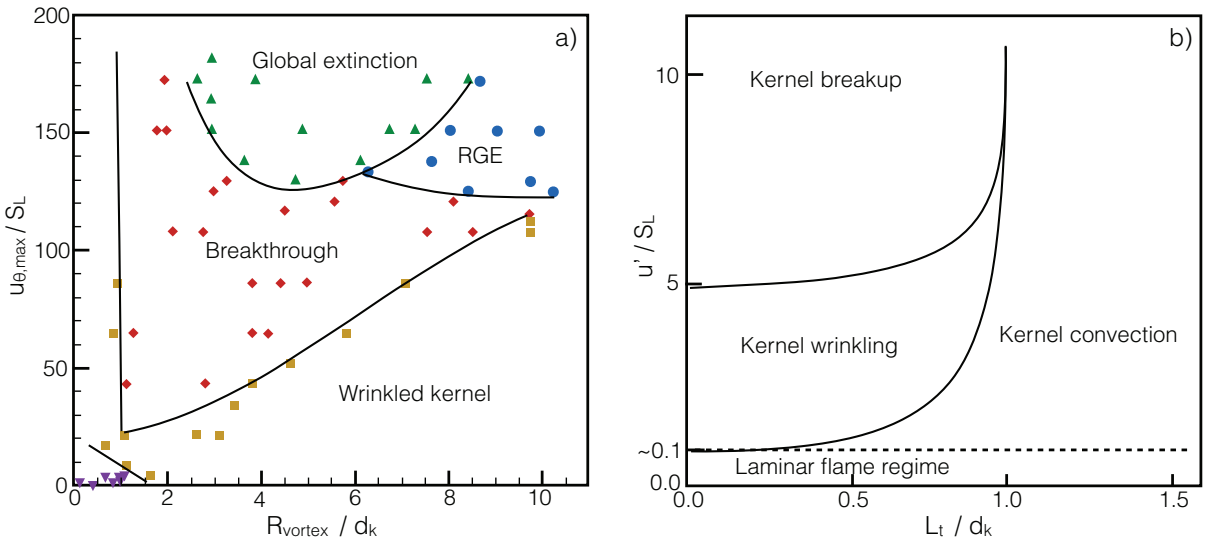

Figure 5.7: (a) Kernel-vortex interaction spectral diagram of Vasudeo *et al.* (2010). (b) Kernel-turbulence interaction map of Reddy & Abraham (2013)

Vasudeo *et al.* (2010) had a fifth regime (called Regeneration after Global Extinction (RGE) regime) in case where the vortex is strong enough to break the kernel into peaces but the flame front is reconstructed after the vortex has passed by. Both studies of Vasudeo *et al.* (2010) and Reddy & Abraham (2011) point out the effect of the chemical description on the kernel-vortex interactions: if a simple chemistry is able to capture the effect of strain and curvature as well as the main overall kernel growth, it might fail to reproduce local extinction and re-ignition associated with flame-flame interaction or kernel reconstruction. When considering kernel growth in a full turbulence spectrum, the resulting interaction cannot simply be viewed as a superposition of isolated vortices of various size and strength due to coupling and interaction between these scales. Reddy & Abraham (2013) perform 2D DNS of flame kernel interaction with fully developed turbulence in conditions representative of internal combustion engines with detailed chemistry. The study focuses on the kernel growth rate and highlights the influence of the parameter l_t/d_{ker} where d_{ker} is the kernel diameter. A kernel-turbulence interaction map is proposed (see Fig. 5.7(right)): regimes similar to kernel-vortex diagram are found, and the maximum growth rate is found in the kernel wrinkling regime.

The effect of turbulence on ignition in non-premixed cases is not easy to evaluate because of the coupling between velocity and mixture fraction fluctuations. Chakraborty *et al.* (2007) perform 3D DNS of forced ignition in a turbulent mixing layer with one-step chemistry. The study proves

that an increase of turbulent velocity is detrimental to the kernel growth since it results in an increase of the mixture fraction gradient, which in turn slows the triple flame propagation (Ko & Chung, 1999; Buckmaster, 2002).

Note that most of these DNS studies are limited to 2D configurations, but Thevenin *et al.* (2002) show that the maximum stretch undergone by the flame is higher in 3D and the curvature distribution is shifted towards positive values in 2D configurations. The differences between 2D and 3D curvature distributions are also highlighted in Gashi *et al.* (2005) by comparing 2D OH-PLIF measurement and 3D DNS results, so that it is necessary to be cautious when estimating three dimensional flame properties from 2D measurements or simulations.

All these studies show that the flame kernel growth is maximal in the wrinkled regime where the flame surface increase is beneficial to the overall burning rate with very little local extinction.

5.2.1.c Quenching mechanisms

The mechanisms leading to quenching of the kernel flame front is first studied using DNS, since the simultaneous measurement of the flame position and the velocity field is a complex task. The recent development of advanced optical diagnostics (Trunk *et al.*, 2013; Kerl *et al.*, 2013) allows to bring some new insight on the flame kernel development (Peterson *et al.*, 2015) and to validate numerical findings. Two mechanisms leading to local or global quenching of the flame kernel can be distinguished: 1) the modification of the kernel structure by large scale turbulence and 2) the modification of the flame structure by vortices which sizes are of the order of the flame front.

The first DNS of expanding flame kernel in premixed environment is performed by Poinsot *et al.* (1991) in a 2D decaying turbulence, for which no global quenching is reported. But the study points out the occurrence of 'catastrophic' events where pockets of burnt gases are separated from the kernel and can subsequently be quenched, resulting in a temporary reduction of the kernel growth rate. Such events are also captured in 3D DNS at various levels of turbulence and equivalence ratios performed by Fru *et al.* (2011). The frequency of pinch off events, where mutual flame annihilation creates pockets of hot gases in fresh gases, increases with the turbulent intensity. The temporal evolution of a flame kernel in intense turbulence extracted from Fru *et al.* (2011) show in Fig. 5.8 illustrates the strong wrinkling of the flame kernel and the creation of pockets.

This mechanism is also observed in the DNS of kernel-vortex interactions where significant flame surface destruction was captured in the breakthrough or quenching regime where large vortices interact with the flame kernel (Vasudeo *et al.*, 2010). The resulting pockets can either collapse if their size is too small (typically following the sustainable flame kernel criterion introduced in Sec. 5.1) or expand and contribute to the ignition process.

The second mechanism inducing local quenching is not specific to kernel propagation but results of the interaction of turbulence with the flame front. Unlike the first quenching mechanism which can occur at relatively low turbulence intensity, the second mechanism is observed in the thin-reaction zone regime (Peters, 1999), i.e. when vortices are sufficiently small to enter the preheat layer of the flame but too large to enter the reactive layer. Jenkins *et al.* (2006) perform 3D DNS of flame kernel propagation to evaluate the effect of strain rate and curvature on the

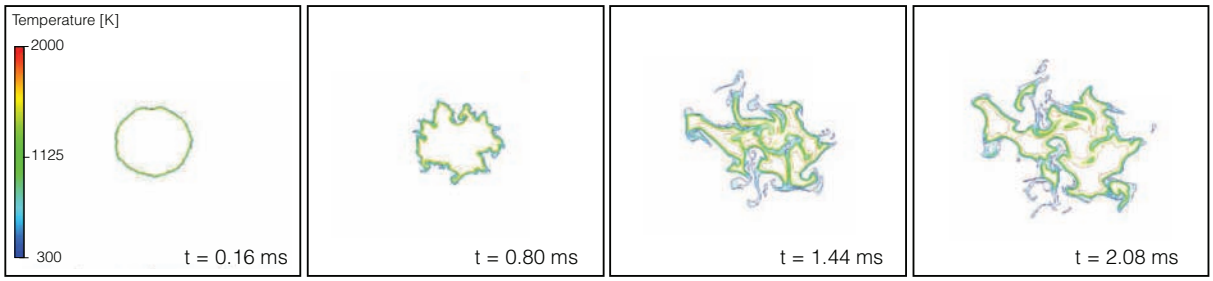

Figure 5.8: Temporal evolution of temperature iso-contours of flame kernel in decaying isotropic turbulence at $Re_T = 2462$. Extracted from Fru *et al.* (2011).

flame structure and propagation. To analyze the DNS data, the flame displacement speed S_d introduced by Echekki & Chen (1996) (Sec. 3.2.1.b) is used. The mean positive curvature experienced by the spherical flame front is found to be detrimental to the flame displacement speed due to an increase of the tangential diffusion component (as compared to a statistically planar turbulent flame). In a similar case, Klein *et al.* (2006) show that for high positive curvature, negative S_d could be found where the rate of thermal diffusion dominates that of heat release. Note that notion of negative S_d does not pertain to the flame consumption rate but to the propagation of a c iso-level relative to the flow. Negative displacement speeds have also been captured experimentally by Peterson *et al.* (2015) during the flame development following sparking in an internal combustion engine using 4D measurements. The study, however, shows no evidence of correlation between S_d and the curvature of the flame front as observed in DNS studies. Studies have indicated that $S_d < 0$ can be used an indicator of local extinction (Gran *et al.*, 1996; Chen & Im, 1998; Kolera-Gokula & Echekki, 2006). The occurrence of local extinction can then be related to the distribution of curvature: the studies of Jenkins & Cant (2002) and Reddy & Abraham (2013) indicate the broadening of the curvature PDF for increasing values of turbulent velocity u'.

5.2.2 Ignition of single burner configuration

The overall ignition success of a single burner is not solely guaranteed by the capacity of the flame kernel to overcome the detrimental effect of turbulence. In complex flow, the outcome of the ignition sequence depends on the ability of the flame to propagate and stabilize at the injector nozzle. Because the incoming flow velocity is generally much higher than the turbulent flame speed, practical injection systems generate recirculation zones which provide pathways for the flame to propagate from downstream location to the injector nozzle. The study of flame propagation following initiation of a flame kernel is rather recent and motivated by the new design trends. It requires well equipped complex experimental set-ups and computationally expensive numerical investigations.

5.2.2.a Jet configuration

The early works of Birch *et al.* (1981) and Smith *et al.* (1986) focus on the ignition of a turbulent free jet. The flame front propagation is not investigated in detail but the authors show that allthough the probability of creating a flame kernel P_{ker} along the jet axis correlates well with the flammability factor F_f, the overall ignition is not guaranteed. Two scenarios are identified: either flame propagates downstream and eventually blows-off or flame propagates upstream, against the flow, and results in a stable flame. A similar configuration is studied in Ahmed & Mastorakos (2006) with the objective of providing a detailed understanding of the flame propagation mechanisms at various stages of the ignition sequence. The results indicate that the region of non zero ignition probability is wider than the contours corresponding to the lean and rich flammability limits. This result is coherent with the observation of Richardson & Mastorakos (2007) in a laminar counterflow flame: the transport of energy from a spark location outside of the flammability contours to a flammable region can result in a successful ignition. Ahmed & Mastorakos (2006) demonstrate that the initially spherical flame kernel quickly turns into an edge flame due to the non-premixed configuration and the flame front propagates upstream along the stoichiometric iso-lines at a mean speed three to six times the laminar flame speed. The experimental configuration of Ahmed & Mastorakos (2006) is studied numerically using LES in Lacaze *et al.* (2009*b*) and Jones & Prasad (2011). Both numerical studies use a Gaussian source term in the energy equation to trigger ignition but Lacaze *et al.* (2009*b*) use the thickened flame model to handle the flame on the LES grid while Jones & Prasad (2011) use sub-grid *pdf* model. The two numerical studies are in good agreement with experimental data for the non-reacting flow as well as in terms of ignition phases. A comparison of the direct visualization of the flame extracted from experiments and the temperature field extracted from the LES of Lacaze *et al.* (2009*b*) is showed in Fig. 5.9. The triple flame propagation behavior and the lift-off distance are recovered by both LES studies, proving the capability of LES to capture the complex ignition transient.

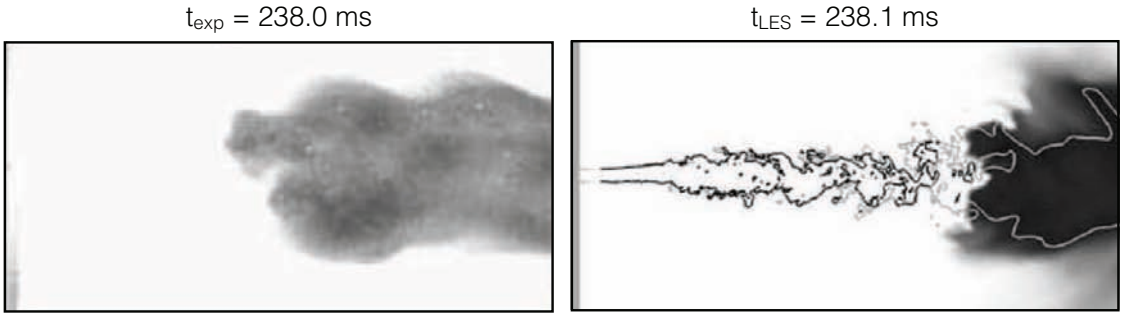

Figure 5.9: Ignition of a free jet burner: experiments from Ahmed & Mastorakos (2006) (left) versus temperature field (grayscale) in the LES of Lacaze *et al.* (2009*b*) (right)

5.2.2.b Recirculating flow configuration

Gaseous experiments

To study the *Phase 2* of ignition in a flow closer to real combustion chambers, Ahmed *et al.*

(2007*a*) experimentally investigates ignition in a non-premixed complex flow configuration exhibiting recirculation zones induced by a bluff-body. Both velocity and mixture fraction are measured to analyze the non-reacting flow and the flame position during ignition sequences tracked by high speed OH PLIF. Examples of flame snapshots during an ignition sequence is shown in Fig. 5.10. Failed and successful ignition events are visualized and ignition probability map is constructed. Three types of ignition failure are observed: failure of kernel initiation, blow-off of propagating flame kernel and global extinction after flame propagation and stabilization. The relation between flammability factor, kernel probability and ignition probability is investigated without and with swirl motion. The direction of flame propagation is proven to be related to the energy deposit location rather than to the instantaneous flow conditions at the energy deposit. An important finding is that the differences between ignition probability and flammability factor are mainly due to nonlocal effect (advection) and quenching by turbulence (Abdel-Gayed & Bradley, 1985).

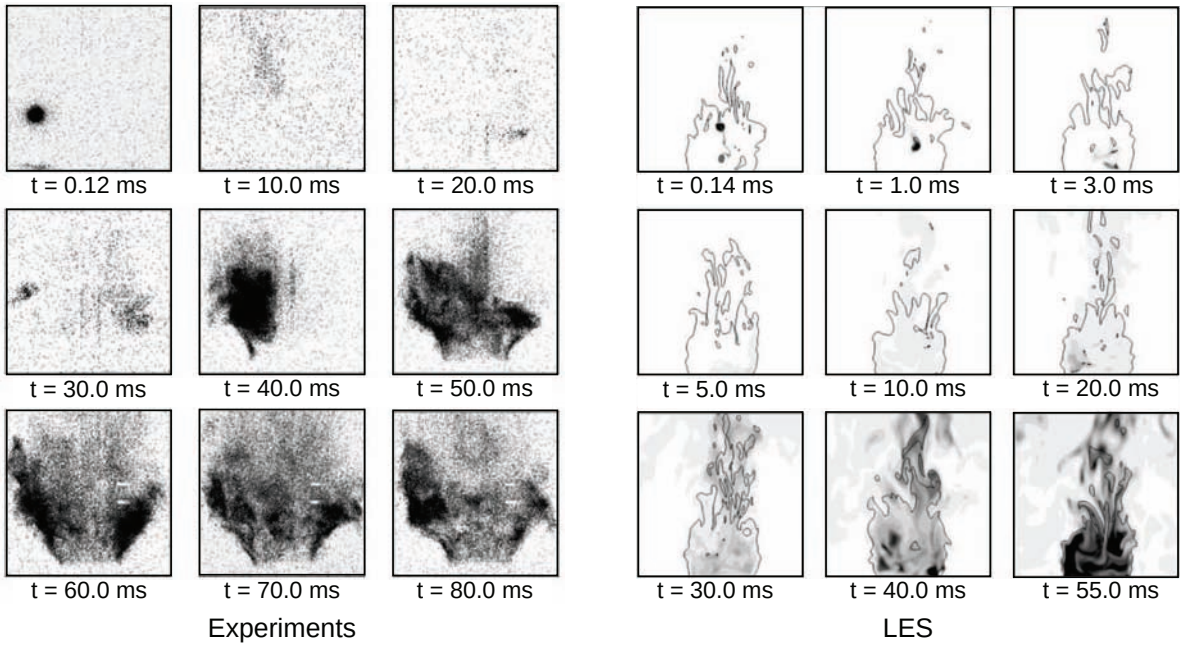

Figure 5.10: Ignition sequence in a non-premixed bluff-body burner: experiments from Ahmed *et al.* (2007*a*) and temperature field in the LES computation of Subramanian *et al.* (2010).

Cordier (2013) designs a lean swirled burner close to realistic lean burn aeronautical injection systems to study ignition in premixed and non-premixed configurations for two different swirl intensities. The ignition performances of the burner are evaluated by constructing ignition probability maps. Cordier *et al.* (2013*a*) show that the ignition efficiency is not only controlled by the local flow properties but also by the kernel trajectory. The mean effect of the swirl intensity is an increase of the turbulent intensity which can locally quench the flame kernel, but can also have a beneficial effect on the ignition probability due to changes of the flow aerodynamics. For the partially premixed case, the local increase of equivalence ratio enhances the ignition efficiency but has also detrimental effect in regions where air and methane are insufficiently mixed. Cordier *et al.* (2013*a*) and Cordier *et al.* (2013*b*) also construct ignition scenarios based on high

speed flame visualization pointing out the occurrence of kernel fragmentation and the subsequent quenching induced by turbulence.

Corresponding LES studies

The bluff-body configuration of Ahmed *et al.* (2007*a*) is numerically studied using two LES solvers with different combustion models: Triantafyllidis *et al.* (2009) use a detailed chemistry with Conditionnal Moment Closure (CMC) model while Subramanian *et al.* (2010) employ tabulated chemistry and a presumed-*pdf* model. Triantafyllidis *et al.* (2009) find a flame development very similar to the experimental results, and their results show that a detailed chemistry mechanism is necessary to reproduce the expansion rate. The flame kernel trajectory is found to depend on the spark location in accordance with experiments. Subramanian *et al.* (2010) show that sparking at the same location but varying deposit timing can lead to either ignition success or failure depending on the convection direction during the first instants after energy deposit. Two mechanisms are found to jeopardize the ignition success in region with favorable convection direction: quenching near the bluff-body wall and high strain rate encountered by the flame kernel. This last point shows that the effect of strain rate must be taken into account in the combustion closure modeling.

The premixed configuration of Cordier *et al.* (2013*a*) is studied in the work of Barré (2014). In this study, a two-step global chemistry along with the thickened flame model are used and the author indicates that during the early instants after sparking, the grid resolution should be chosen as to minimize the contribution of the combustion closure since it could alter the outcome of the ignition try. The key role of the combustion closure is further highlighted during the flame propagation through the combustion chamber: comparison of temporal pressure signals with experimental data shows that a closure adequate for highly turbulent regions results in overestimation of the sub-grid contribution in near laminar regions. The quenching mechanisms are investigated using both diagnostics of the flame displacement speed S_d and joint contributions of strain and curvature to flame stretch. The results are in accordance with the DNS study of Klein *et al.* (2008).

Two-phase flow experiments

The experiment of Marchione *et al.* (2009) is today the only detailed analysis of ignition in a two-phase flow environment. A swirling n-heptane academic burner is studied and high ignition probability is found to be correlated with regions of backward velocity and small droplet SMD and to coincide with location of total equivalence ratio (liquid and vapor) within the flammability limits. Multiple spark sequences are also investigated: the ignition efficiency is shown to increase with the ignition sequence duration. A similar configuration is studied in Letty *et al.* (2012) where the effect of swirl and fuel are briefly investigated. The three failure modes mentioned above are captured for both ethanol and n-heptane in the swirling configuration. Eyssartier *et al.* (2013) perform ignition sequences in the MERCATO configuration of Garcia-Rosa *et al.* (2011) at atmospheric conditions. The study focuses on the construction of a model to predict ignition probability, but the early instants of several ignition sequences are simulated with two-phase flow LES and large variability in the flame kernel development is captured.

5.2.2.c Realistic combustor

Experimental study of ignition in realistic temperature and pressure conditions have been conducted by Read *et al.* (2008), Read *et al.* (2010) and Garcia-Rosa *et al.* (2011). Detailed data on the velocity field and the spray pattern are not available is these studies due to the complexity of the test facilities. Read *et al.* (2010) study the ignition of a LDI injector by direct imaging of the kernel development in the combustor and failure modes similar to the one captured in Ahmed *et al.* (2007*a*) are observed. The study also shows a rapid disintegration of the flame kernel and convection of the fragments throughout the combustor. Figure 5.11 shows an ignition sequence in the test bench proposed by Garcia-Rosa *et al.* (2011). Right after energy deposit, the flame visible emissions are weak. The experiment shows that in realistic conditions, the kernel phase is quite long: the flame is convected downstream (in the right direction in Fig. 5.11) with little expansion. After 16 ms, the flame front rapidly expands in the whole chamber and eventually stabilizes on the nozzle.

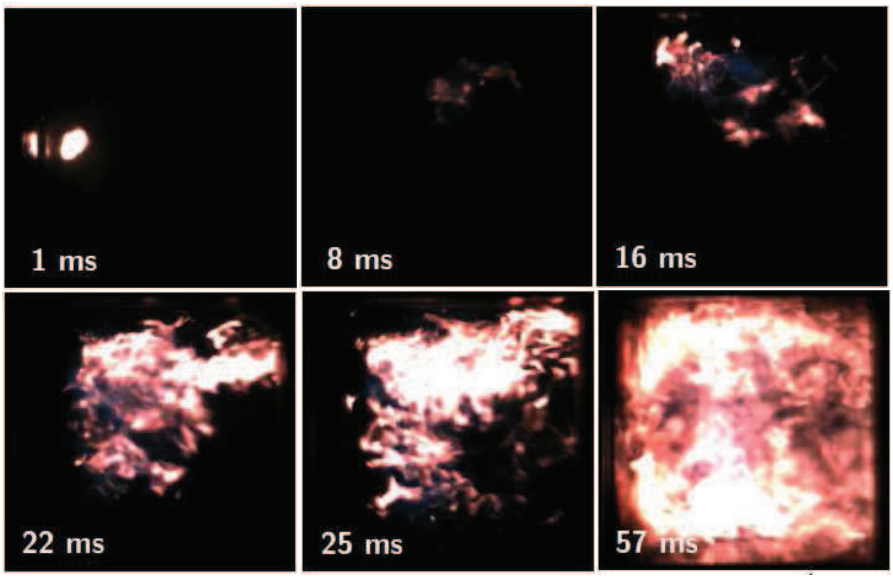

Figure 5.11: Ignition sequence in realistic two-phase flow combustor extracted from Garcia-Rosa *et al.* (2011).

Ignition sequence in realistic (but simplified) combustion chamber sector is performed in Boileau (2007) to demonstrate the feasibility of such computation with LES using an Eulerian dispersed phase formulation. Jones & Tyliszczack (2010) investigated the ignition sequence of a realistic gas turbine sector including the multiphase flow description, but in atmospheric conditions, using LES. A sub-grid *pdf* approach similar to the work of Jones & Prasad (2011) is employed for closure of filtered conservation equations, and a Lagrangian formulation is used for the liquid phase. Both ignition failure and success are obtained as function of the spark size and sparking timing but very little is reported regarding the precise effect of two-phase flow on the kernel development and flame propagation.

5.3 Conclusion

This review clarifies the key elements controlling the *Phase 1* of ignition in gas turbines but note that in gas turbine the spark igniter is generally sufficiently strong to initiate chemical reaction, regardless of the turbulence level at the spark location. Hence, the success of this phase is mainly conditioned upon the ability of the flow to provide a flammable mixture at the vicinity of the spark location.

The review on *Phase 2* of ignition demonstrates that the distinction introduced by Mastorakos (2009) between the development of isolated kernels and the subsequent flame propagation and stabilization is relevant since they are governed by different mechanisms:

- Kernels developing in turbulent flows are subjected to aerodynamic constraints that can either result in a faster growth rate, mainly due to an increase of the kernel surface, or in a quenching of the flame kernel. The later is found to be related to both the dislocation of the kernel structure and the imbalance between chemical heat release and heat losses associated with turbulent mixing. In non-premixed flow, the kernel rapidly turns into a propagating edge flame also highly sensitive to aerodynamic strain.
- The success of ignition in single burner configurations is mainly controlled by the residence time of the kernel in the burner. Indeed, long residence times allow to increase the temperature in recirculating regions, the key element of flame stabilization. The spark position should be such that flammable mixture is available nearby and the large scale flow motions bring the flame kernel towards low or backward velocity regions where it can propagate upstream. Otherwise, the kernel can be blown out even though the conditions necessary for its growth are met.

The literature review also highlights that numerical simulations have greatly contributed to the understanding of the ignition process through DNS of flame kernel development and more recently, LES of ignition sequences in complex configurations. Nonetheless, the validity of the LES approach for conditions approaching realistic gas turbines have not been fully demonstrated and the mechanisms leading to ignition failure in non-premixed, highly turbulent flows are not fully identified.

Chapter 6

Non-reacting flow in the KIAI single burner

Contents

Knowledge for ignition, acoustic and instabilities (KIAI) project is a FP7 european research project coordinated by SNECMA whose goal is to deliver CFD tools able to study unsteady phenomena in gas turbines. In the framework of the KIAI project, joint experimental and numerical studies of ignition in a single sector and a multi-burner configuration are performed. The single injector test rig is installed at CORIA (Rouen, FRANCE) and has been designed during the work of Frenillot (2011) and Cordier (2013).

Prior studying the ignition performance of the burner, the non-reacting flow is investigated in LES with two main objectives:

- Compare LES results with experiments and evaluate the sensitivity of the LES to numerical parameters. The influence of subgrid stresses model, numerical scheme, wall treatment and mesh refinement is especially targeted.

- Provide a complete description of the flow and precise data to identify the effect of the aerodynamics and mixture on the ignition sequence.

6.1 Experimental test rig

The KIAI test rig ams to study ignition, from the energy deposit (*Phase 1* of ignition as distinguished in Sec. 5.1) to the anchoring of the flame at the injector nozzle (**Phase 2**) in highly swirled confined environment. The design is inspired from test rigs reported in the literature: the partially-premixed burner from TU Darmstadt (Janus *et al.*, 2005), the PRECCINSTA burner installed at DLR (Weigand *et al.*, 2006) and the two-phase flow MERCATO burner experimented at ONERA (Garcia-Rosa *et al.*, 2011; Linassier, 2012). The major constraints of the design are the large optical access required to track the flame position during the whole ignition sequence, the capability to change the swirl intensity and the operability in both premixed and partially premixed modes. The last two features aim to quantify the effect of swirl and partial premixing on the ignition performance of the burner and have direct implications on the design of industrial injection systems.

Figure 6.1 is a picture of the burner illustrating its four major components, from bottom to top:

- A plenum is located upstream of the injection system to lower the turbulence of the flow generated in the feeding lines and a grid placed in the lower part helps to destroy the large structures.
- The swirl injection system is close to the one designed by Janus *et al.* (2005), the latter being inspired from the aeronautical industry. A radial swirler composed of 18 vanes inclined at 45° and followed by a convergent annular section acts as the main air (or premixed mixture) admission (see Fig. 6.2). The convergent annular section ends at the combustion chamber inlet with an outer diameter $D_{ext} = 20$ mm and an inner diameter $D_{int} = 9$ mm. The fuel injector tube of diameter $d = 4$ mm is nested in the air admission and enters the combustion chamber in the same plane as the first admissions.
- The combustion chamber is a square of 100 mm length by 260 mm height. Large optical accesses on three sides of the combustor enable to use non-intrusive optical diagnostics, direct visualization of the flame and ignition by laser induced breakdown.
- At the top, a convergent exhaust forces closure of the inner recirculation zone. The convergent also increases the pressure rise during the ignition sequence, which allows to use the pressure evolution as an indicator of the ignition progress.

The experimental facility is operated in ambient conditions and the fuel used is methane. Two operating modes are studied experimentally:

- The premixed case where the central tube and the plenum are fed with premixed flow is studied in the work of Barré (2014) but will also be used in this work to evaluate the performance of the ignition model (Chap. 8)

Figure 6.1: Picture of the KIAI single injector experimental test bench.

- The non-premixed case where the central tube is fed with pure methane and the plenum with air. This configuration is investigated here in LES.

The operating conditions of both mode are listed in Tab. 6.1.

	$\dot{m}_{tube}$ [g/s]	$\dot{m}_{plenum}$ [g/s]	Global ϕ_g	T [K]	P [Atm]
Premixed	0.236	5.612	0.75	298	1.0
Non-premixed	0.234	5.43	0.75	298	1.0

Table 6.1: Operating conditions studied experimentally in the KIAI single burner.

Stereo-Particle Image Velocimetry (SPIV) and Planar Laser-Induced Fluorescence (PLIF) measurements are used to characterize the initial cold flow field and fuel mixing. The experimental data are based on 1000 instantaneous measurements. High speed OH* emission recording is used to track the flame during ignition as well as a pressure sensor in the combustion chamber. More details on the experimental facility and diagnostic technics can be found in the work of Cordier (2013).

6.2 Numerical set-up

6.2.1 Computational domain

The computational domain includes the four components of the experimental test rig, as reported in Fig. 6.2. The grid placed in the plenum of the test rig is not included in the numerical domain but replaced by a laminar air injection at the inlet of the plenum. The axial direction is referred to as the z-axis, corresponding to the main flow direction, while the x-axis and y-axis denote the transverse directions. Space dimensions are non-dimensionalized by D_{ext}, where $D_{ext} = 20$ is the outer diameter of the swirler passages.

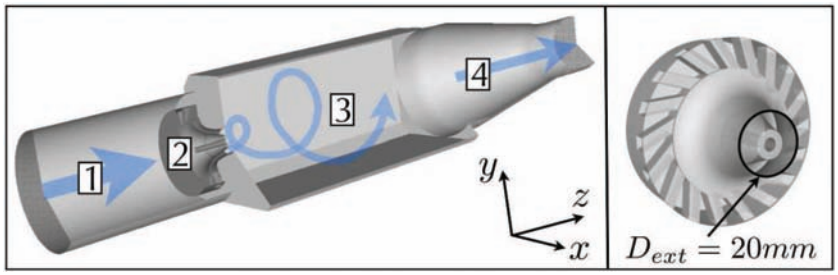

Figure 6.2: Computational domain and injection system details. Main components are: 1. Plenum, 2. Injection system, 3. Combustion chamber, 4. Convergent exit.

In order to evaluate the dependence to the numerical set-up, three meshes have been generated and their main characteristics are listed in Tab. 6.2. The first two meshes are composed of tetrahedral elements only, with a significant reduction of the characteristic size in the convergent section and at the vicinity of the methane jet for *MeshT31M* compared to *MeshT09M* (see Fig. 6.3). A hybrid mesh *MeshP12M* with a layer of prisms on the injection system walls enables to strongly reduce the y^+ in the swirler and in the convergent while keeping the overall mesh size reasonable since the grid size in the rest of the domain is similar to *MeshT09M*. This hybrid mesh is used to evaluate the effect of the mesh resolution of the pressure drop.

	Nb. elements [M]	Nb. vertices [M]	V_{min} [m^3]	Swirler $\overline{y^+}$
MeshT09M	9.1	1.63	$6.835\,e^{-13}$	~ 60
MeshT31M	31.1	5.64	$1.85\,e^{-14}$	~ 25
MeshP12M	11.7	2.19	$1.62\,e^{-13}$	~ 8

Table 6.2: Characteristics of meshes used to study non-reacting flow.

6.2.2 Numerical parameters

LES are performed with AVBP and unless specified otherwise, the numerical parameters of the solver are listed in Table 6.3. In addition, to assess the accuracy of the numerical results, results obtained with YALES2, a low Mach number LES solver developed at CORIA (Moureau *et al.*,

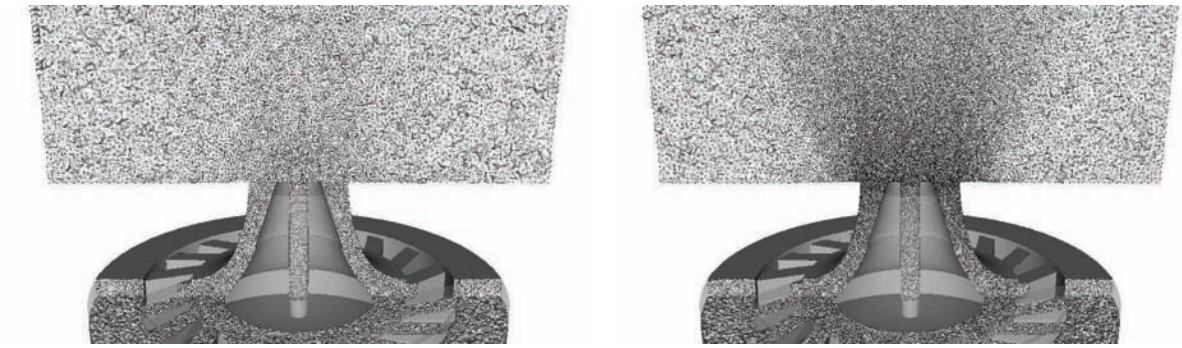

Mesh09M *Mesh31M*

Figure 6.3: Slices in the computational domain for *Mesh09M* and *Mesh31M* illustrating the mesh difference in refinement.

2011*a*) are also reported. Unless specified otherwise, YALES2 simulations are performed using the same LES modeling as for AVBP in Table 6.3. WALE subgrid model with adiabatic non-slipping walls. Numerics in YALES2, however, strongly differs from AVBP: a 4^{th}-order finite-volume scheme for the spatial resolution and the TVF4A 4^{th}-order explicit time integration (Kraushaar, 2011) are used with a Deflated PCG method for the Poisson solver (Nicolaides, 1987).

	Numerical Parameters
Convection scheme	TTGC: $\mathcal{O}(3)$ in space & time (Colin & Rudgyard, 2000)
Diffusion scheme	2Δ operator
SGS model	WALE (Nicoud & Ducros, 1999)
Artif. viscosity	Colin model: $\epsilon^{(2)} = 0.01$, $\epsilon^{(4)} = 0.005$
	Boundary conditions
CH_4 inlet	NSCBC (Poinsot & Lele, 1992) (velocity, 10% turbulence)
Air inlet	NSCBC (Poinsot & Lele, 1992) (velocity)
Walls	Adiabatic non-slipping walls

Table 6.3: Numerical parameters for AVBP.

	Numerical Parameters
Convection scheme	$\mathcal{O}(4)$ finite volume in space & $\mathcal{O}(4)$ TVF4A time integration
Diffusion	implicit
Poisson solver	DPCG (Nicolaides, 1987)
SGS model	WALE (Nicoud & Ducros, 1999)
	Boundary conditions
CH_4 inlet	Dirichlet (velocity, 10% turbulence)
Air inlet	Dirichlet (velocity)
Outlet	Dirichlet (pressure)
Walls	Adiabatic non-slipping walls

Table 6.4: Numerical parameters for YALES2.

Note that, in both code, turbulence is injected through the CH_4 inlet corresponding to 10% of the bulk velocity in order to mimic turbulence induced by the feeding line shape.

6.3 Non-reacting flow characteristics

6.3.1 Flow characteristics

Prior to present the results of the numerical simulations, the main flow characteristics are introduced:

- the convective time scale is evaluated from the volume in the combustion chamber V_c and the inlet flow rate $\dot{m}$:

$$\tau_{conv} = \frac{\rho V_c}{\dot{m}} = 0.73\ s \tag{6.1}$$

- the rotation time scale is evaluated at the combustion chamber inlet:

$$\tau_{rot} = \frac{\pi R_i}{u_{\theta,i}} = 0.81\ ms \tag{6.2}$$

  where R_i is the mean radius of the convergent inlet and u_θ is the mean azimuthal velocity component in the inlet plane.

- the Reynolds number is evaluated at the combustion chamber inlet:

$$Re = \frac{|\vec{u}|_i D_i}{\nu} = 21000 \tag{6.3}$$

  where $|\vec{u}|_i$ is the norm of the velocity vector in the inlet plane, D_i is the mean diameter of the convergent inlet and ν is the kinematic viscosity.

6.3.2 Flow pattern

Figure 6.4 shows time-averaged streamlines in a central x-normal plane (left) and a z-normal plane (right). The flow pattern is typical of highly swirled configurations: the swirled jet (SWJ) issued from the swirler generates a reverse flow region along the axis of the burner referred to as Inner Recirculation Zone (IRZ). The presence of the IRZ is due to an axial adverse pressure gradient. Indeed, the strong rotation of the incoming flow results in centrifugal forces that are compensated by a radial pressure gradient. As the SWJ expands in the combustion chamber, the conservation of circulation implies a decay of the azimuthal velocity, hence a decay of the radial pressure gradient (Billant *et al.*, 1998). If the axial pressure gradient is strong enough, a bifurcation called vortex breakdown occurs (Lucca-Negro & O'Doherty, 2001), characterized by a reverse flow region nested in the SWJ.

The onset of vortex breakdown is generally related to the Swirl number S_w (Beer & Chigier, 1983; Billant *et al.*, 1998). There are several definitions of the swirl number in the literature,

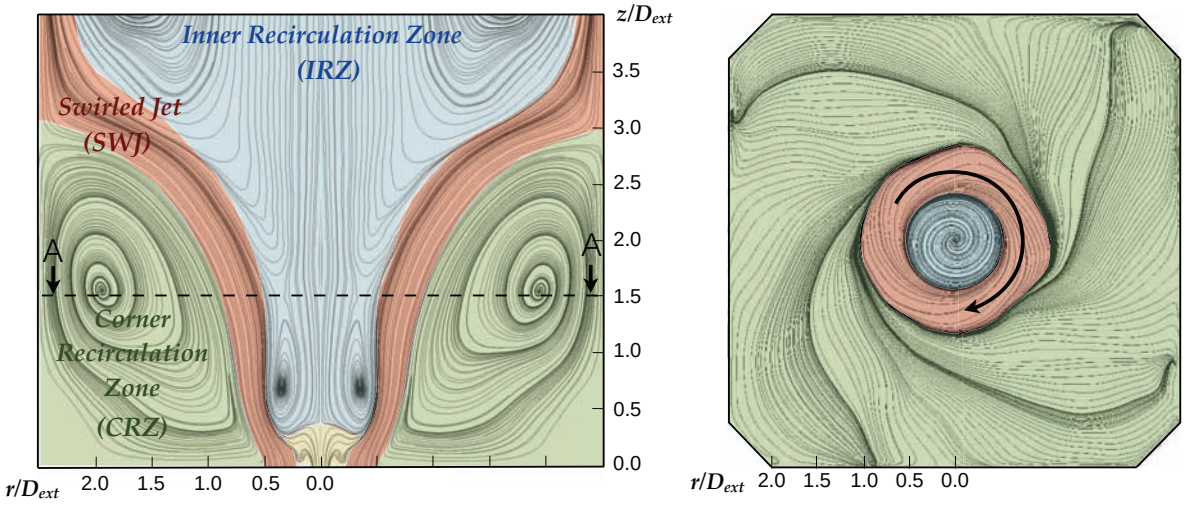

Figure 6.4: Time-averaged streamlines in a central x-normal plane (left) and the A-A z-normal plane (right). The main flow regions are identified: Swirled Jet (SWJ), Inner Recirculation Zone (IRZ) and Corner Recirculation Zone (CRZ).

including or not the axial momentum due to the pressure gradient or the velocity fluctuations. A complete derivation of the Swirl number can be found in Palies (2010) along with a brief overview of the various relations found in the literature. To define S_w, it is convenient to introduce a cylindrical referential (r,θ,z) whose z-axis is aligned with the z-axis of the cartesian referential presented in Fig. 6.2. Following the definition of Ivanic *et al.* (2003), S_w writes:

$$S_w = \frac{G_\theta}{R_{ext} G_z} = \frac{\int_0^{R_{ext}} \rho u_z u_\theta 2\pi r^2 dr}{R_{ext} \int_0^{R_{ext}} \rho u_z^2 2\pi r dr} \tag{6.4}$$

where G_θ is the flux of azimuthal momentum, G_z is the flux of axial momentum, $R_{ext} = D_{ext}/2$ is the outer radius of injection and u_θ and u_z are the azimuthal and axial velocity components respectively. Note that S_w is the result of an integral in a given z-normal plane and theoretically independent of the z position but its value decreases as progressing downstream of the injection plane due to dissipation. The swirl number in the LES simulation is evaluated in the injection plane ($z = 0.0$) of the combustion chamber at 0.81, close to the experimental value reported in Cordier *et al.* (2013*a*) ($S_{exp} = 0.76$). Billant *et al.* (1998) derives a critical theoretical value S_c above which vortex breakdown occurs, based on assumption that the incoming flow velocity profile is that of a Rankine vortex: $S_c = 0.707$. This value is evaluated against experimental measurements and is found to agree in several configurations (Billant *et al.*, 1998; Liang & Maxworthy, 2005). The value find in both experiments and LES is above $S_{w,c}$, in agreement with the flow pattern observed in the LES. The IRZ is closed downstream due to the presence of the convergent exhaust. In confined environment, the SWJ also induces recirculation on its outer part, referred to as Corner Recirculation Zones (CRZ), closed at $z/D_{ext} = 3$. At the bottom of Fig. 6.4(left), the flow coming from the methane injection meets with the air back flow of the IRZ. At the meeting point, the zero axial velocity location is called the stagnation point. Its axial location results from the equilibrium between the momentums of the methane jet and the IRZ flow. Finally, strong shear layers are located at the interfaces between the SWJ and both IRZ

and CRZ.

6.3.3 Mean flow velocity

Figure 6.5 shows time-averaged mean and RMS fields of the velocity components in the central x-normal plane. Data are recorded during 150 ms in order to obtain converged statistics and the mean and RMS of a quantity ψ are evaluated respectively by:

$$\langle\psi(\vec{x})\rangle = \frac{1}{T_m}\sum_{n=1}^{N_T}\psi(\vec{x},t^n)\Delta t_m \tag{6.5}$$

$$\psi(\vec{x})_{RMS} = \sqrt{\langle\psi(\vec{x})^2\rangle - \langle\psi(\vec{x})\rangle^2} \tag{6.6}$$

where T_m is the recording duration, N_T is the total number of instantaneous snapshots and Δt_m is the time delay between two consecutive snapshots. Note that this definition corresponds to a Reynolds average so that the density difference between methane and air is not taken into account. Moreover, the RMS value does not account for the subgrid scale contribution.

The high velocity of the SWJ is clearly visible on the axial velocity component. The jet opening is first limited resulting in a arrow IRZ while further downstream the SWJ is fully opened. Such IRZ shape called *bottle-neck* is also observed in the MERCATO test rig. The highest axial velocity is located in the methane jet and very rapidly decreases near the stagnation point. It is interesting to note that the time-averaged position of the IRZ goes up to the wall between the methane jet and the SWJ. The high swirl number of the injection system is demonstrated by the tangential velocity component with $u_{x,max} \sim u_{\theta,max}$ at the injection plane. The RMS field of the axial component shows the strong turbulence intensity at the vicinity of the stagnation point and the inner shear layer. The other two components illustrate the flapping motion of the methane jet with high turbulence along the wall between the methane jet and the SWJ: as the axial velocity quickly decreases near the stagnation point, the conservation of the mass flow rate implies a rapid increase of the radial component.

LES results are compared with experiments using time-averaged statistics profiles. Figures 6.6 & 6.7 show the first two statistical moments of the three components of velocity at five axial positions downstream of the injection system: $z/D_{ext} = 0.25, 0.5, 1, 1.5, 2$ (see bottom left cut inFig. 6.5). For the sake of clarity, only the results for *MeshT09M* and *MeshT31M* using AVBP are reported. The results obtained with *MeshP12M* are very similar to those of *MeshT09M*. The velocity profiles show that the velocity field is in good agreement with experiments past the first profile at $z/D_{ext} = 0.25$. The LES is able to accurately capture the jet opening angle and the velocity components. The fluctuations are lightly over-predicted but fully recovered downstream. The large differences observed at $z/D_{ext} = 0.25$ denote the slightly too strong penetration of the methane jet: an offset in the jet penetration is found compared with experiments, which greatly modifies the velocity profile since the mean field has a strong gradient in the stagnation point region. Note that the increase in mesh resolution from *MeshT09M* to *MeshT31M* is able to significantly improve the jet penetration prediction but the position of the stagnation point is not fully recovered in LES.

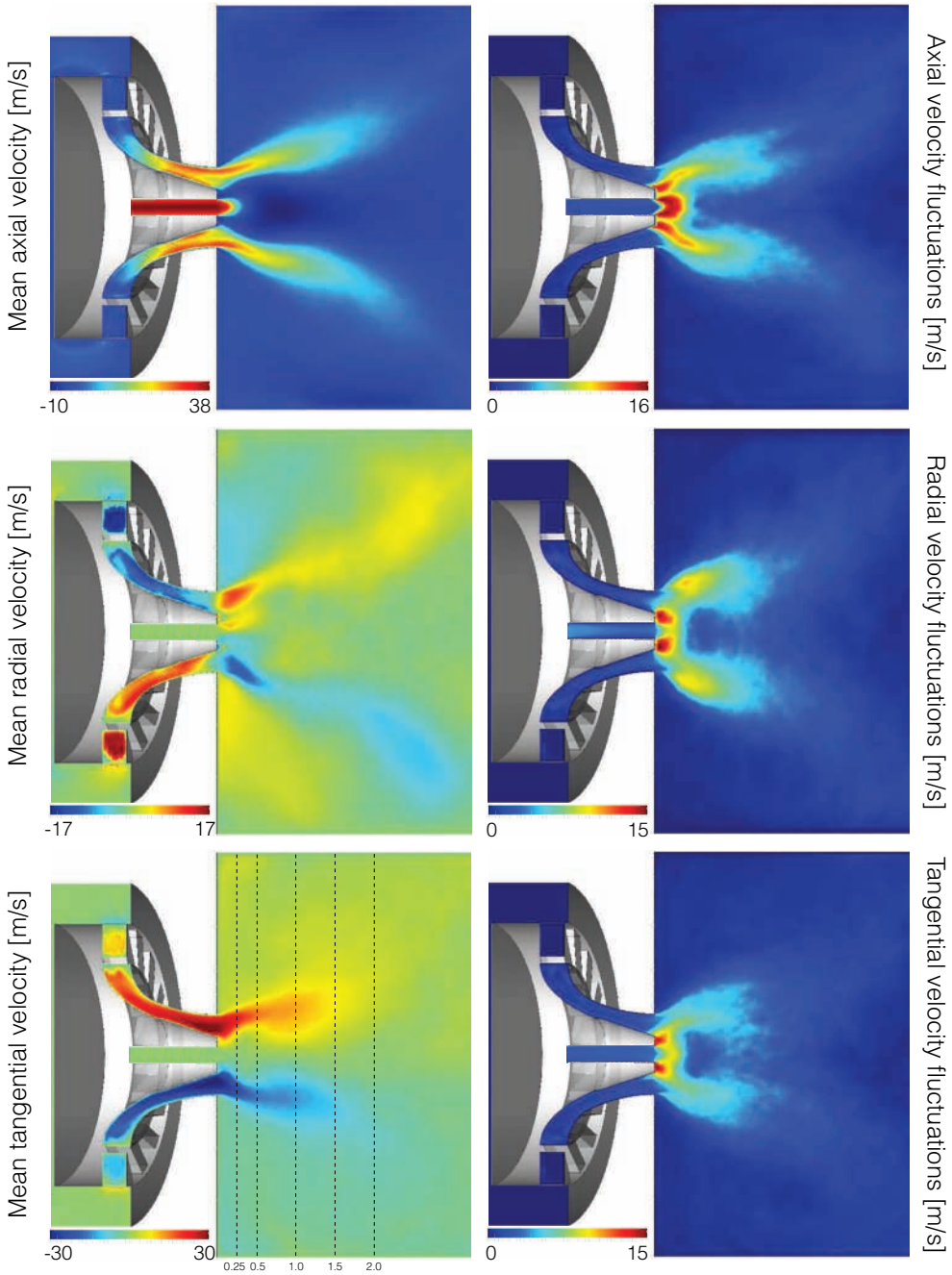

Figure 6.5: Mean and RMS velocity components in a central x-cut plane through the combustion chamber on *Mesh31M* with AVBP.

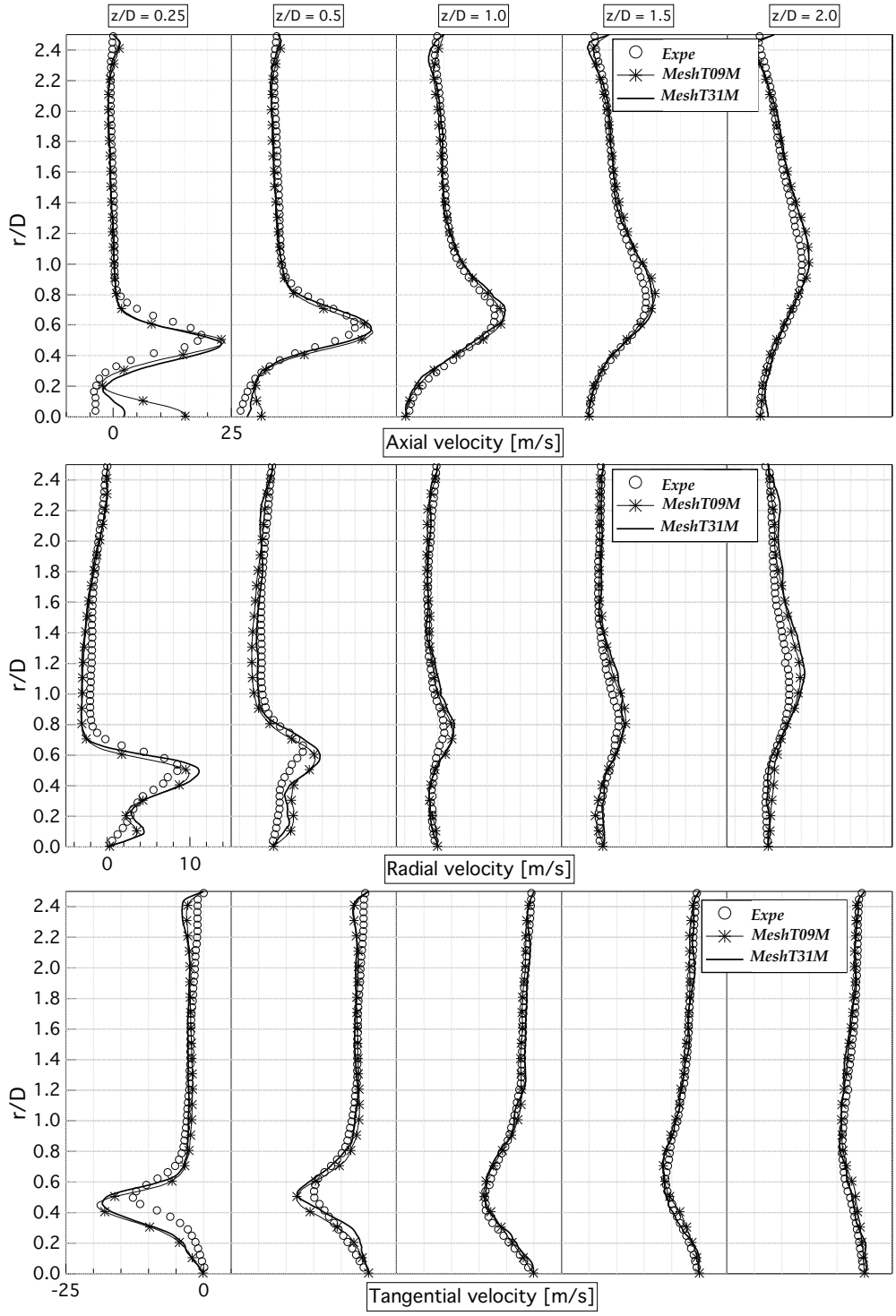

Figure 6.6: LES versus experiments: mean velocity components profiles obtained with AVBP at 5 axial positions $z/D_{ext} = 0.25, 0.5, 1, 1.5, 2$.

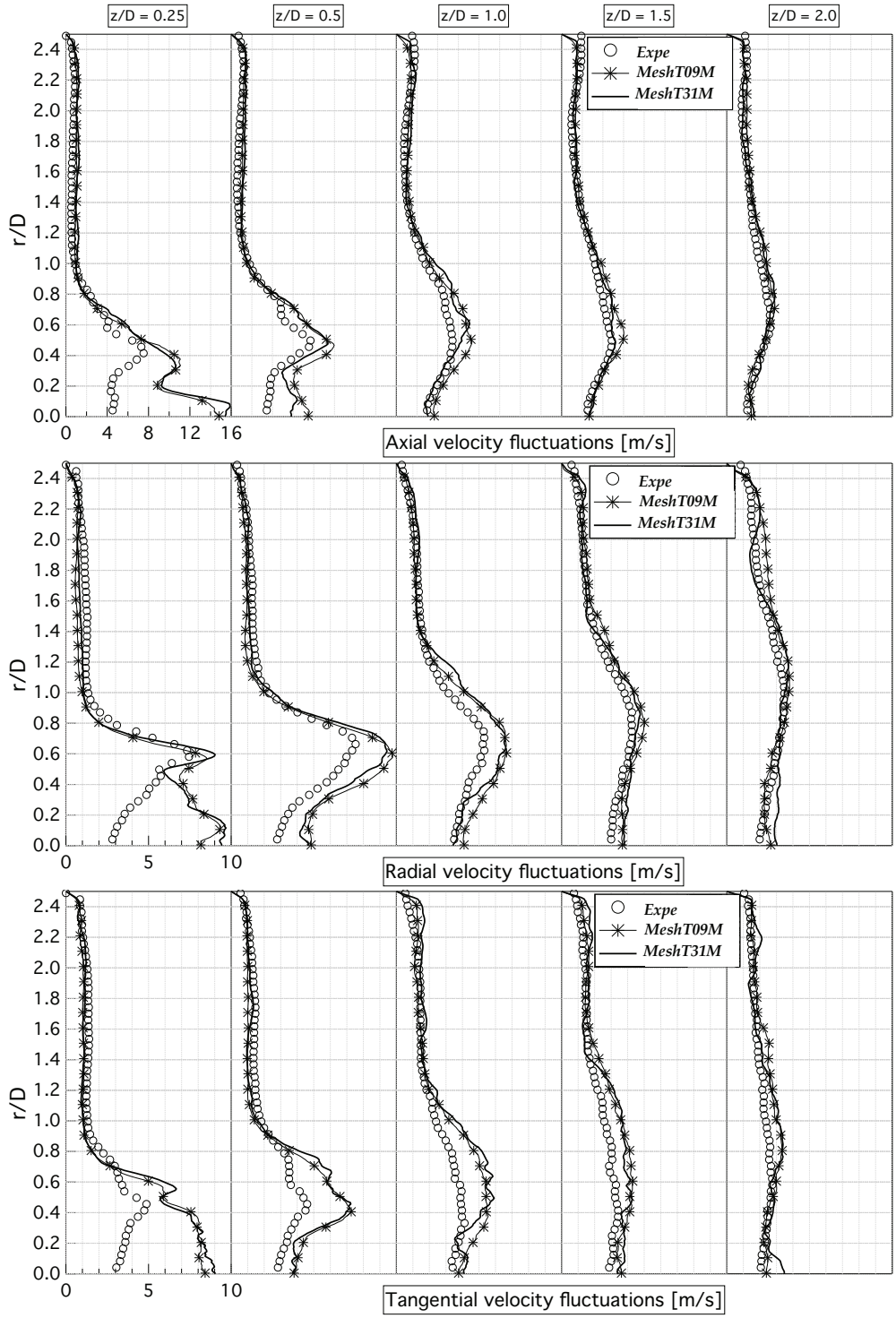

Figure 6.7: LES versus experiments: RMS velocity profiles obtained with AVBP at 5 axial positions $z/D_{ext} = 0.25, 0.5, 1, 1.5, 2$.

In Tab. 6.5, the methane jet penetration is taken as an indicator to compare the LES performed varying the physical and numerical parameters. Changing the subgrid stresses model from WALE to SIGMA keeping non-slipping walls or Smagorinsky in combination with a law-of-the-wall on *MeshT09M* results in a greater offset with the experimental position of the stagnation point ($z_{jet}/D_{ext} = 0.18$) . The results are also worse when using LW rather than TTGC. The results obtained with *MeshP12M* are fairly similar to those of *MeshT09M* and shows that the change in jet penetration is not controlled by the resolution of the boundary layer in the swirler or the convergent section. The most accurate results are obtained with *MeshT31M* when using the baseline numerical set-up. The same conclusion can be drawn with YALES2. Note that a very fine mesh containing 70 millions of cells has been tested with no significant improvement of the jet penetration.

Solver	Models	Num. scheme	Mesh	z_{jet}/D_{ext}
AVBP	*SMAGO/Wall-law*	TTGC	*MeshT09M*	0.501
	SIGMA/No-slip	TTGC	*MeshT09M*	0.421
	WALE/No-slip	LW	*MeshT09M*	0.428
		TTGC	*MeshT09M*	0.418
			MeshT31M	**0.285**
			MeshP12M	0.402
YALES2	*WALE/No-slip*	4^{th}-order FV	*MeshT09M*	0.388
			MeshT31M	0.292
			MeshP12M	0.378

Table 6.5: Numerical predictions of the methane jet penetration z_{jet}/D_{ext} measured as the position of the zero z-axis component of velocity along the injector axis. (Expe: $z_{jet}/D_{ext} = 0.18$).

The axial velocity profile along the central axis of the burner is shown in Fig. 6.8 for AVBP and YALES2 simulations on *MeshT31M*: both codes are in good agreement, but the stagnation point exhibits an offset of about 2 mm with experiments.

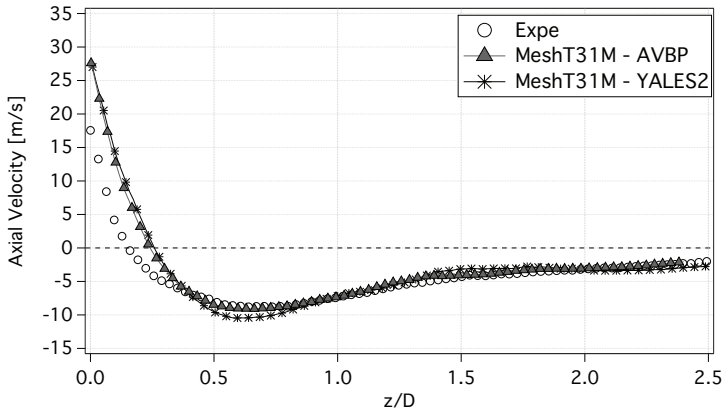

Figure 6.8: LES on *MeshT31M* versus experiments: velocity components fluctuations profiles at 5 axial positions $z/D_{ext} = 0.25, 0.5, 1, 1.5, 2$.

6.3.4 Mean mixture fraction

For a similar mass flow rate, the Reynolds number of swirling flows is increased compared to non-swirling flows due to the additional azimuthal velocity component. Hence, strongly swirled flows generally show very good mixing capabilities since the turbulent mixing is increased. The mean and RMS mixture fraction fields shown in Fig. 6.9 illustrate the good mixing properties of the current design: most of the combustion chamber is filled with a mixture close to the global equivalence ratio ($\phi_g = 0.75$, corresponds to $z_g = 0.042$), the pure methane injected through the central jet does not penetrate far downstream in the chamber.

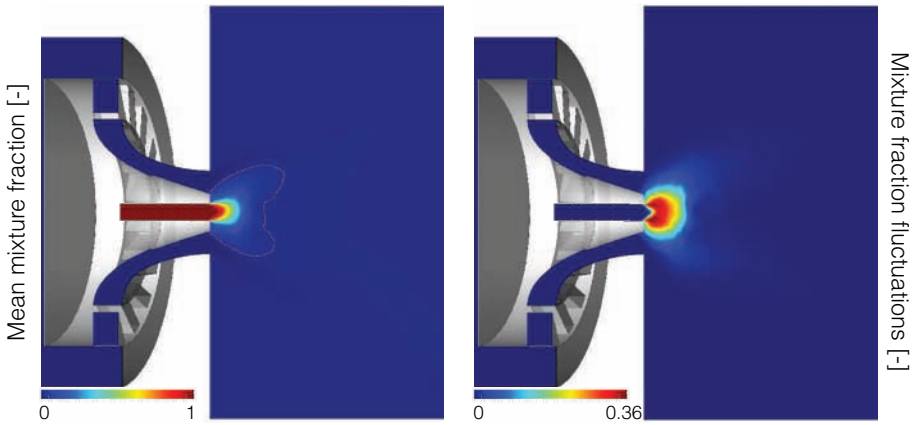

Figure 6.9: Mean and RMS mixture fraction in a central x-cut plane through the combustion chamber. The iso-line $z_{st} = 0.055$ is shown in white.

Once again, the mixture fraction mean and RMS profiles displayed in Fig. 6.10 & Fig. 6.11 are compared with experimental results at 4 axial positions $z/D_{ext} = 0.3, 0.5, 0.9, 1.1$ (different from the position used for the velocity profiles). Only results obtained with AVBP on *Mesh31M* are presented. The dotted-dashed lines indicate the positions of the lower and upper flammability limits. The inaccurate penetration of the methane jet greatly modifies the two statistical moments of the mixture fraction distribution on the first profile.

6.3.5 Pressure drop

The pressure drop through complex geometries, such as swirled injection systems, is a key design parameter since it has a direct influence on the engine efficiency (Nicholas, 2005). However, the prediction of the pressure drop is not an easy task to achieve using LES and numerous parameters of the computation affect the results (Kraushaar, 2011; Barré *et al.*, 2013). The pressure drop is the results both of singular losses due to geometrical changes and linear losses due to friction at the walls. The pressure drop can be evaluated from the conservation of total energy between two planes located upstream and downstream of the injection system. In the following, the pressure drop is simply defined as the total pressure difference between point A located upstream and point B located downstream of the injection system as shown in Fig. 6.12.

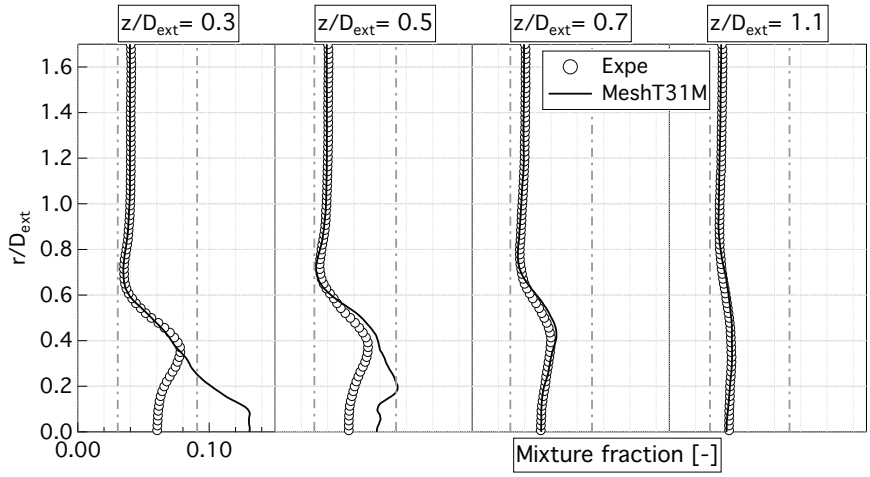

Figure 6.10: LES versus experiments: mixture fraction profiles at 4 axial positions $z/D_{ext} = 0.3, 0.5, 0.7, 1.1$.

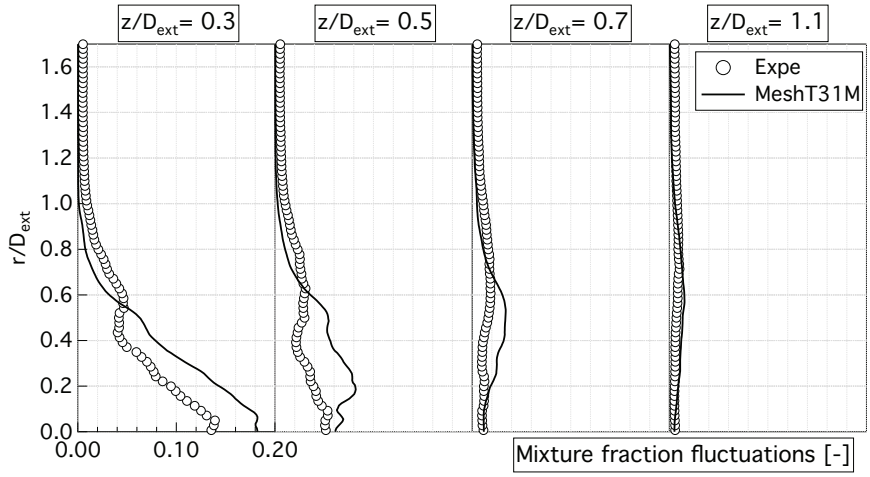

Figure 6.11: LES versus experiments: mixture fraction fluctuations profiles at 4 axial positions $z/D_{ext} = 0.3, 0.5, 0.7, 1.1$.

Using time-averaged LES results:

$$\Delta P = \overline{P}_{tot,up} - \overline{P}_{tot,down} \tag{6.7}$$

with

$$\overline{P}_{tot} = \overline{P} + \frac{1}{2}\overline{\rho}(\widetilde{u}^2 + \widetilde{v}^2 + \widetilde{w}^2) \tag{6.8}$$

where $\overline{P}$ is the filtered static pressure. The pressure drops measured experimentally is $\Delta P_{exp} = 593Pa$. The pressure drops measured in LES for all numerical set-ups investigated in this study

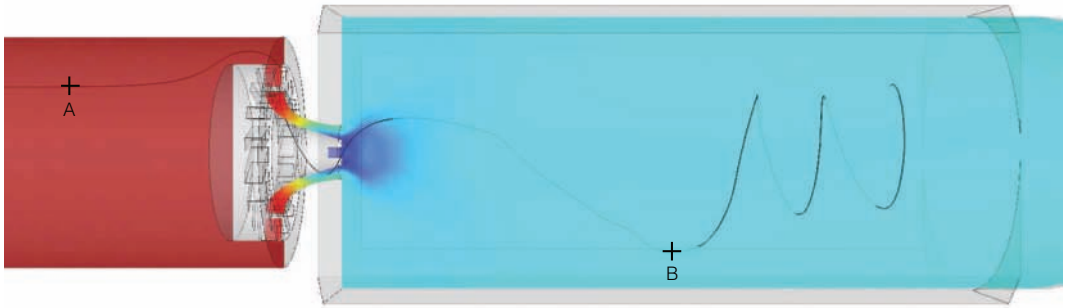

Figure 6.12: Position of point A and point B along a streamline for the evaluation of the pressure drop. The central cut plane is colored by the mean static pressure P.

are summarized in Table 6.6. From the AVBP simulations, the pressure drop is found to be strongly reduced when increasing the mesh resolution. The best prediction is obtained using TTGC and *MeshT31M*, with less than a 3.2% offset as compared to experiments. On the coarse mesh, the best predictions are obtained using *SMAGO/Wall-law* combination rather than *WALE/No-slip*, which is coherent with the observations of Barré *et al.* (2013). The prediction obtained with *MeshP12M* are very similar to the results obtained with *MeshT31M*, showing that the smaller $\overline{y^+}$ does not improve pressure drop predictions. The effect of the mesh resolution on the prediction is also reproduced in YALES2, but the prediction are higher than those obtained with AVBP.

Solver	Models	Num. scheme	Mesh	Pressure drop $[Pa]$
AVBP	*SMAGO/Wall-law*	TTGC	*MeshT09M*	700
	SIGMA/No-slip	TTGC	*MeshT09M*	764
	WALE/No-slip	LW	*MeshT09M*	790
		TTGC	*MeshT09M*	775
			MeshT31M	**612**
			MeshP12M	614
YALES2	*WALE/No-slip*	4^{th}-order FV	*MeshT09M*	821
			MeshT31M	785
			MeshP12M	692

Table 6.6: Numerical prediction of pressure drop $[Pa]$ ($\Delta_{P,exp} = 593[Pa]$).

6.3.6 Flow instability

Swirled flows at super-critical swirl number ($S_w > S_{w,c} = 0.707$) are prone to hydrodynamic instabilities due to the ability of the perturbation to propagates upstream through recirculation zones (Liang & Maxworthy, 2005). Axial and azimuthal instabilities arise in the shear layers in the form of a precessing vortex core (PVC) (Ruith *et al.*, 2003; Roux *et al.*, 2005). In the present LES, the PVC is a large scale coherent structure evolving in the inner shear layer between the SWJ and the IRZ. A less intense counter-part is found in the outer shear layer between SWJ and the CRZ. The PVC as shown in Fig. 6.13 is tracked by an iso-surface of low static pressure and

colored by the radial gradient of axial velocity to differentiate the inner (grey) and outer (white) shear layer structures. In the present case, the PVC has a two branches structure in the inner shear layer with a helical shape. Figure 6.13(a) indicates the sign convention: the flow has a clockwise rotation, considered as positive. Following this convention, the PVC helical structure is winded in a negative direction around the axis of the swirler, but is rotating in the positive direction. The PVCs captured in Roux *et al.* (2005) or García-Villalba *et al.* (2006) have similar winding and rotation orientation, although theory is not yet able to predict which unstable mode will dominate the flow. The outer shear layer vortices do not show a clear helical shape, but they are placed in symmetrical arrangement with the inner one around the SWJ region.

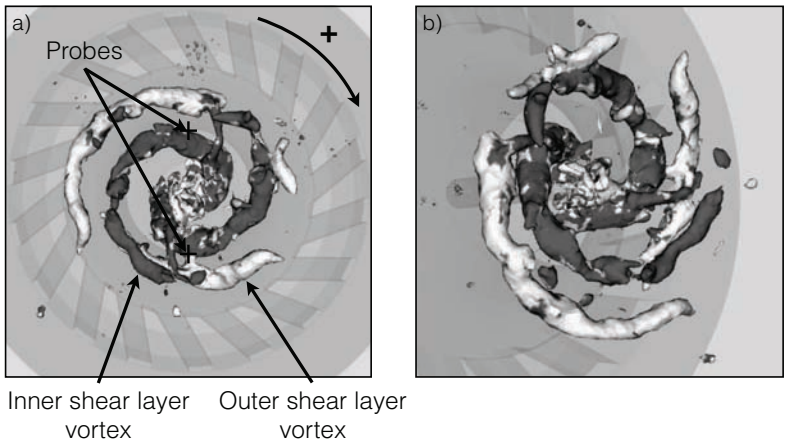

Figure 6.13: Precessing Vortex Core in a z-axis top view (a) and perspective (b). Vortices are colored by the radial gradient of axial velocity: positive regions in grey (inner shear layer) and negative regions in white (outer shear layer).

Figure 6.14 plots the cross spectra of two diametrically opposed probes ($x/D_{ext} = \pm 0.5$, $z/D_{ext} = 0.5$ see Fig. 6.13(left)) time series and shows a clear indication of a periodic oscillation having a similar influence on pressure (a), z-velocity component (b) and mixture fraction (c). The peak activity at 1150 Hz is accompanied by two smaller intensity frequencies at about 575 Hz and 1725 Hz. The experiments reported in Cordier (2013) use a temporally resolved diagnostic (Doppler Laser Anemometry (DLA)) to capture the PVC frequency on the velocity fields. The present case is not investigated, but a perfectly premixed case with the same geometry shows activity at 507 Hz and 999 Hz. The Strouhal number of the perturbation can be evaluated:

$$St = \frac{D_{ext} f}{|\boldsymbol{u}|_{inlet}} \tag{6.9}$$

where f is the frequency of the instability and $|\boldsymbol{u}|_{inlet}$ the norm of the velocity at the combustion chamber inlet. $St = 0.72$ is found using the frequency of the most energetic perturbation which is coherent with the experimental observations reviewed in Syred (2006) and the characteristics of PVC.

The coherence between pressure, velocity and mixture fraction signals indicates that the PVC of the inner shear layer (starting between the methane jet and the SWJ) traps rich mixture

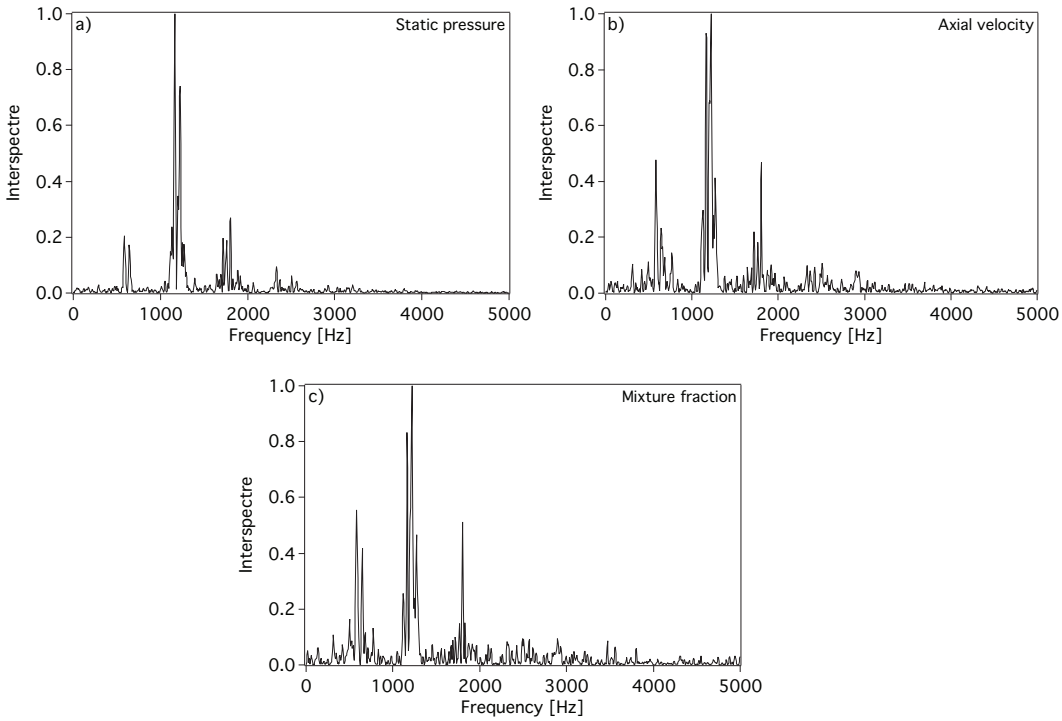

Figure 6.14: 2-points cross spectra of static pressure (a), streamwise velocity (b) and mixture fraction (c) of probes located in the inner shear layer.

in its core. Figure 6.15 shows instantaneous pressure distribution in a central x-normal plane. The white iso-contour indicates the position of the rich flammability limit mixture fraction ($z_{rich} = 0.089$). The contour is wrapped by the PVC, tracked here by low-pressure regions. This mechanism has also been observed experimentally by Cordier (2013) and by Cheng *et al.* (2012) in a close configuration. On the contrary, pockets of lean mixture are also found in the outer shear layer (between the SWJ and the CRZ) due to the presence of the PVC.

6.4 Conclusion

Simulations of the non-reacting flow in the KIAI single burner have been performed and the two main objectives set out in introduction can be summarized as follows:

- LES is found to be mainly sensitive to the mesh resolution and to a lesser extend to the LES subgrid and wall modeling. Comparison with experiments shows that the best numerical set-up gives satisfactory results, allowing to now investigate ignition sequences. The close vicinity of the methane injection is not well reproduced and several leads have been investigated without significant improvement of the LES predictions. In the following, numerical simulations of ignition will be performed on a grid having the same properties as *MeshT31M*.

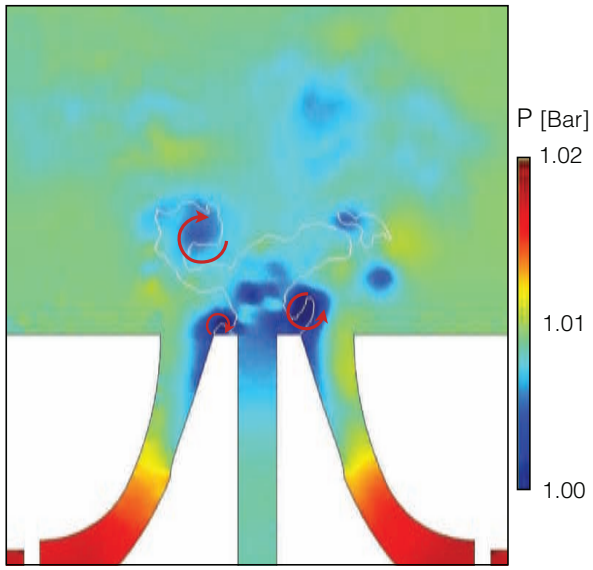

Figure 6.15: Pressure field in a central x-cut plane. $z_{rich} = 0.089$ iso-contour is reported in white.

- LES reveals a flow pattern typical of highly swirled configurations similar to experimental observations. The recirculation zones are expected to play an important role during the ignition process. The partial premixing generates a rich zone at the bottom of the IRZ and a lean zone at the beginning of the SWJ region while the downstream of the combustion chamber is fully premixed. A coherent structure is observed in both the inner and outer shear layers resulting in periodic perturbation of the local mixture fraction and velocity fields. No evidence of correlation between the PVC and the ignition success or failure has been reported in the literature but it is at least expected to affect the kernel trajectory.

Chapter 7

Ignition of the KIAI single burner

Contents

Over the last 5 years, several LES studies of ignition sequences in simple burner configurations (Lacaze *et al.*, 2009*b*; Triantafyllidis *et al.*, 2009; Subramanian *et al.*, 2010; Jones & Prasad, 2011) have demonstrated the capacity of the LES approach to investigate ignition in complex configurations and shed some light on flame propagation mechanisms following energy deposit. However, these studies suffer from two main limitations:

- they are limited to free jet or bluff-body configurations with low velocity fluctuations, far from highly swirled conditions as encountered in realistic gas turbines.
- the small number of LES of ignition sequences performed does not allow to study the stochastic character of ignition.

Barré (2014) was the first to numerically investigate the configuration of Cordier (2013), in premixed mode. Several ignition sequences were computed and the effect of the numerical parameters on the ignition outcome was highlighted. In particular, Barré (2014) recommended to use

well resolved LES to minimize the effect of the model for flame/turbulence interactions on the flame/kernel interactions.

The objectives of the present study are multiple:

- Perform multiple LES of ignition sequences and evaluate the capability of LES to reproduce the ignition scenarios and statistics observed in the experiment.
- Investigate the growth of flame kernels in a highly turbulent partially premixed environment.
- Identify the mechanisms leading to quenching of the flame kernel by a systematic analysis of multiple LES.
- Use LES of full ignition sequences to directly predict ignition probability.

Part of the results presented in this Chapter has been published in Esclapez *et al.* (2015):

Esclapez L., Riber E. & Cuenot B. 2015. Ignition probability of a partially premixed burner using LES. *Proceedings of the Combustion Institute* **35** (3), 3133-3141.

7.1 Experimental results

Focusing on the ignition of a single burner, the experimental study conducted by Cordier (2013) had two main objectives:

- investigate the ignition performance of the burner by constructing ignition probability maps for two swirl number values both in premixed and non-premixed modes. In combination with measurements on the non-reacting flow field, ignition maps provide a better understanding of the relation between local or global properties and ignition capabilities.
- build ignition scenarios depending on the ignition location and analyze ignition sequences using the non-reacting flow pattern.

To achieve the first objective, a small zone of the combustion chamber near the methane jet is selected. A cartesian 2D grid is drawn in the combustion chamber central cut plane and 50 ignition tries are performed at each grid point. The 2D grid is composed of 88 points so that the total number of ignition sequences captured experimentally is 4400. The experimental ignition probability $P_{ign,XP}$ is computed as the number of successful ignition sequences over the total number of trials. The uncertainty on the ignition probability is evaluated by the standard deviation:

$$\sigma = \left(\frac{P_{ign,XP}(1 - P_{ign,XP})}{N} \right)^{1/2} \tag{7.1}$$

where N is the number of trials. Using 50 trials, the uncertainty is maximum for $P_{ign,XP} = 0.50$ and equal to 7 %. The ignition probability map of the operating point studied in this work

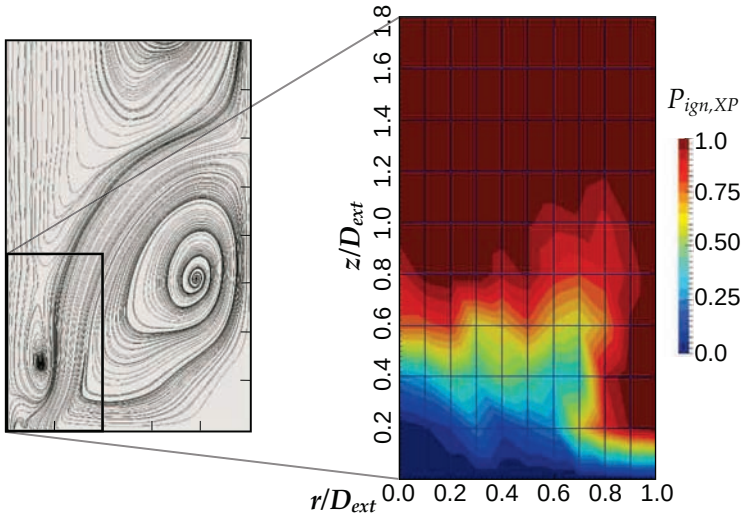

Figure 7.1: Experimental ignition probability map extracted from Cordier (2013).

is presented in Fig. 7.1: the region of interest extends from ($r/D_{ext} = 0.0$; $z/D_{ext} = 0.0$) to ($r/D_{ext} = 1.0$; $z/D_{ext} = 1.8$).

Note that the value $P_{ign,XP} = 0$ on the line $z/D_{ext} = 0$ denotes the lack of experimental data due to the vicinity of the chamber wall. Along the burner z-axis, $P_{ign,XP}$ is found to go from zero near the methane jet to one in the downstream region with a steep gradient around $z/D_{ext} = 0.5$. A large region in the top half of the domain exhibits a maximum probability $P_{ign,XP} = 1$, but the region of $P_{ign,XP} < 1$ extends downstream along the position of the SWJ (at $r/D_{ext} = 0.7$). Cordier (2013) also reported comparisons of the ignition probability with the local turbulence intensity and flammability factor and showed no direct correlation between the pointwise non-reacting flow characteristics and the ignition probability. Ignition scenarios were constructed from high speed OH* recordings. The knowledge of both the flame kernel motion and flame expansion allows to evaluate the path and mechanisms leading to either ignition success or failure. Figure 7.2 shows an example of ignition sequence with sparking at a downstream location in the IRZ at $z/D_{ext} = 1.4$ and $r/D_{ext} = 0.0$. The flame kernel is found to propagate upstream at first, then to expand downstream in the IRZ. The flame front subsequently propagates through the whole combustion chamber and overall ignition is reached after 14.5 ms.

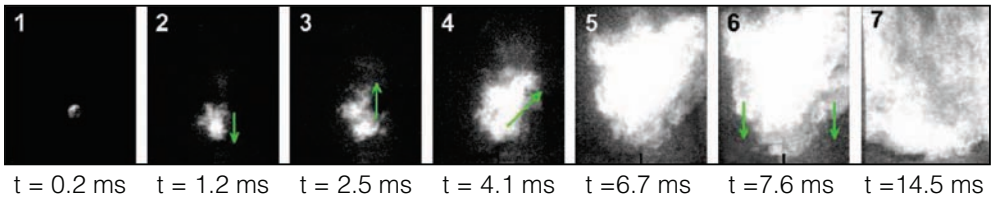

Figure 7.2: Direct visualization of OH* emission during ignition when sparking at $z/D_{ext} = 1.4$ and $r/D_{ext} = 0.0$. Extracted from Cordier (2013).

7.2 Numerical simulations

Due to the high computational cost of LES, reproducing the complete experimental ignition map is today not feasible. Therefore, to achieve the objectives defined for the numerical study, three spark locations have been selected. These points have been selected from the experimental ignition map: they should show different kernel trajectories and exhibit intermediate values $P_{ign,XP}$, indicating important stochastic behavior. The position of these 3 points is illustrated in Fig. 7.1(right) and Tab. 7.1 gives the coordinates, the main flow features and the experimental ignition probability for each location.

	z/D_{ext}	x/D_{ext}	Location	$P_{ign,XP}$
PT1	0.5	0.0	IRZ	[28%-70%]
PT2	0.4	0.4	Shear Layer	50%
PT3	0.8	0.7	SWJ	80%
	F_f	F'_f	k $[m^2.s^{-2}]$	l_t $[mm]$
PT1	0.80	$9.67\ .10^{-3}$	63.7	9.8
PT2	0.46	$13.41\ .10^{-3}$	93.5	32.1
PT3	0.81	$17.62\ .10^{-3}$	67.5	20.5

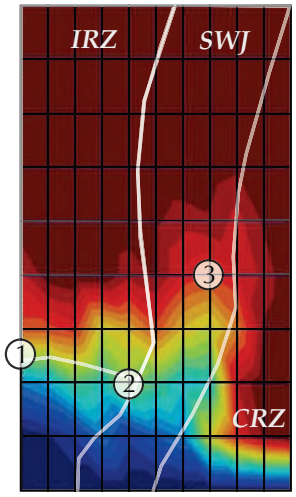

Table 7.1: Position of the ignition locations studied in LES, corresponding flow structure, experimental ignition probability and local non-reacting flow characteristics.

To provide a first idea of the flow characteristics at each location, the flammability factor F_f (see Eq. (5.7)), the flammability dispersion F'_f, the turbulent kinetic energy and an estimation of the integral length are also reported in Tab. 7.1. The flammability dispersion measures the dispersion around stoichiometry of a flammable mixture by:

$$F'_f = \frac{\int_{z_{lean}}^{z_{rich}} |z - z_{st}| P(z)\, dz}{F_f} \tag{7.2}$$

where the stoichiometric, lean and rich mixture fractions of pure methane in air are $z_{st} = 0.055$, $z_{lean} = 0.029$ and $z_{rich} = 0.089$ respectively. F'_f is high when the most probable value for the z disturbution is within the flammable mixture but far from the stoichiometric conditions, and small for a PDF peaked near z_{st}. The turbulent kinetic energy k is directly evaluated from the variance of the resolved velocity field. As for the integral length scale l_t, it is estimated under the assumption of homogeneous isotropic turbulence $l_t = u'^3/\langle\varepsilon\rangle$ with the ensemble averaged scalar dissipation rate (Pope, 2000) given by:

$$\langle\varepsilon\rangle = \frac{1}{N}\sum_{n=1}^{N} 2\nu S_{ij,n} S_{ij,n} \tag{7.3}$$

where $S_{ij,n}$ is the strain rate tensor of the n-th LES snapshot. The turbulent kinetic energy is fairly high at each ignition position but especially at point PT2 located in the shear layer between the SWJ and the IRZ regions. At point PT2, due to the PVC, a large scale coherent structure significantly increases the size of the most energetic eddies as compared to points PT1 or PT3. The flame/turbulence interaction can be characterized in terms of combustion regimes, as introduced in Sec. 3.3.2.a. To estimate the Karlovitz number, the flame properties S_L^0 and δ_L^0 are estimated from the mean mixture fraction conditioned on the flammable range. Placed in the premixed regime diagram, the result indicates that ignition lies in the thin reaction-zone regime where the flamelet hypothesis does not hold because significant quenching of the flame front can occur and the flame preheat layer is modified by small vortices. Note that these results only denote the general trend, and are susceptible to significantly change from one ignition try to the next due to the change in instantaneous equivalence ratio and turbulence fields.

At each location, 20 ignition sequences are computed in LES. Using Eq. (7.1), the uncertainty on the resulting LES probability is about 11.7 %. As shown in Sec. 6.3.6, the vicinity of the injector nozzle undergoes periodic perturbations due to the PVC. The time period of these oscillations is about 1.6 ms, so that ignition is triggered every 0.2 ms in order to span over the whole cycle. Note that, due to the offset observed on the non-reacting flow at the vicinity of the methane jet, PT1 is shifted downstream and is not located on a grid point of the experimental ignition probability map.

7.3 Numerical set-up

7.3.1 Numerical parameters

LES of ignition sequences are performed with AVBP using the numerical parameters listed in Table 7.2, similar to those used for the non-reacting study in Chapter 6.

	Numerical Parameters
Convection scheme	TTGC: $\mathcal{O}(3)$ in space & time (Colin & Rudgyard, 2000)
Diffusion scheme	2Δ operator
SGS model	WALE (Nicoud & Ducros, 1999)
Artif. viscosity	Colin model: $\epsilon^{(2)} = 0.01$, $\epsilon^{(4)} = 0.005$
	Boundary conditions
CH_4 inlet	NSCBC (Poinsot & Lele, 1992) (velocity, 10% turbulence)
Air inlet	NSCBC (Poinsot & Lele, 1992) (velocity)
Atmosphere Outlet	NSCBC (3D) (Granet *et al.*, 2010) (pressure)
Walls	Adiabatic non-slipping walls

Table 7.2: Numerical parameters of AVBP.

7.3.2 Energy deposit model

In the present study, energy deposit is performed using the energy deposit (ED) model developed by Lacaze *et al.* (2009*b*). The ED model follows the methodology proposed by Poinsot *et al.* (1991) where the spark is modeled as a source term in the energy conservation equation. In a TFLES context and in order to avoid undesirable dissipation of the deposited energy, the thickening is not applied before the mass fraction of burnt species exceed 90% of the chemical equilibrium value. The source term follows a Gaussian shape both in time and space given by:

$$\mathcal{Q}_{sp}(r,t) = \frac{\epsilon_i}{4\pi^2\sigma_t\sigma_s^3} e^{-\frac{1}{2}\left(\frac{r}{\sigma_s}\right)^2} e^{-\frac{1}{2}\left(\frac{t-t_0}{\sigma_t}\right)^2} \tag{7.4}$$

where ϵ_i is the amount of energy deposited, r is the Euclidian distance to the center of the deposit x_0, t_0 is the deposit timing and σ_s and σ_t are the characteristic size and duration of the deposit respectively. The parameters of the ED model Δ_s and Δ_t are derived from the Gaussian standard deviation so that 98% of the energy is deposited in $\Delta_s^3\Delta_t$: $\Delta_s = 2\sqrt{ln10^4}\sigma_s$ and $\Delta_t = 2\sqrt{ln10^4}\sigma_t$. Because AVBP is limited to a maximum temperature of 5000 K, the deposit size cannot exactly match a real spark and is increased in the ED model as shown in Fig. 7.3 so that the integral of the power remains the same for the ED model and the real spark, and temperature profile does not exceed 5000 K.

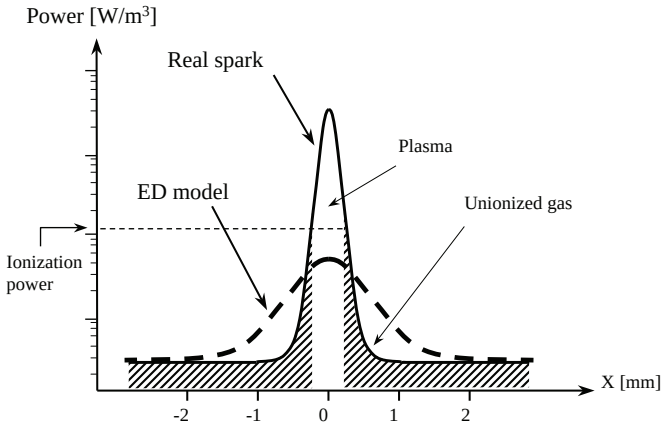

Figure 7.3: Sketch of power distributions for real spark and for the ED model. Extracted from Lacaze *et al.* (2009*b*).

The exact amount of losses induced by the formation of the shock wave and conduction in the electrodes after the spark is not well quantified experimentally. The choice here is to estimate the parameters of the ED model considering that 30% of the deposited energy is transferred to the gas, leading to $\epsilon_i \simeq 29\ mJ$ (Teets & Sell, 1988) measured experimentally. Δ_s is derived from Eq. (7.4):

$$\Delta_s = \frac{4\sqrt{ln10}}{\sqrt{2\pi}} \left(\frac{\epsilon_i}{\rho_f C_p (T_{max} - T_f)} \right)^{1/3} \tag{7.5}$$

where T_{max} is the maximum temperature desired in the kernel and T_f, ρ_f and C_p are the fresh gas properties. The energy deposit time duration is kept constant $\Delta_t = 100\mu s$. Note that Eq. (7.4)

is derived neglecting conduction losses and possibly heat release during the deposit so that the maximum temperature reached in the LES simulation can significantly differ from this prescribed value and vary from one ignition to the next depending on the mixture fraction.

7.3.3 Combustion modeling

The DTFLES model (Colin & Rudgyard, 2000) is employed using the efficiency function from Charlette *et al.* (2002) to handle the flame front on the LES grid. In the context of partially premixed flame, the DTFLES is modified in order to adapt locally the model parameters to the equivalence ratio (Franzelli, 2011). Thus in thickening and efficiency function, S_L^0, δ_L^0 and Ω_0 based on the 2nd reaction of the 2S_CH4_BFER scheme are tabulated versus equivalence ratio from a collection of unstrained laminar premixed flame calculated with CANTERA (Goodwin *et al.*, 2014). The evolution of the DTFLES model parameters as function of the equivalence ratio is reported in Fig. 7.4. The laminar flame speed obtained with the GRI-MECH3.0 detailed scheme is also reported showing a good agreement between the 2S_CH4_BFER scheme used in this study (Sec. 4.4) and a detailed mechanism.

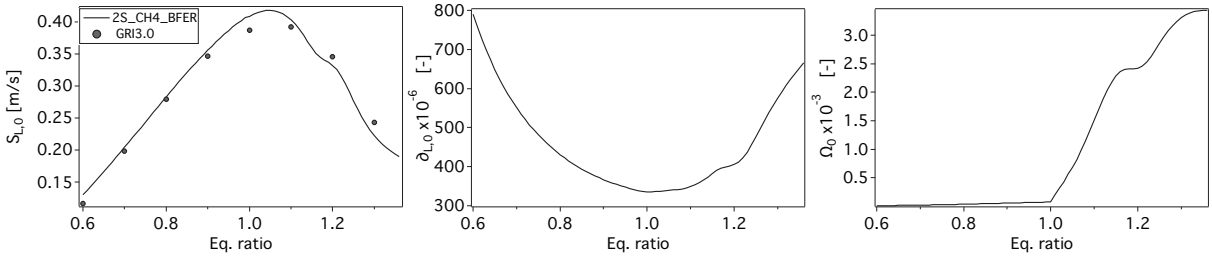

Figure 7.4: Dynamic TFLES model parameters computed versus equivalence ratio from a collection of 1D laminar flames using the 2S_CH4_BFER scheme: S_L^0 (left), δ_L^0 (center) and Ω_0 (right).

The main objective when tabulating the DTFLES parameters versus equivalence ratio is to reduce the thickening factor in regions where the flame burns at lean or rich equivalence ratio since the laminar flame thickness can be more than twice that of the stoichiometric flame depending on the equivalence ratio.

7.3.4 Meshes

All the LES of ignition sequences are performed on fully tetrahedral meshes of about 22 million elements. The global mesh is shown in Fig. 7.5(right) and Fig. 7.5(left) details the mesh in the vicinity of the injector. Note that a large volume is added at the end of the combustion chamber as compared to the non-reacting simulations. The aim of this modification is to avoid the strong dependance of the LES to the outlet boundary conditions during the propagation phase previously observed by Barré (2014). The characteristic mesh size is about 150 μm in the swirler and the mixing regions, 800 μm in the upstream part of the combustion chamber and rapidly increases to about 2 mm downstream.

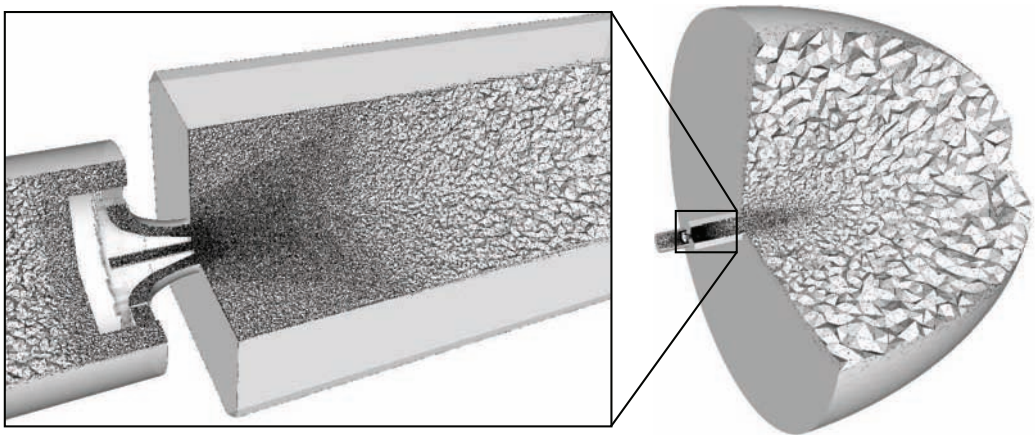

Figure 7.5: LES grid for ignition sequences: full computational domain (right) and details of the injection system region (left).

To comply with the requirements of the ED model (Lacaze *et al.*, 2009*b*) and the recommendations of Barré (2014), three other meshes are generated for each ignition location numerically studied, PT1 PT2 and PT3. Indeed, to fully resolve the initial laminar and small scale kernel without artificially thickening the flame front, a locally refined mesh around the ignition location (in a region of size $20\delta_L^0$ where $\delta_L^0 = 0.51$ mm is the laminar flame thickness at the overall equivalence ratio $\phi_g = 0.75$) is used for the first instants of the simulation, where the cell size is reduced to $\Delta_x = \delta_L^0/6$. Meshes with a refined zone used in this study are presented in Fig. 7.6. Once the flame kernel has sufficiently grown, the refined zone is suppressed and the mesh resolution goes back to LES ($\Delta_x = 1.6\delta_L^0 \sim 0.8$ mm).

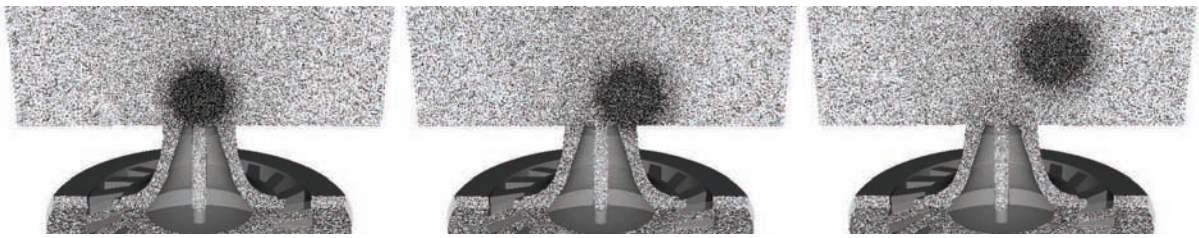

Figure 7.6: LES grids with a refined region at the three energy deposit locations used for the simulation of the first instants after energy deposit.

7.4 Results

60 full LES of ignition sequences have been performed in order to show the capability of LES to reproduce ignition probability at the 3 points of interest and to build a sufficient database to provide a comprehensive understanding of the various mechanisms occurring simultaneously

during the ignition transient. At each location, the 20 ignition trials correspond to 20 realizations of the ignition sequence, only changing the initial flow conditions. Over the 60 ignition sequences computed at the 3 ignition locations, 32 result in a successful ignition of the burner. The ignition probability obtained with LES, noted $P_{ign,LES}$ and reported in Table 7.3, compares well with the experimental $P_{ign,XP}$ listed in Table 7.1 demonstrating the capability of LES to reproduce quantitatively the variability of ignition. The probability of creating a sustainable flame kernel $P_{ker,LES}$ is also estimated based on the temporal evolution of the heat release: cases where the overall heat release drops to zero within the first ms after energy deposit are considered to be failures of kernel generation.

	$P_{ign,XP}$	$P_{ign,LES}$	$P_{ker,LES}$
PT1	80 %	40%	90 %
PT2	46 %	50%	70 %
PT3	81 %	75%	85 %

Table 7.3: $P_{ign,XP}$ along with LES prediction of ignition probability $P_{ign,LES}$ and kernel generation probability $P_{ker,LES}$ at the three ignition locations PT1, PT2 and PT3.

On the basis of the good agreement between $P_{ign,LES}$ and $P_{ign,XP}$, combined with the good LES predictions of the non-reacting flow statistics shown in Chap. 6, the results can be analyzed to identify the mechanisms controlling ignition. As a first step, Sec. 7.4.1 gives an overview of the ignition scenarios captured for each sparking location and highlights the variability resulting of the change in spark timing. Then details of the combustion regime and flame front propagation are proposed, followed by an analysis of the mechanisms leading to ignition failure in Secs. 7.4.2 and 7.4.3. Finally, the ignition sequences are treated as a whole in an effort to relate the ignition outcome to the non-reacting flow properties.

7.4.1 Ignition scenario at the 3 sparking locations

To give an overview of the LES results, ignition sequences are first analyzed using global indicators and qualitatively compared to the experimental observations of Cordier (2013).

7.4.1.a PT1: $z/D_{ext} = 0.5$, $x/D_{ext} = 0.0$

PT1 is located at the bottom of the IRZ, close to the stagnation point. As shown in Sec. 6.3 and in Tab. 7.1 , this position is located in a region of high turbulence intensity and small turbulent structures. The flammability factor indicates locally a strong probability of flammable mixture but $\overline{z}$ is well towards rich mixture and the mean gradient of z is large. As illustrated in Fig. 7.7(left) where the flame is materialized by an iso-surface of temperature $T = 600\ K$, the ignition scenario following sparking at PT1 can be decomposed as follows:

- convection of the kernel towards the methane jet
- development of a highly turbulent partially premixed flame kernel
- expansion of the flame kernel in the IRZ

- flame propagation towards the top of the chamber and expansion in the CRZ

In the successful case, the flame kernel growth is limited during about ~ 5 ms by the high turbulence levels and the vicinity of inflammable mixture at the bottom of the IRZ. In this case, the progressive temperature increase of the IRZ eventually allows the flame kernel to expand and ignite the full burner. In the failed event illustrated in Fig. 7.7(right), a flame kernel is generated but is quickly quenched (< 2 ms) before a sufficient amount of heat is generated. Mechanisms leading to overall flame quenching will be studied in detail in Sec. 7.4.3

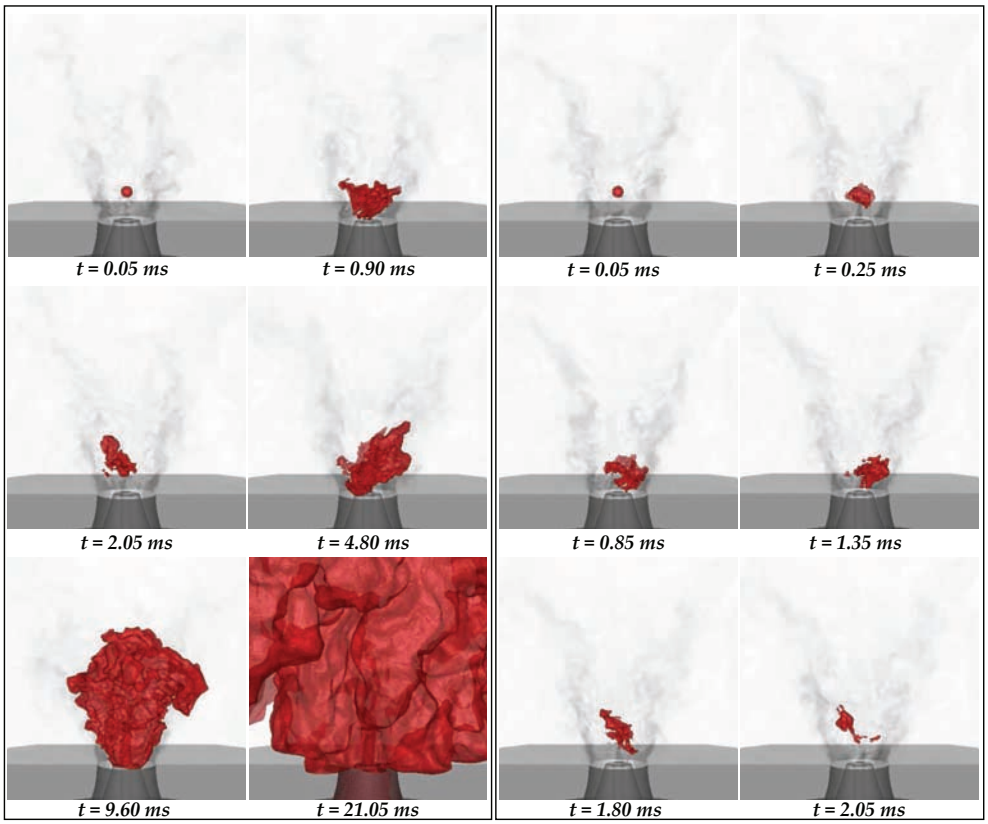

Figure 7.7: Instantaneous flame position tracked by an iso-surface $T = 600$ K in case of ignition success (left) or failure (right) at sparking location PT1.

A qualitative comparison with experiments shows that the LES scenarios for ignition success or failure at PT1 described above match experimental visualization. In accordance with experiments, no case of late failure is observed since once hot gases have filled a sufficient portion of the IRZ, the ignition success is guaranteed. This behavior may be explained by the operating conditions, chosen far from the blow-off conditions by Cordier (2013). The focus is given here on the first instants of ignition and a detailed study of the late flame propagation and stabilization is not performed.

The early flame kernel behavior is investigated in Fig. 7.8 showing flame kernel trajectories projected in a x-z view. Successful ignition events are colored according to the time after ignition ($t - t_{ign}$) while failed events are in white. The flame kernel trajectories are obtained by tracking

the Flame Center of Gravity (FCG). The coordinates of the FCG are defined as the barycentric coordinates of the vertices having a temperature above 1300 K:

$$x_{i,FCG} = \sum_{n=1}^{N} \frac{\rho_n V_n x_{i,n}}{\rho_n V_n} \tag{7.6}$$

where $x_{i,FCG}$ is the i-th coordinate of the FCG, ρ_n and V_n are the density and volume at the n-th node and N is the number of nodes having a temperature $T_n > 1300\ K$. Note that these trajectories only indicate the general trends of the kernel displacement and can significantly differ from the actual kernel motion if large chunks of flame are separated from the bulk. The variability of the velocity field at ignition time scatters the FCG trajectories, but in all cases the FCG first goes downstream the combustion chamber before being deflected out of the burner axis due to the rich methane jet. In cases of successful events, trajectories show that the flame kernel is able to move downstream in an helical motion following the inner shear layer. These trajectories also indicate that, at PT1, there is no evident flame pathway that guarantees ignition success.

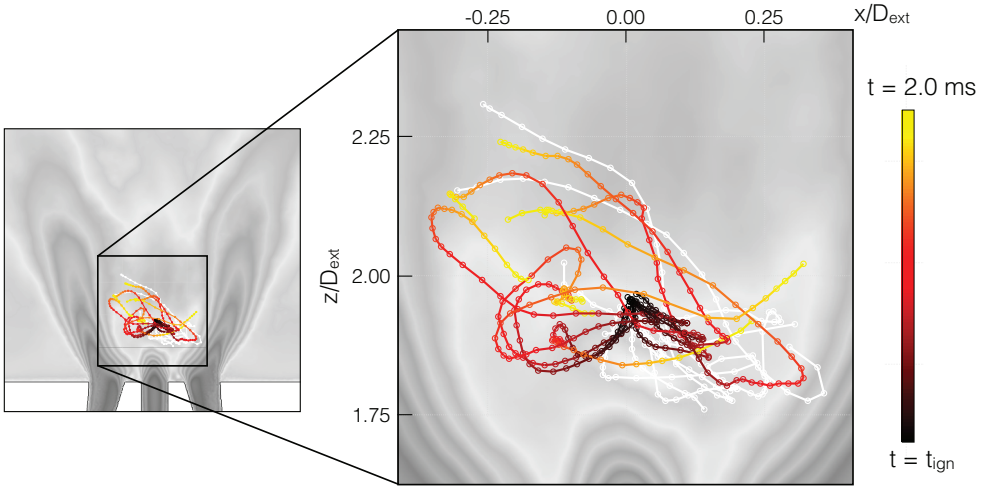

Figure 7.8: Trajectories of the FCG at sparking location PT1 superimposed on the time-averaged velocity field. Successes are colored by the time while failures are in white.

As the flame kernel moves along its trajectory, it grows and interacts with the surroundings. The temporal evolution of the mean heat release rate in the computational domain is plotted in Fig. 7.9 for the first two milliseconds after energy deposit at PT1 and is used as an indicator of the kernel growth. Successful cases are reported in black while plain grey symbols correspond to failed events. The first observation is the wide spreading of the curves and the fact that the distinction between failed and successful events is not obvious even after 1 ms. For all cases, the evolution of heat release is non monotonic, revealing that the flame experiences significant quenching. This shows the high turbulence conditions around the energy deposit, far above the DNS of kernel growth or LES of burners reported in the literature (Poinsot *et al.*, 1991; Subramanian *et al.*, 2010; Reddy & Abraham, 2013). The early peak in heat release denotes the effect of the over-adiabaticity resulting from the energy deposit. This peak is observed for all cases except two, and the peak amplitude is found to vary from one simulation to the other.

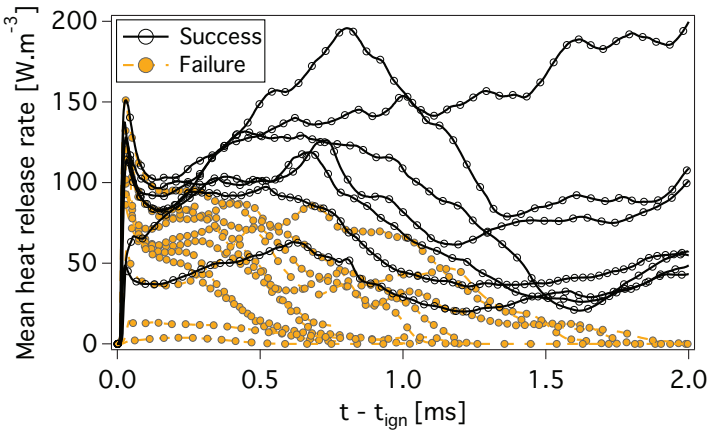

Figure 7.9: Temporal evolution of the mean heat release in the computational domain following energy deposit at sparking location PT1.

7.4.1.b PT2: $z/D_{ext} = 0.4$, $x/D_{ext} = 0.4$

PT2 lies in the shear layer between the IRZ and the SWJ. Due to the presence of the PVC, this region undergoes large fluctuations of mixture fraction between the pure air of the SWJ and the rich mixture at the bottom of the IRZ. The size of the most energetic structures is also significantly larger than at the other two ignition locations (see Tab. 7.1). Apart from the early changes due to the shifted energy deposit location, the ignition scenario is quite similar to the one described for PT1:

- in most cases, the kernel is convected radially inward towards the IRZ and downstream
- a highly turbulent partially premixed flame kernel develops
- the flame kernel in the IRZ expands
- flame propagates towards the top of the chamber and expands in the CRZ

Figure 7.10 shows a successful (left) and failed (right) ignition event at sparking location PT2. The flame kernel is found to expand faster than for PT1 due to the near stoichiometric mixture and the lower level of turbulence experienced in the intermediate part of the IRZ. When convected towards the methane jet, the kernel size is sufficient to overcome the local extinction effects and fills the whole IRZ. The failed ignition event shown in Fig. 7.10 is very short. It corresponds to a failure mode where the amount of flammable mixture at the sparking time and location is insufficient to generate a sustainable flame kernel.

Trajectories of the FCG are reported in Fig. 7.11. The large vortices passing at PT1 induce a large spreading of the trajectories. Since the deposit is performed in the inner shear layer, most kernels go inward. Some misfires are emitted towards the lean SWJ region or maintained in the shear layer. All successful cases penetrate in the IRZ, slightly larger than PT1, at a location of near stoichiometric mixture fraction. However, this path does not guarantee ignition success.

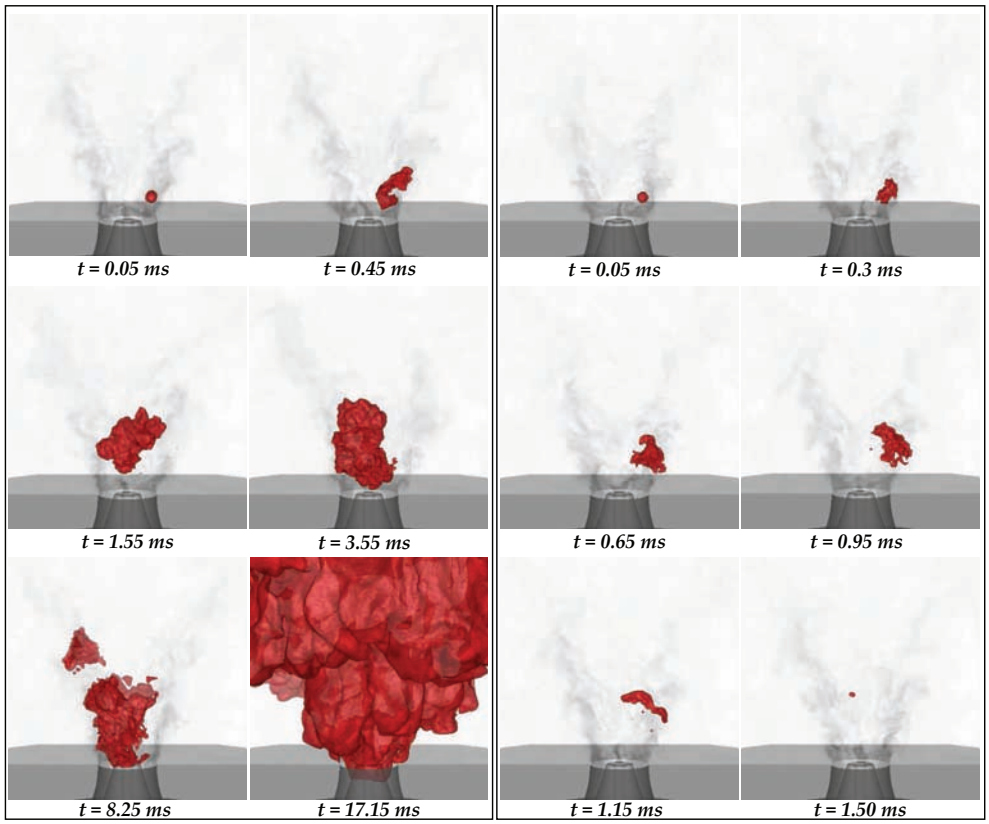

Figure 7.10: Instantaneous flame position tracked by an iso-surface $T = 600\ K$ in case of ignition success (left) or failure (right) at sparking location PT2.

The mean heat release is displayed as function of time in Fig. 7.12. Once again, the change in ignition timing results in a high variability of the kernel growth and the non monotonic evolutions also indicate the occurrence of local extinction. The initial heat release peak is also observed for most cases, but it is interesting to notice that some successful ignition sequences are exempted: energy is delivered to a mixture that is not flammable and the subsequent transport of heat towards flammable regions is responsible for the progressive increase of heat release. As for PT1, it is not possible to unambiguously distinguish success from failure from the early flame development, and global extinctions are observed up to 4 ms after energy deposit.

7.4.1.c PT3: $z/D_{ext} = 0.8$, $x/D_{ext} = 0.7$

PT3 is located in the SWJ region, slightly downstream of the two other ignition points. The flammability factor reported in Tab. 7.1 indicates that at this location, flammable mixture is available most of the time. The turbulence intensity is close to that of PT1, but the size of the turbulent eddies are about twice as large. Two main ignition scenarios are observed:

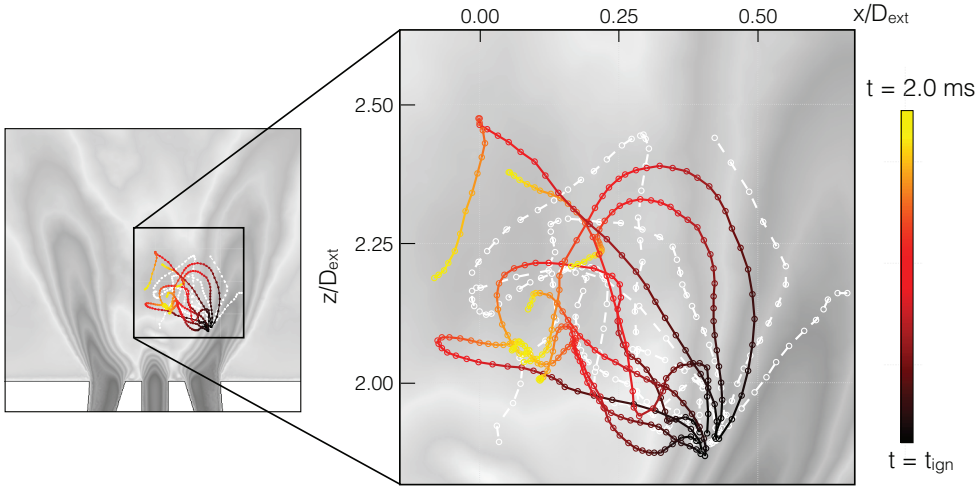

Figure 7.11: Trajectories of the FCG at sparking location PT2 superimposed on the time-averaged velocity field. Successes are colored by the time while failures are in white.

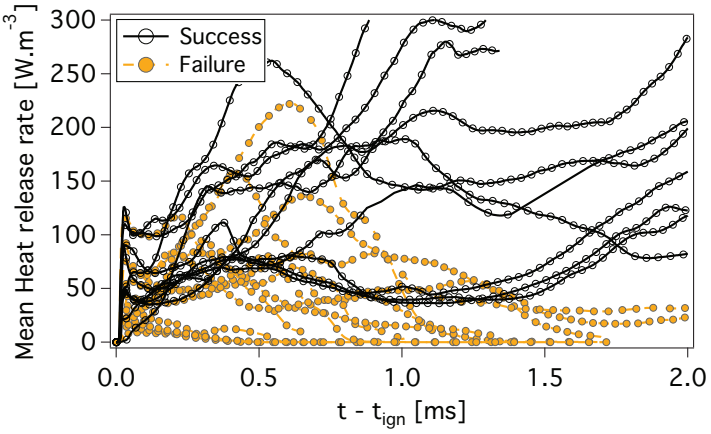

Figure 7.12: Temporal evolution of the mean heat release in the computational domain following energy deposit at sparking location PT2.

Scenario 1:

- the kernel is convected downstream and radially inward
- the flame rapidly develops in the upper part of the IRZ
- the flame propagates towards the injector nozzle
- the flame quickly expands in the whole chamber

Scenario 2:

- The kernel is strongly convected downstream
- the flame develops in the top of the combustion chamber
- the flame front propagates upstream, promoted by both IRZ and CRZ

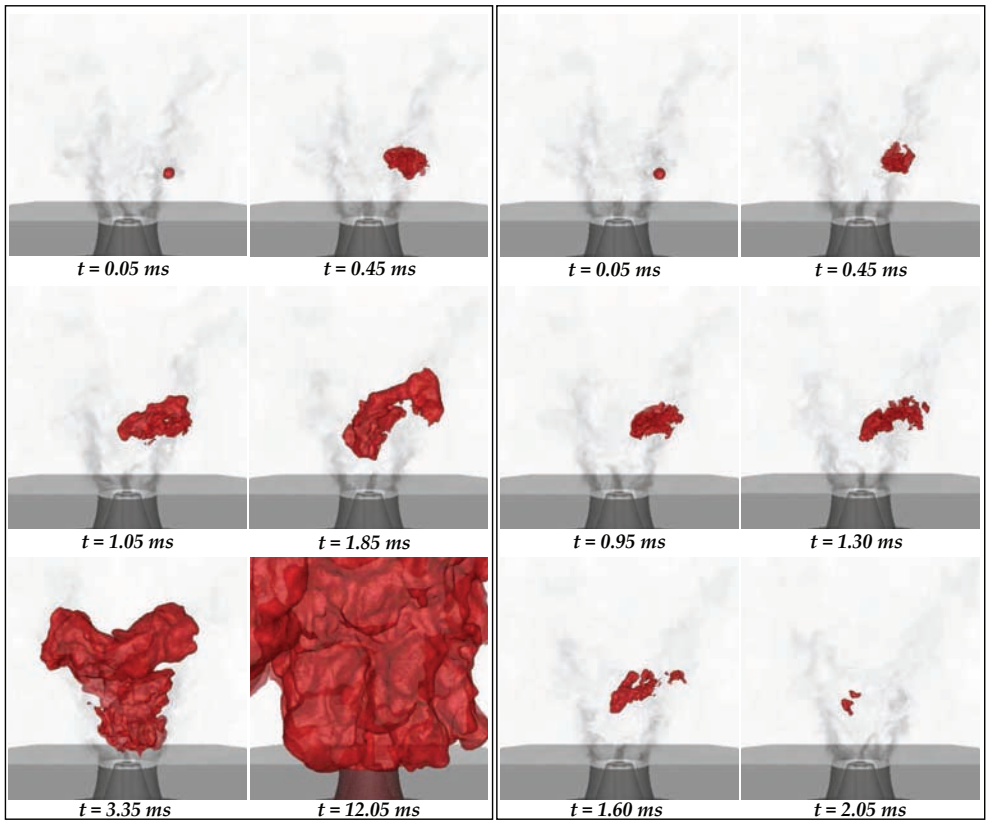

Figure 7.13: Instantaneous flame position tracked by an iso-surface $T = 600\ K$ in case of ignition success (left) or failure (right) at sparking location PT3.

Flame position snapshots in Fig. 7.13 illustrate ignition success (left) and failure (right) at sparking location PT3. The successful case follows Scenario 1 described above. The flame enters the IRZ downstream and is able to expand both towards the injector nozzle and against the slow backward flow in the top of the IRZ. The weak turbulence level and favorable mixture fraction then allows a fast flame expansion with limited local extinction and the overall ignition is reached in less than 15 ms. In the other case, failure is the result of a lean mixture pocket passing at the ignition location at the sparking time. The limited heat release is unable to counter the heat dissipation induced by the turbulence of the SWJ and even though a fragment of the flame is convected in the IRZ, its size is insufficient for its survival.

The FCG trajectories shown in Fig. 7.14 clearly support the existence of 2 scenarios: part of the flame kernel goes towards the IRZ while the other mainly follows a downstream motion. Ignition scenarios reported in Cordier (2013) do not focus on the exact same location, but the second scenario is similar to experiments when sparking in the SWJ. The first scenario seems to guarantee the overall ignition success, at least for all cases performed in LES. On the contrary, the second scenario can lead to ignition failure, in particular if the downstream motion is accompanied of a radially outward displacement. Finally, the overall ignition is reached faster for the first scenario.

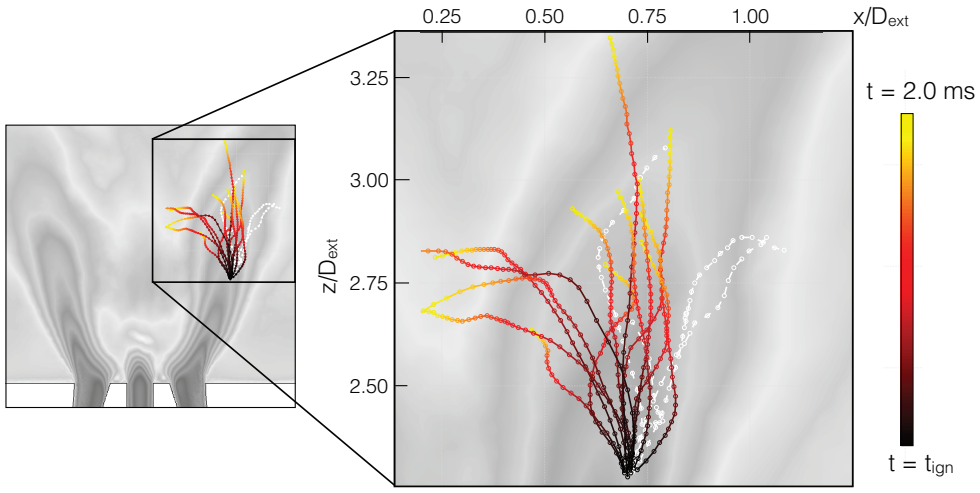

Figure 7.14: Trajectories of the FCG at sparking location PT3 superimposed on the time-averaged velocity field. Success are colored by the time while failures are in white.

The kernel growth is tracked by the mean heat release in Fig. 7.15. Due to the more homogeneous mixture fraction and the lower turbulence intensity at sparking point PT3, the growth rates are much stronger than at the two other locations. For all successful cases, the heat release is found to increase continuously, without any strong reduction of the heat release related to the quenching of large flame portions.

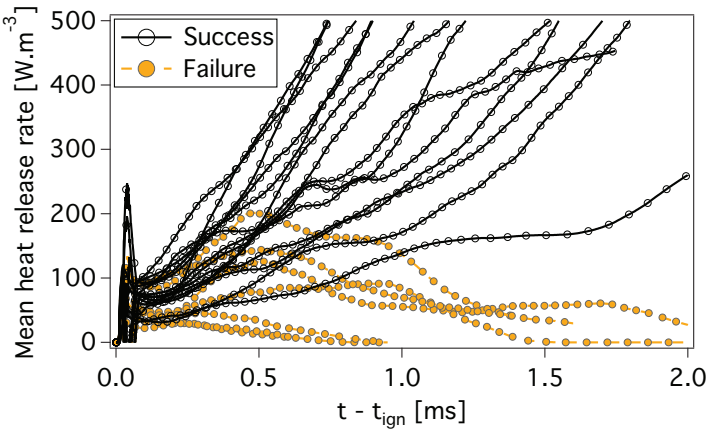

Figure 7.15: Temporal evolution of the mean heat release in the computational domain following energy deposit at sparking location PT3.

7.4.2 Flame structure and propagation

7.4.2.a Combustion regime

A first step towards a better understanding of the parameters driving ignition is to investigate in detail the flame front in terms of combustion regime. The PDF of mixture fraction given in Fig. 7.16 for each ignition location indicates three distinct mixing behaviors:

- at PT1 the most probable mixture fraction is slightly lean but $\overline{z}$ is significantly higher than z_{st} due to the long tail of the PDF towards rich mixture. The long tail denotes the proximity of the methane jet that results in non-zero probability of pure methane pockets at this location.

- at PT2 the PDF is bimodal with nearly equal probability of slightly lean mixture ($z = 0.5$) and pure air. The distribution is characteristic of the intermittent behavior of the mixture in the shear layer between the pure methane jet and the pure air SWJ.

- PT3 shows the most probable mixture at a lean but flammable mixture and is much narrower than the other ignition locations. This is mainly due to the fact that PT3 is located downstream, allowing longer time for mixing.

Two situations must be distinguished depending on the PDF position relative to the stoichiometric mixture fraction: for PT1 and PT2 the PDF of z reported in Fig. 7.16 indicates that the probability of finding lean and rich flammable mixture is fairly equivalent while at PT3 the occurrence of rich mixture is much lower than that of lean one. Thus, it is expected that both non-premixed and premixed combustion regimes might coexist during ignition at PT1 or PT2 but lean stratified premixed combustion should be dominant at PT3.

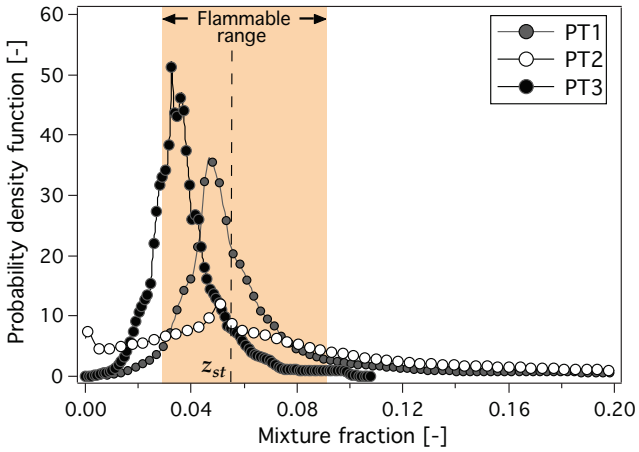

Figure 7.16: PDF of mixture fraction z at the three ignition locations.

To evaluate the respective contribution of both combustion regimes, the Takeno index I_{tk} (Yamashita *et al.*, 1996) is introduced:

$$I_{tk} = \frac{\nabla\vec{Y}_F.\nabla\vec{Y}_O}{|\nabla\vec{Y}_F.\nabla\vec{Y}_O|} \tag{7.7}$$

which evaluates the alignment of the fuel and oxidizer gradients based on a one dimensional geometrical argument. Even though its extension to 3D turbulent flames is not trivial, 3D DNS studies demonstrate the validity of such flame index (Mizobuchi *et al.*, 2002). It is generally argued that diffusion flame are characterized by opposed gradients ($I_{tk} = -1$) and premixed flame by aligned gradient ($I_{tk} = 1$). Note that Fiorina *et al.* (2005) showed that this description breaks down in certain regimes of partially premixed combustion where the gradients of fuel and oxidizer are aligned but combustion remains diffusion-controlled. The integrated heat release conditioned by the Takeno index is evaluated and plotted against time in Fig. 7.17 where a representative example is shown for each ignition location. For ignition at PT1 and PT2, both premixed and non-premixed combustion is encountered but most of the heat release is produced in premixed regions (about 90%). For ignition at PT3, most of the time the combustion is fully premixed even though non-premixed flame front can be found at later time when the flame front reaches the bottom of the IRZ.

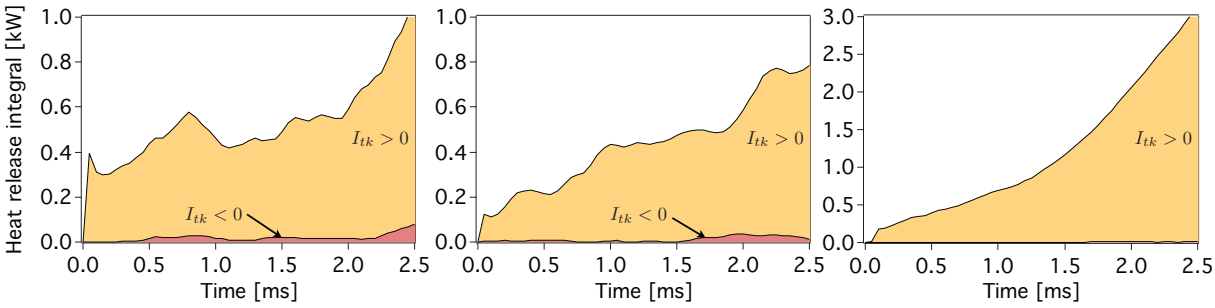

Figure 7.17: Temporal evolution of the conditioned heat release integral for PT1, PT2 and PT3 respectively: orange (or light grey in black and white) denotes premixed combustion ($I_{tk} > 0$) and red non-premixed regime ($I_{tk} < 0$).

An example of the intricate mixing of diffusion and premixed fronts is shown in Fig. 7.18 (for ignition at PT1). The color scale corresponds to the heat release rate while the black line shows the stoichiometric mixture fraction and the grey lines notice the lower and upper static flammability limits. Several flame elements are captured: 1) on the upper LHS, a premixed flame front spanning from lean to rich mixtures is visible with a triple point at the bottom location, 2) on the lower part a diffusion flame front is present along the stoichiometric iso-line. Due to the intense turbulence, diffusion flame fronts are rapidly quenched and re-ignited as vortices propagate downstream in the shear layer between methane and air.

7.4.2.b Flame propagation

The early flame propagation is sustained by the over-adiabaticity resulting from the energy deposit. Due to the very short ignition delay of the 2S_CH4_BFER (Fig. 4.3 in Chap.4) global

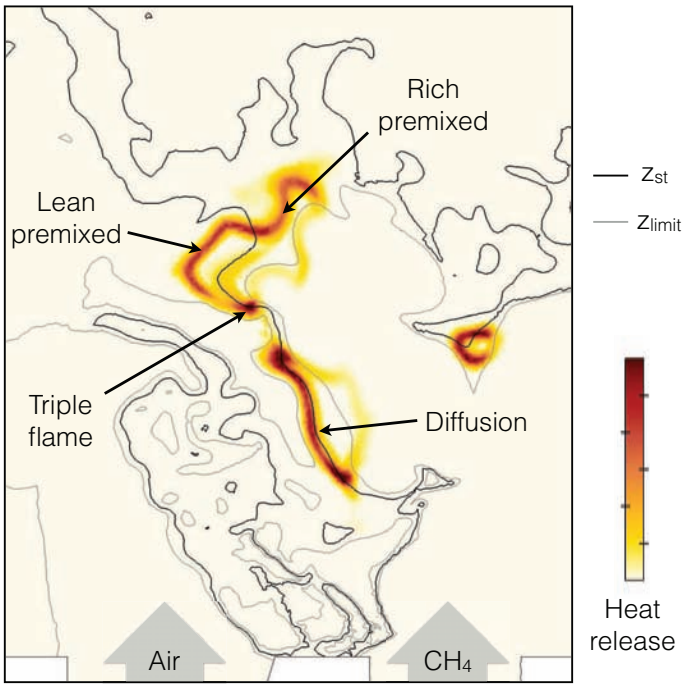

Figure 7.18: Instantaneous field of heat release (color scale) at $t = 0.75\ ms$ at PT1. Black iso-line indicates the stoichiometric mixture fraction iso-line position while grey lines notice the static flammability limits.

kinetic scheme, the maximum temperature and the amplitude of the initial heat release peak is closely related to the amount of fuel readily available at the vicinity of the sparking location. Within the first 700 μs, the temperature of the flame kernel drops to the adiabatic flame temperature and the flame propagation then depends on both the fresh mixture composition and the level of turbulence. Since most of the heat is released in premixed flame mode, the analysis of the flame front is performed on the premixed flame only and unless specified otherwise, the diagnostics are conditioned on positive I_{tk} regions. The overall flame propagation is first studied using the consumption speed:

$$S_c = -\frac{1}{\langle\rho_0\rangle(\langle Y_F^f\rangle - \langle Y_F^b\rangle)A_f}\int_V \dot{\omega}_F\ dv = \frac{1}{\langle\rho_0\rangle(\langle Y_F^f\rangle - \langle Y_F^b\rangle)A_f\mathcal{Q}_{r,CH4}}\int_V \dot{\omega}_T\ dv \tag{7.8}$$

where $\langle\rangle$ indicates averaged over the flame front to take into account the mixture heterogeneity, A_f is the flame surface and $\mathcal{Q}_{r,CH4}$ is the heat of combustion of methane. Defining the flame surface of a turbulent flame front is not an easy task, especially in the thin reaction zone regime since small vortices can significantly increase the thickness of the preheat zone. In this study, A_f is computed from the flame surface density (FSD) Σ and several tests indicate that this evaluation gives results close to those obtained with those of an iso-surface $c = 0.2$.

$$A_f = \int_V \Sigma_{tot}\ dv = \int_V \mathcal{E}\Sigma_{res}\ dv \tag{7.9}$$

where Σ_{tot} and Σ_{res} are the total and resolved FSD respectively. The FSD is based on the gradient of the progress variable c, $\Sigma_{res} = |\boldsymbol{\nabla c}|$ and in this analysis, the progress variable is the reduced

temperature:

$$c = \frac{\widetilde{T} - T_f}{T_{ad} - T_f} \tag{7.10}$$

Note that in partially premixed environment, the definition of the progress variable should be adapted to the local composition by changing the adiabatic temperature T_{ad}. The effect of the definition of c on the description of the flame structure is detailed in Appendix B. The evolutions of S_c for successful and failed ignition events are plotted in Fig. 7.19 for each ignition location.

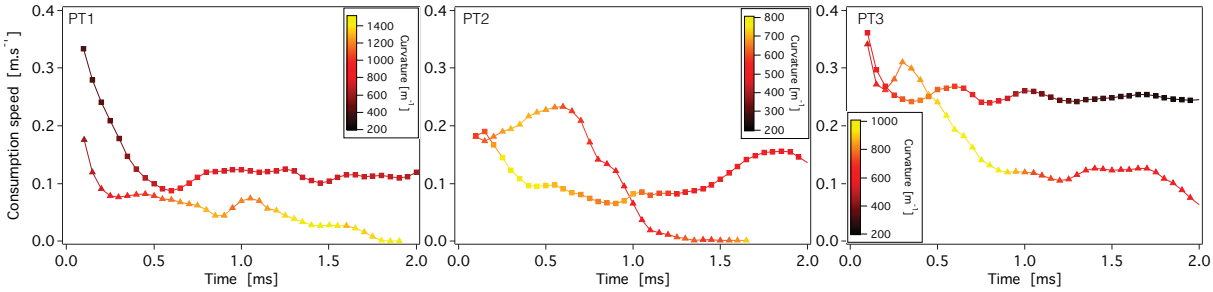

Figure 7.19: Temporal evolution of the consumption speed S_c for successful (square) and failed (triangle) ignition events at each ignition location. Markers are colored by the mean curvature along the flame front.

The consumption speed is found to be initially high due to the high temperature in the kernel. For all successful cases, S_c stabilizes to a value which corresponds to 60% of the unstrained laminar flame speed at the mean equivalence ratio about the flame front so that S_c is higher at PT3 than at PT1 or PT2 due to the near stoichiometric mixture. The mean curvature along the flame front is found to have a significant effect on the consumption speed since high mean curvature is associated with a reduction of the consumption speed.

To further study the flame front motion, the flame velocity is split into a convective contribution induced by the underlying flow and the displacement speed contribution resulting from the thermo-diffusive processes within the flame front. This distinction is related to the definitions of flame speeds introduced in Sec. 3.2.1.b. A formula for the flame density-weighted displacement speed S_d^* is derived in Appendix B:

$$S_d^* = \frac{\overline{\rho}}{\rho_0} S_d = \frac{\overline{\rho}}{\rho_0} \frac{1}{\overline{\rho C_p} |\boldsymbol{\nabla} \widetilde{\boldsymbol{T}}|} \left[\frac{\mathcal{E}}{\mathcal{F}} \dot{\omega}'_T + \boldsymbol{\nabla} \cdot (\mathcal{E} \mathcal{F} \lambda \boldsymbol{\nabla} \widetilde{\boldsymbol{T}}) - \boldsymbol{\nabla} \widetilde{\boldsymbol{T}} \left(\sum_{k=1}^{N} C_{p,k} \overline{J}_{i,k} \right) \right] \tag{7.11}$$

Two tests are performed in Appendix B to ensure that this definition holds within the TFLES context and a detailed study of the components of S_d^* on a 3D ignition case is also reported to clarify its evolution across the turbulent flame front.

In order to evaluate the main contributor to the flame motion, PDFs of displacement speed S_d^* and absolute speed S_a are given for a successful ignition case at PT2 in Fig. 7.20(left). PDFs are computed for $c = 0.25 \pm 0.1$. S_d^* has a near Gaussian distribution bounded between -1 and 2 $m.s^{-1}$ and a mean value around 0.5 $m.s^{-1}$. This value corresponds to the resolved turbulent flame speed: $\mathcal{E}.S_L^0$. The mean absolute flame speed on the other hand ranges from -20 to 20 $m.s^{-1}$,

with a mean value several times higher than the displacement speed. This indicates that the flame motion is mainly driven by the convection induced by the underlying flow and clearly supports the fact that the kernel trajectories reported in Figs. 7.8, 7.11 & 7.14 is linked to variation of the initial flow field rather than the flame displacement speed magnitude and direction.

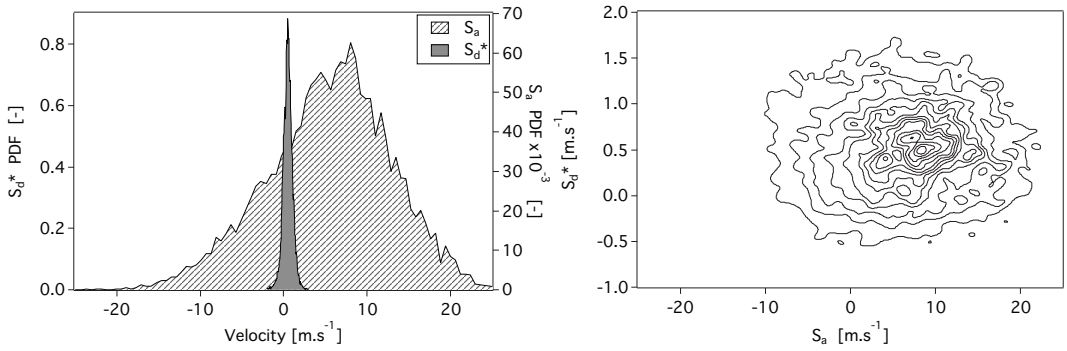

Figure 7.20: PDF of flame density-weighted displacement speed S_d^* and absolute flame speed S_a (left) and joint-PDF of S_d^* and S_a (right) computed for $c = 0.25 \pm 0.1$ at sparking location PT2.

The joint PDF of S_d^* and S_a displayed in Fig. 7.21(right) and shows that there is no correlation between these two quantities: the flame is not able to impose its own expansion dynamics to the surrounding flow due to the high turbulence conditions. The frequent occurrence of negative S_a also indicates that the convection can locally be strong enough to induce a reverse motion to the flame front and participate to the formation of burnt gas pockets.

Thermo-diffusive process however however strongly influence the kernel growth. Unlike S_c (see Eq. (7.8)), S_d^* is a local quantity and its magnitude varies depending on the local mixture fraction and stretch. The decomposition of the flame stretch into two terms, one related to the aerodynamic strain tangential to the flame front and one due to curvature is used hereafter. The effect of curvature is highlighted by the joint PDF of S_d^* and $\mathcal{K}$ reported in Fig. 7.21(left): the displacement speed is inversely proportional to curvature through the tangential diffusion term (see Appendix B). On the contrary, S_d^* is not correlated to the tangential strain rate as shown in Fig. 7.21(right). The fact that the curvature effect dominates the flame response to stretch is coherent with the modeling approach developed by Peters (1999) for flame/turbulence interaction in the thin reaction zone regime. Such results are also obtained in the DNS of Chakraborty & Cant (2004) and Jenkins *et al.* (2006). The kernel growth is then reduced in cases where turbulent structures are able to induce large flame curvature, i.e. for strong turbulence intensity and small length scales.

The dependance of S_d^* to the equivalence ratio follows that of the laminar flame speed: maximum near the stoichiometry and rapidly decreasing for rich and lean mixture. As a consequence, the kernel growth rate is closely correlated to both the amount of flammable mixture around the sparking location but also to its equivalence ratio.

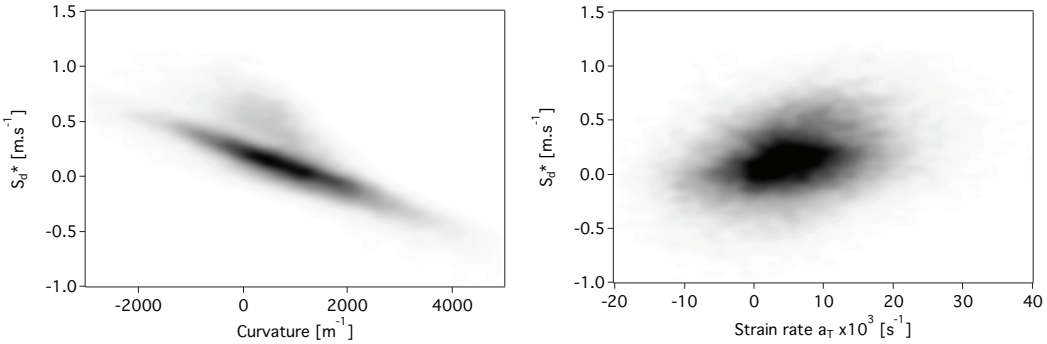

Figure 7.21: Joint-PDF of S_d^* versus $\mathcal{K}$ (left) and a_T (right) computed for $c = 0.25 \pm 0.1$ at sparking location PT2.

7.4.3 Mechanisms leading to ignition failure

In about half of the 60 LES, the deposited energy fails to initiate a stabilized combustion regime. The two failure modes identified can be related to two ignition probabilities as proposed by Birch *et al.* (1981) and used by Ahmed & Mastorakos (2006) and Mastorakos (2009):

- **mode 1**: the deposited energy induces an insufficient amount of heat release due to the lack of flammable mixture around the ignition location or too strong turbulence conditions. Ignition fails to create a flame kernel. The occurrence of this type of failure is quantified by the probability of generating a flame kernel P_{ker}.
- **mode 2**: a flame kernel is created, but the subsequent flame/turbulence interactions in partially premixed turbulent flow leads to its quenching. The overall ignition probability P_{ign} is affected.

An example of **mode 1** is presented in Fig. 7.13 when trying to ignite at PT3 while **mode 2** is illustrated in Fig. 7.10 at PT2. In the case of **mode 1**, the overall dissipation of the flame kernel is reached very rapidly after energy deposit since the turbulent environment strongly enhances heat diffusion. On the contrary, **mode 2** generally occurs at longer times and has been observed during the entire kernel phase duration (up to 3 ms after sparking). The distinction between P_{ker} and P_{ign} is not made in the experiments of Cordier (2013) since this distinction it is not easy to observe from measurements.

7.4.3.a Failure of flame kernel generation

In the present study, failed initiation of the kernel is always due to the lack of flammable mixture at ignition time. Such cases occur at all ignition locations as shown in Figs. 7.9, 7.12 and 7.15 by the rapid disappearance of the chemical source term for some cases. An example of both lean and rich failures at PT3 and PT2 is presented in Fig. 7.22 showing the temporal evolution of the PDF of mixture fraction computed on the vertices where the heat release rate is higher than

10^5 $W.m^{-3}$. The PDF is estimated using a Kernel Density Estimator (KDE) (Silverman, 1986) to avoid the issue related to the number of sample points and change in the PDF range. More details on the KDE method can be found in Appendix A. For the sake of clarity, the distribution at each snapshot used to build such graph is normalized in order to follow the position of the most probable value so that it is not strictly speaking a PDF. The dashed horizontal lines correspond to the lower and upper flammability limits.

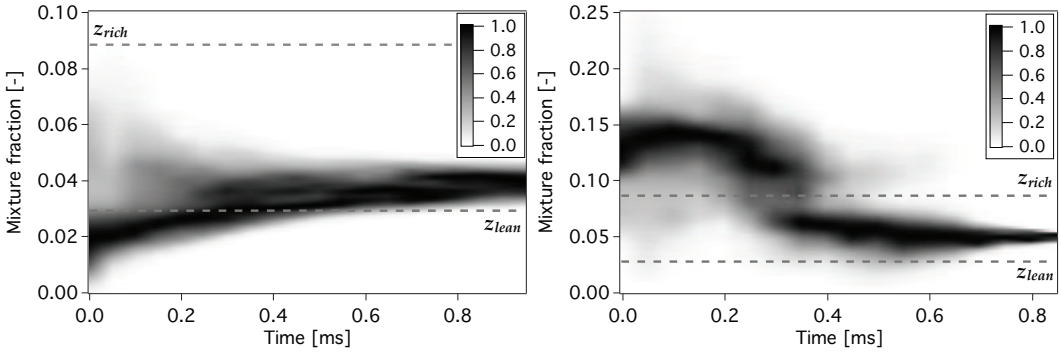

Figure 7.22: Temporal evolution of the z PDF on the reactive flame kernel for a failed ignition event at PT3 (left) and PT2 (right).

Figure 7.22(left) corresponds to an ignition sequence at PT3, where the mixture at the initial deposit location is almost entirely too lean to burn. In Fig. 7.22(right) an ignition at PT2 is reported for which the initial distribution of z is above the rich flammability limit. In both cases, the z distribution stays outside of the flammability limits during the first 200 to 400 μs. Later, since only reactive mixture locations produce heat, the PDF tends towards flammable mixture but the remaining burning gases are unable to compensate for the heat losses that are enhanced by the local turbulent conditions.

7.4.3.b Quenching

Quenching of the flame kernel at longer time can result from the combination of several mechanisms sketched in Fig. 7.23:

- effect of the partial premixing on the flammability of the fresh mixture: quenching due to lack of flammable mixture
- large scale deformation, fragmentation of the flame kernel: thermal quenching of burnt gases pockets
- effect of the strain and curvature on the flame consumption rate: modification of the flame structure

These mechanisms are closely related but not limited to the stretch direct and indirect quenching mechanisms identified in Poinsot *et al.* (1991). If the flame kernel size is of the order of the

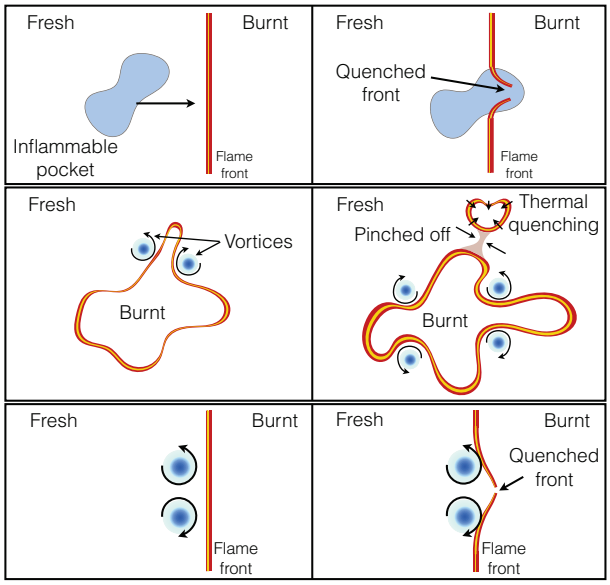

Figure 7.23: Schematic description of flame kernel quenching mechanisms in partially premixed flows: mixture heterogeneity (top row), kernel large scale deformation and fragmentation (middle row) and direct stretch quenching of the flame front (bottom row).

aerodynamic or mixture perturbations, the first two mechanisms can result in overall quenching of the flame kernel. On the contrary, the last mechanism can only induce a significant decrease of the kernel growth rate or local quenching in extreme cases.

- Partial premixing effect

Flame front quenched by inflammable mixture is considered to represent a net loss of energy since fresh gases are heated but do not subsequently produce any significant heat release. From the PDF of mixture fraction reported in Fig. 7.16 and the flammability factor given in Tab. 7.1, the occurrence of partial quenching due to lack of flammable mixture is more frequent at PT2 than PT1 or PT3. However, considering that PT1 is located in a region of strong gradient of z, this quenching mechanism is also critical for PT1. An example of such behavior is illustrated in Fig. 7.24 where the heat release field (color scale) is plotted along with the position of the stoichiometric (black) and lean and rich (gray) flammability mixture fraction iso-contours in a central cut plane through the burner.

Following sparking at PT1, a flame kernel is created in a rich but flammable mixture region. The reverse flow from the IRZ and a burst of pure methane emitted from the jet quench large portions of the flame kernel as the flame front meets the rich flammability limits. The flame kernel completely looses its spherical shape and flame fragments are distributed in the flow. A similar behavior is observed at PT3 during the interaction of the flame kernel with pockets of lean gases in the wake of the SWJ. But at PT3, the kernel is rapidly convected downstream where the mixture distribution is more favorable.

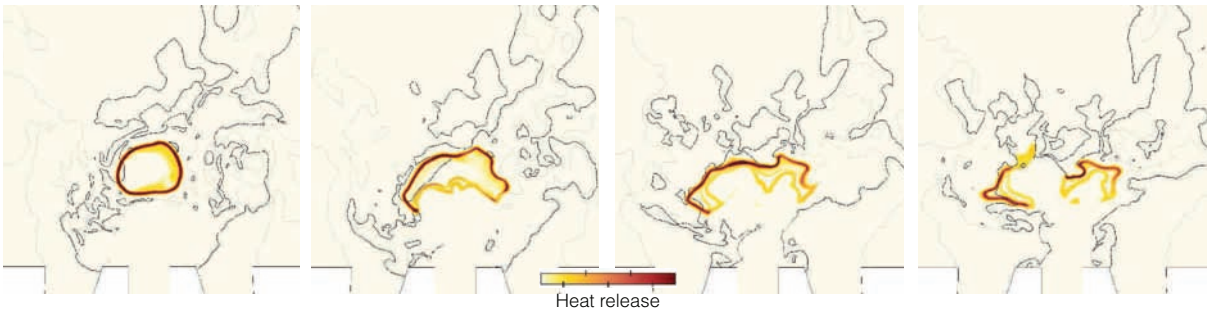

Figure 7.24: Heat release field in a central cut plane through the combustion chamber along with mixture fraction stoichiometric (black) and flammability limits (gray) iso-contours. Interaction of the flame kernel with the methane jet at PT1.

In an attempt to quantify the losses of reactive flame front due to inflammable mixture, the portion of flammable mixture in the preheat zone of the flame is tracked in time. The preheat zone is limited here as the region where $0.4 < c < 0.5$ and the preheated gases flammability indicator $\mathcal{I}_{PFI}$ is simply given by:

$$\mathcal{I}_{PFI} = \int_{z_{lean}}^{z_{rich}} P(z)\, dz \tag{7.12}$$

where $P(z)$ is computed on the grid nodes having $0.4 < c(n) < 0.5$. The temporal evolution of $\mathcal{I}_{PFI}$ is reported for both ignition failure and success at each ignition location in the top row of Fig. 7.25. In order to correlate the evolution of $\mathcal{I}_{PFI}$ with the growth of the kernel, the temporal evolution of the mean heat release is given on the bottom row of Fig. 7.25. At PT1, the kernel is triggered in a flammable mixture but $\mathcal{I}_{PFI}$ rapidly drops due to the convection toward the pure methane jet and this fall occurs sooner in the case of the failed ignition sequence so that the overall heat release is lower from the start. Both ignition sequences at PT2 are initiated in inflammable mixture and the hot gases kernel meet flammable mixture sooner for the failed ignition event resulting in higher overall heat release. After 0.3 ms, more than 80% of the temperature front meets flammable mixture for the successful case against less than 60% for the failed one so that the overall heat release evolution crosses. At PT3, more flammable fuel is initially available in the failed case but the opposite is found soon later and the heat release of the successful case swiftly grows. The flame growth in all these cases is also modulated by the other mechanism described below and $\mathcal{I}_{PFI}$ is only a first step to help distinguishing failed from successful ignition events.

- Flame kernel fragmentation

Under the effect of the large scale turbulence, the flame kernel is wrinkled and deformed. The particular effect of the PVC on the kernel structure will be studied in further detail in Sec. 7.4.3.c. As seen Fig. 7.20, the convection of the flame front is able to counteract the outward expansion of the flame kernel. Locally, flame fronts can be convected toward each others so as to be quenched by mutual annihilation and a burnt gases pocket is created in the process. This mechanism differs from the pocket formation captured in Poinsot *et al.* (1991) and studied in Chen & Im (1998) since it creates pockets of burnt gases in the fresh gases with back-to-back flame annihilation rather than pockets of fresh gases in the burnt gases with face-to-face flame annihilation.

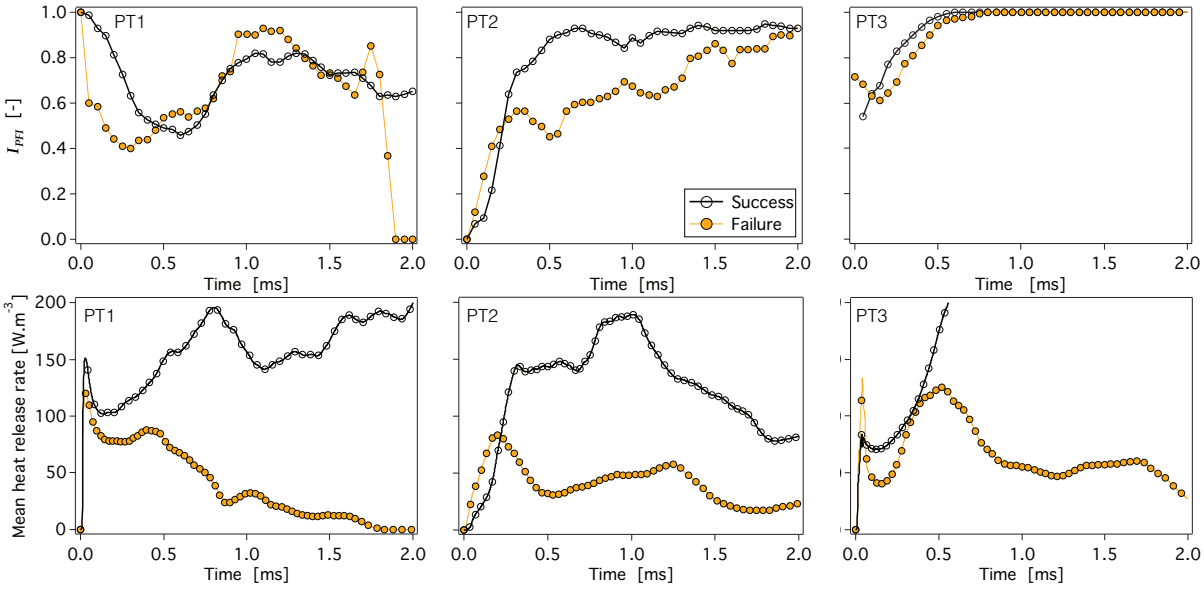

Figure 7.25: Temporal evolution of $\mathcal{I}_{PFI}$ (top row) and overall heat release (bottom row) for a failed and successful ignition event at each ignition location.

Examples of this behavior are illustrated for an ignition at PT3 in Fig. 7.26. The flame kernel is tracked by an iso-surface of temperature at 1700 K colored by the mixture fraction and vortices materialized using an iso-surface of the Q-criterion. Long vortical structures interact with the flame front and generate thin flame branches that are subsequently separated from the kernel bulk. These burnt gases pockets are then quenched since their rate of heat release is unable to counteract the diffusion rate to the surroundings.

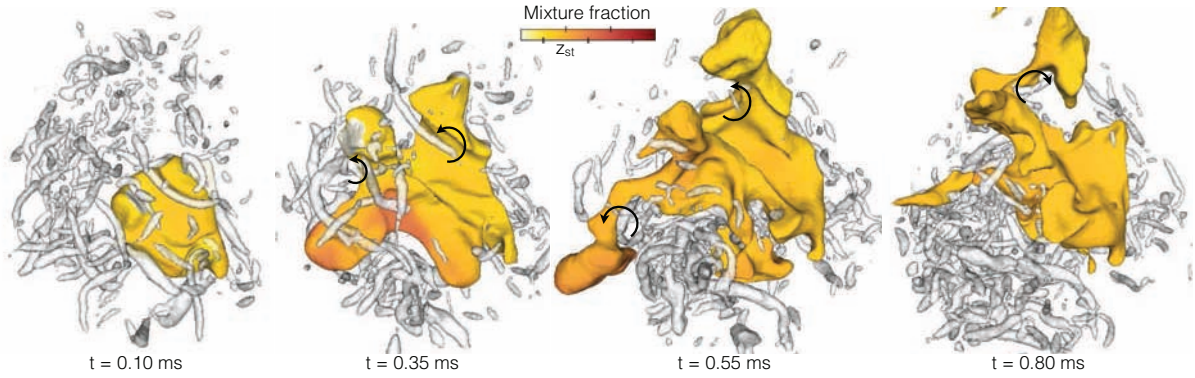

Figure 7.26: Instantaneous snapshots of the flame kernel tracked by an iso-surface of temperature at 1700 K and colored by the mixture fraction. Vortices are captured by an iso-surface of Q-criterion.

To globally quantify this mechanism, the temporal evolution of the shape ratio γ_r defined as the surface of the kernel over its volume is shown for a successful and a failed ignition event at each ignition locations in Fig. 7.27. To focus on the effect of the flame kernel shape only, the

selected cases are nearly free of quenching due to inflammable mixture. At each ignition location, γ_r is found to be higher in the failed ignition than in the successful cases indicating that the flame kernel surface is highly deformed and possibly fragmented.

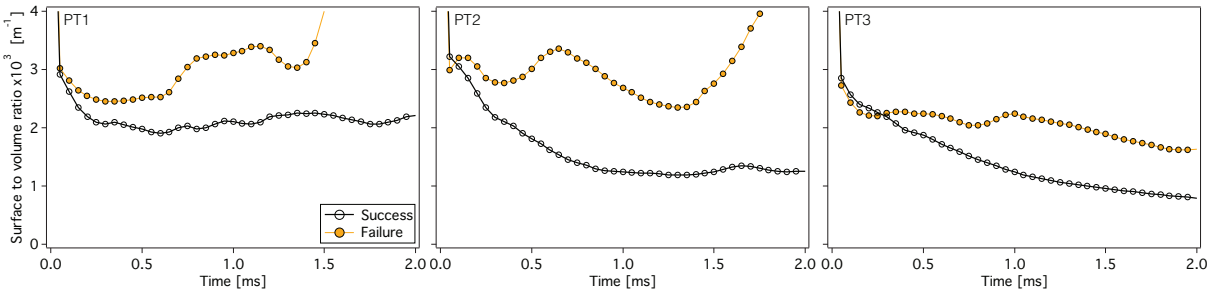

Figure 7.27: Temporal evolution of the shape ratio γ_r for a failed and successful ignition event at each ignition location.

- Flame quenching by stretch effect

As indicated from the turbulent velocity magnitude and length scale reported in Tab. 7.1, the flame/interaction of the present study lies in a region of the premixed turbulent combustion diagram where the flame front structure can be significantly modified by the small vortices of the flow. An illustration of the premixed flame front structure is given in Fig. 7.28 showing the heat release field and several iso-contours of progress variable. The preheat zone thickness (tracked here with $c = 0.2$ and $c = 0.4$ iso-contours) is found to vary from one point of the flame to the other, while the reactive layer thickness (tracked here with $c = 0.6$ and $c = 0.8$ and above) is found to be nearly constant. This confirms that the small vortices are locally able to penetrate the preheat layer inducing its thickening due to an enhanced diffusion process. Poinsot *et al.* (1991) point out that direct quenching of the flame front by stretch only occurs for very large stretch values unless the flame undergoes heat losses.

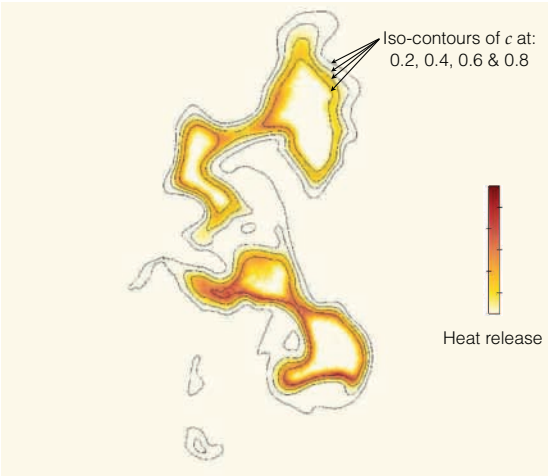

Figure 7.28: Cut through the flame kernel colored by heat release along with several iso-levels of c.

The PDF of S_d^* reported in Fig. 7.20 indicates a non-negligible proportion of negative displacement speed. DNS studies have shown that negative S_d does not pertain to the flame consumption rate but the propagation of a given c iso-level relative to the flow (Gran *et al.*, 1996; Chen & Im, 1998). This differential displacement of c iso-levels indicates a local modification of the flame thickness. To better illustrate that negative S_d corresponds to a thickening of the flame front, the conditional mean value of the flame surface density, which can be interpreted as the inverse of the flame thickness, is computed for both negative and positive regions of S_d and reported in Fig. 7.29(left).

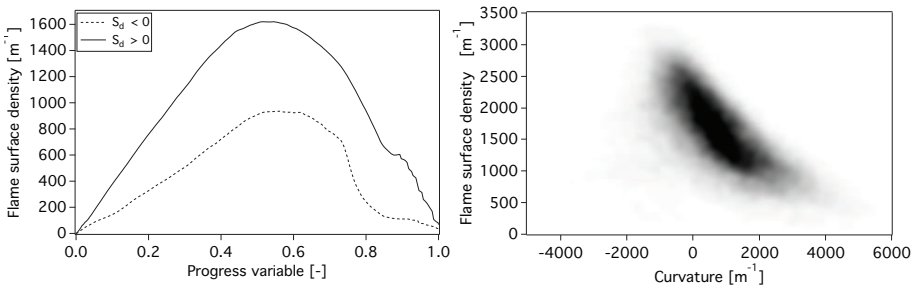

Figure 7.29: Conditional mean of the flame surface density conditioned on S_d positive and negative values regions.

The value of the flame surface density is found to be notably lower for negative S_d, indicating a thicker flame front as compared to the value conditioned on positive S_d. As demonstrated in Fig. 7.21, S_d^* is negatively correlated with curvature so that regions of high positive curvature are thicker and exhibits negative S_d^*. This correlation between curvature and flame thickness is also illustrated in Fig. 7.28 where the c iso-levels are more spaced in positive curvature regions and clearly visible from the joint-PDF of Σ versus $\mathcal{K}$ in Fig. 7.29(right). The thickening of the flame front denotes an imbalance of the reaction-diffusion processes within the flame front and can lead to local quenching of the flame front where heat is diffused away from the reaction zone faster than it is produced. S_d^* can then be used as an indicator of the flame thermal equilibrium with negative values of S_d^* denoting an imbalance and possible extinction of the flame front. The temporal evolution of the mean S_d^* in the $c = 0.25 \pm 0.1$ range for a failed and successful ignition event is plotted in Fig. 7.30 for each ignition location.

For failed ignition events, the flame displacement speed is found to drop below zero at least for a short period of time. Similarly to the consumption speed showed in Fig. 7.19, the local equivalence ratio induces lower S_d^* at PT1 and PT2 and more occurrence of negative values. The dependence of S_d^* is illustrated by the colorscale and confirm its negative correlation with curvature.

7.4.3.c Interactions of the flame kernel with the PVC

The present experimental set-up is the first dedicated to ignition where the swirl is sufficiently strong to observe a PVC. Due to the complexity of the configuration and the required diagnostics, the interaction of the PVC with the flame kernel during ignition was not investigated in the

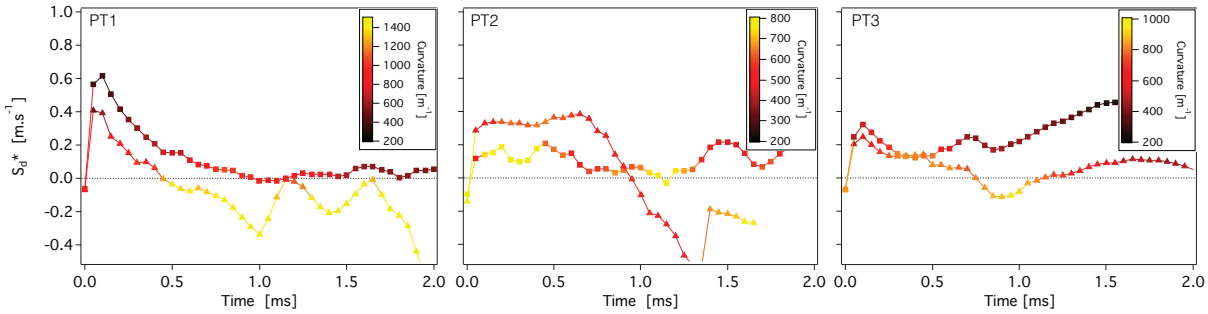

Figure 7.30: Temporal evolution of the mean S_d^* in the $c = 0.25 \pm 0.1$ range for a failed (triangle) and successful (square) ignition event at each ignition location. Markers are colored by the mean flame curvature in the same c range.

experiments. The LES observation reported in Sec. 6.3.6, indicates that the PVC is responsible for periodic fluctuations of the velocity, pressure and mixture field. This structure is particularly strong at the vicinity of the injector nozzle but rapidly degenerates downstream. To evaluate more precisely its interaction with the growing flame kernel, its dynamics is now further investigated.

PT2 is precisely located in the wake of the PVC and PT1 is nested between its two helical branches as depicted in Fig. 7.31.

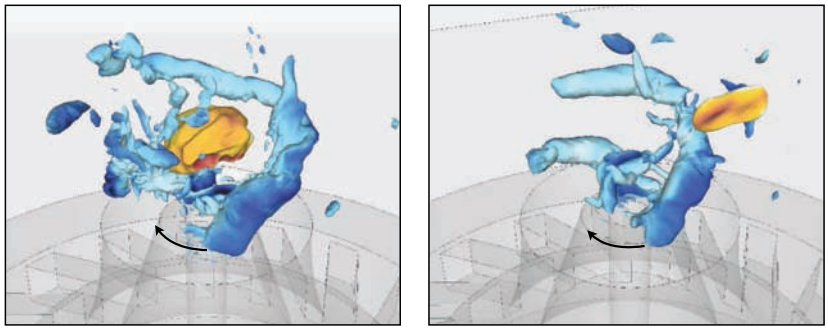

Figure 7.31: Instantaneous snapshot of the relative PVC/kernel positions at ignition time for PT1 (left) and PT2 (right). PVC is tracked by an iso-surface of pressure at $P = 101050\ Pa$ and the kernel by a $T = 1700\ K$ iso-surface.

As shown in Fig. 7.8 for PT1, the IRZ flow pushes the kernel toward the injector nozzle, where large portions of the flame front are quenched by the too rich mixture. The kernel is deflected from the injector axis but is also maintained outside of the PVC core due to its strong rotation so that it is convected between its helical branches. The kernel follows the winding pattern of the PVC as indicated in the top row of Fig. 7.32 and rotates along with the PVC, following the swirl direction. Later, the PVC is sufficiently strong to induce large scale deformation of the kernel and separate flame chunk from the bulk that are then quenched by the turbulence (see Fig. 7.32 bottom row). As the flame kernel gradually heats up the bottom of the IRZ, the PVC becomes

weaker and completely disappears during the second phase of ignition.

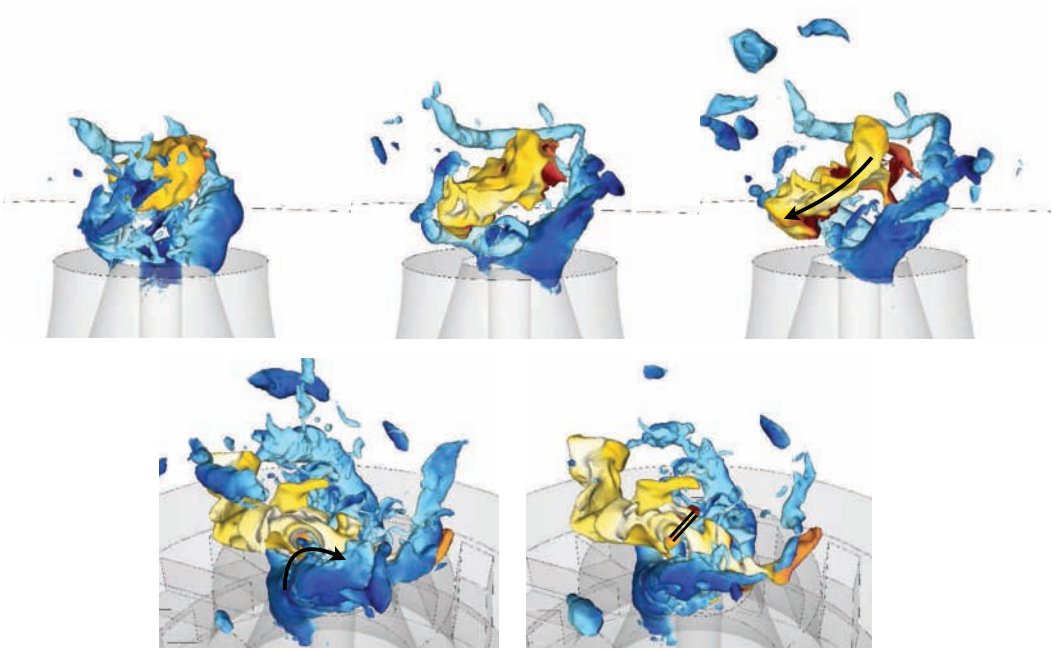

Figure 7.32: Instantaneous snapshots of the PVC/kernel interaction. Top row: winding of the kernel between the PVC branches. Bottom row: large scale deformation of the kernel. The PVC is tracked by an iso-surface of pressure at $P = 101050\ Pa$ and the kernel by a $T = 1700\ K$ iso-surface.

At PT2, the interaction between the flame kernel and the PVC depends on the delay between the energy deposit and the passage of the PVC at the spark location. From the 20 ignition sequences computed, general trends are identified but the number of samples conditioned on the PVC phase is too small to draw a clearer correlation between the PVC passages and the ignition probability. If the PVC passes at the spark position later than 0.6 ms after energy deposit, the kernel as sufficiently grown and undergoes large scale deformation without overall quenching (see top row of Fig. 7.33). When the PVC passes at the spark position within the 0.3 ms following energy deposit, the kernel is rapidly destroyed by the coherent structure and the remaining flame fragments are too small to result in a successful ignition (see bottom row of Fig. 7.33).

7.4.4 Indicators affecting ignition outcome

Having identified the main mechanisms leading to either success or failure of ignition, the aim now is to construct indicators that can be used to distinguish success from failure. Failure of initiating a sustainable flame kernel is expected to be related to the flow properties at the spark location and timing but the quenching at later time has been shown to result from the combination of several mechanisms simultaneously or subsequently during the kernel development. Then, the pointwise or space averaged flow characteristics at the spark timing are first used to recover P_{ker}. Then temporal average indicators are computed to identify the subsequently quenching events.

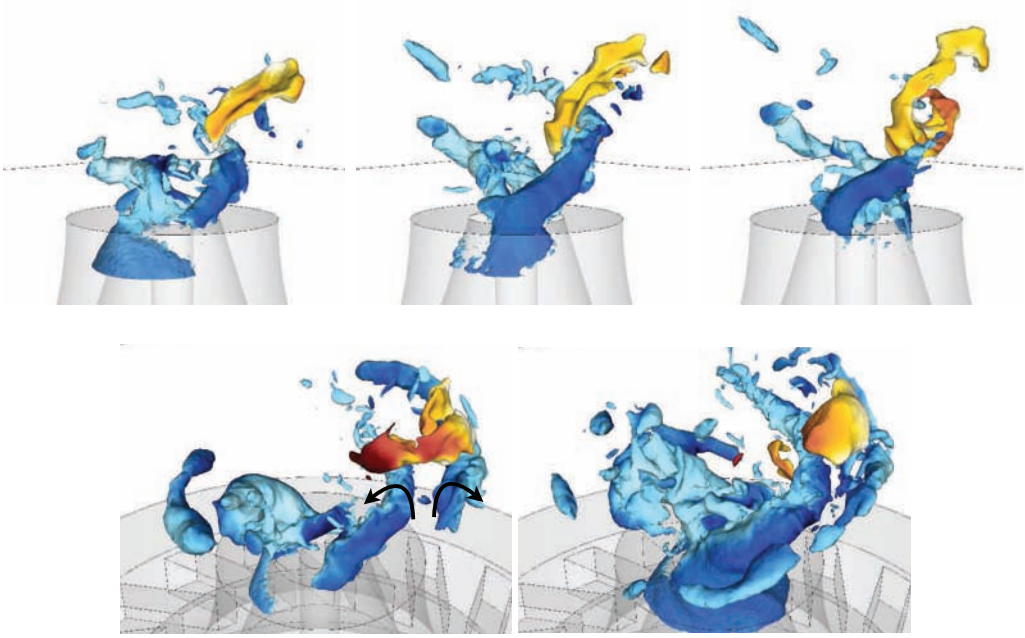

Figure 7.33: Instantaneous snapshots of the PVC/kernel interaction. Top row: winding of the kernel between the PVC branches. Bottom row: large scale deformation of the kernel. The PVC is tracked by an iso-surface of pressure at $P = 101050\ Pa$ and the kernel by a $T = 1700\ K$ iso-surface.

7.4.4.a Initial flow properties at t_0

In a first attempt to discriminate deposits that failed to create a flame kernel, the time history of mixture fraction and velocities have been recorded at the energy deposit locations and are reported in Fig. 7.34. The vertical lines show the timing of a series of ignition LES and differentiate between late failure (red, dashed lines), kernel initiation failure (brown, dotted-dashed) and success (yellow, dotted lines). Subramanian *et al.* (2010) provided similar data for a bluff-body configuration but the magnitude of the velocity fluctuations was much lower than reported here, therefore less detrimental to the kernel survival. At PT1, the axial velocity is found to be globally negative (toward the nozzle) and the mixture fraction above the rich flammability at first, then still rich but flammable later. For PT2, the mixture fraction varies from pure air to rich mixture as also supported by the PDF shown in Fig. 7.16. The axial velocity is alternatively positive and negative with strong fluctuations. At PT3, the mixture fraction stays low with smaller fluctuations as compared to the other locations and the axial velocity is mostly positive with strong fluctuations. For all ignition locations, mixed successful and failed ignition events are found and there is no evident correlation between the pointwise non-reacting flow characteristics and the capability of creating a sustainable flame kernel or ensure its survival, as was also observed by Cordier (2013).

A better indicator can be constructed using spatial distribution around the ignition location rather than pointwise data. The flammability factor F_f is estimated from the cold flow LES at the ignition timing following Cardin (2013). Note that in this case, F_f represents the portion of the

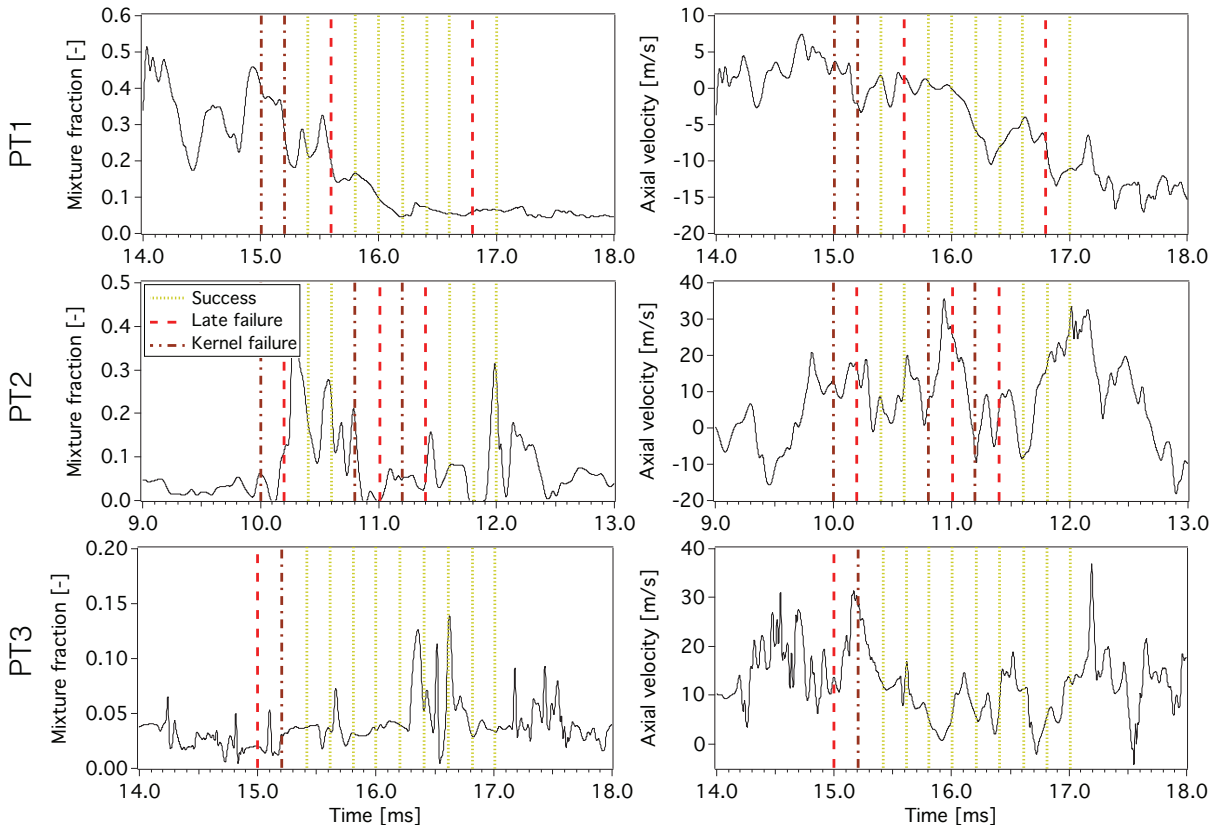

Figure 7.34: Temporal evolution of mixture fraction (left) and axial velocity (right) during non-reacting simulation. Vertical lines correspond to several ignition timing: green dotted line indicates ignition success while red dot-dashed line indicates failure.

spark surroundings that contains flammable mixture. To compute F_f, the PDF of z is constructed in two spherical volumes with different radius around the sparking location at the deposit time. The results are presented in Fig. 7.35for locations PT1, PT2 and PT3 for a spherical volume of radius 1.5 mm (top row) and 2.5 mm (bottom row) respectively. the first volume is about the size of the initial kernel, while the 2.5 mm sphere is larger. The x-axis is the flammability factor while y-axis is the mean mixture fraction in the same spherical domain. Markers are colored depending on the outcome of the ignition event.

At each ignition location, the results show some separation between ignition success and failure. However, the separating line changes from one ignition location to the other and depends on the size of the averaging volume. For PT1, F_f is negatively correlated with the mean mixture fraction and failure of the kernel generation is captured for very low F_f (high $\overline{z}$). As the averaging volume increases, the same trend is observed, but the separation moves toward higher F_f due to the proximity of the rich but flammable IRZ. At PT2, both too lean and too rich mixtures induce low values of F_f but failure is only observed for overall rich mixtures. A clear limit in terms of F_f is not found using the 1.5 mm averaging volume, but it becomes evident for the larger volume. Since PT2 is located in the shear layer, the kernel can rapidly switch from a lean to a rich mixture (or the opposite) and the larger averaging volume allows to better encompass this aspect.

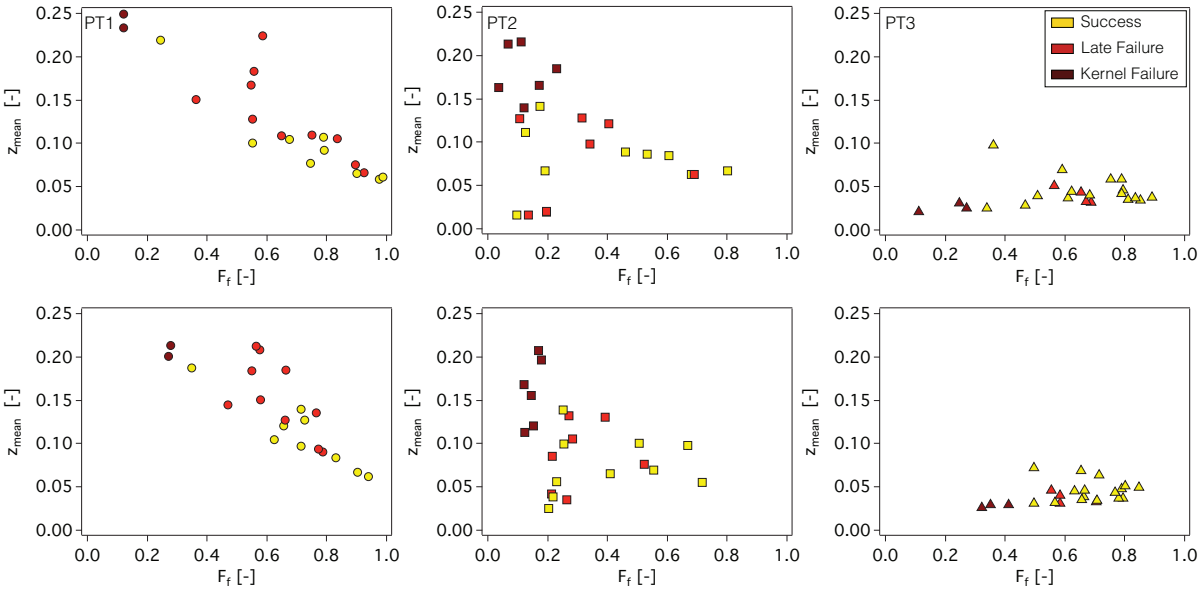

Figure 7.35: Flammability factor $F_f/\overline{z}$ maps colored by the ignition outcome. F_f and $\overline{z}$ are computed in spatial volumes of two sizes (top: 1.5 mm radius, bottom: 2.5 mm radius) around the ignition location at the sparking time.

Finally, values at PT3 do not exhibit a strong separation in terms of $\overline{z}$ but F_f clearly points out a boundary between the failed and successful kernel initiation regions. Although F_f seems to be a good candidate to identify ignition success or failure no threshold value can be determined since it is dependent on the averaging volume size, i.e. the local flow time scale. Finally, Fig. 7.35 also clearly shows that local mixture properties are not able to anticipate the kernel failure at longer time since success and late failure are mixed for all sparking locations.

7.4.4.b Flame/turbulence indicators

To identify indicators that could anticipate kernel quenching, the time history of the flame characteristics are recorded during the flame kernel growth for all simulations where a flame kernel has successfully been initiated. To be consistent with the analysis performed in Sec. 7.4.3, data are restricted and averaged on the $c = 0.25 \pm 0.1$ range located in the preheat zone of the flame. Finally, to provide general trends in a compact way the data are time-averaged over the kernel life time. The time and space averaged values of curvature, S_d^* and tangential strain rate are plotted against mixture fraction for all events that have successfully initiated a flame kernel. Markers are colored by the ignition outcome: yellow denotes success while black indicates failure. The trend described in Sec. 7.4.3.b also appears here with a clear distinction in terms of curvature or S_d^*: the probability of ignition success is strong for low values of curvature and rapidly decreases as the mean curvature exceeds $\simeq 600\ m^{-1}$. Ignition at PT1 (triangles) have $\overline{z}$ above the rich flammability limit and higher values of critical curvature. Consistently with the negative correlation between curvature S_d^*: low values of S_d^* preclude ignition success while the probability of

success increases with higher values of S_d^*. No correlation is found between the tangential strain rate and the ignition success.

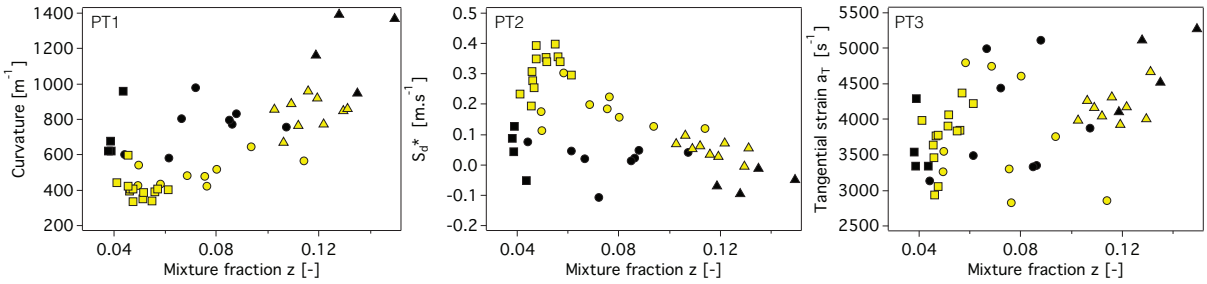

Figure 7.36: κ-$\overline{z}$, S_d^*-$\overline{z}$ and a_T-$\overline{z}$ maps of spatio-temporal mean values for all ignition events colored by the ignition outcome (yellow: success, black: failure). PT1: triangles, PT2: circle and PT3: square.

7.5 Conclusions

Series of LES of ignition sequences in the highly swirled partially premixed KIAI burner have been performed to reveal physical and statistical aspects of the ignition process in complex flow configurations. With respect to previous LES burner studies or DNS kernel expansion simulations, the present configuration makes a step towards gas turbine conditions. Several conclusions can be drawn:

- LES ignition sequences are in good agreement with experiments in terms of flame kernel bulk motion and ignition scenario demonstrating that LES is able to reproduce the driving mechanisms of ignition. At the three ignition locations studied, LES is able to reproduce quantitatively the ignition probability, proving its capability to capture the stochastic nature of the ignition process.
- Flame kernel trajectories are constructed and demonstrate the high variability resulting from the variability of the initial velocity field. There is however no evident correlation between ignition success or failure and the kernel trajectory or its ability to enter recirculation zones (at least at the three locations studied).
- The kernel expansion is found to be highly non-monotonic due to significant flame quenching. Several quenching mechanisms are highlighted: 1) the partial premixing can directly preclude the formation of a flame kernel or quench large chunks of the flame front due to pockets of inflammable mixture; 2) the large scale turbulence induces global deformation of the flame kernel leading to flame-flame interactions and thermal quenching of small burning gases pockets; 3) the flame structure is altered by the turbulence which can significantly lower or even prevent the flame propagation.
- In highly swirled configurations, the presence of a PVC in the region where the flame stabilizes (namely the IRZ) affects the kernel growth if its size is of the order of the PVC structure.

- The probability of creating of sustainable flame kernel is found to be related to the fuel distribution around the spark location at the ignition time rather than to pointwise flow quantities. This is consistent with the previous observation of Cardin (2013) and Cordier (2013).

Lire
la seconde partie
de la thèse